Constraining clouds and convective parameterizations in a climate model from past climate

Riovie D. Ramos[1*], Allegra N. LeGrande[2*], Michael L. Griffiths[1*], Gregory S. Elsaesser[2], Daniel T. Litchmore[2], Jessica E. Tierney[3], Francesco S. R. Pausata[4] and Jesse Nusbaumer[5]

[1]Department of Environmental Science, William Paterson University, Wayne, NJ, USA.
[2]NASA Goddard Institute for Space Studies, New York, NY, USA.
[3]Department of Geosciences, The University of Arizona, Tucson, AZ, USA.
[4]Department of Earth and Atmosphere Sciences, University of Quebec in Montreal, Montreal, Canada.
[5]Climate and Global Dynamics Laboratory, National Center for Atmospheric Research, Boulder, CO, USA.

Corresponding authors: Riovie D. Ramos (ramosr34@wpunj.edu); Allegra N. LeGrande (allegra.n.legrande@nasa.gov); Michael L. Griffiths (griffithsm@wpunj.edu)

Abstract

Cloud and convective parameterizations strongly influence uncertainties in equilibrium climate sensitivity (ECS). We provide a proof-of-concept study to constrain these parameterizations in a perturbed parameter ensemble of atmosphere-only simulations by evaluating model biases in the present-day runs using multiple satellite climatologies and by comparing simulated $\delta^{18}O$ of precipitation ($\delta^{18}O_p$), known to be sensitive to parameterization schemes, with a global database of speleothem $\delta^{18}O$ records covering the Last Glacial Maximum (LGM), mid-Holocene (MH) and pre-industrial (PI) periods. Relative to modern, paleoclimate simulations show greater sensitivity to parameter changes, allowing for an evaluation of uncertainties over a broader range of climate forcing and the identification of parts of the world that are parameter sensitive. Certain simulations reproduced LGM and MH $\delta^{18}O_p$ anomalies relative to the PI better than the default parameterization. Not a single set of parameterizations worked well in all climate states, thus improving simulations requires determining all plausible parameter combinations.

Teaser

Broad paleoclimate variability allows for an evaluation of cloud and convective parameterizations, critical for improving model representations.

Introduction

Cloud and convective processes vary at scales significantly smaller than a general circulation model (GCM) grid box, requiring them to be parameterized on simulated grid-scale variables (*1*). Such parameterizations employ different assumptions (*2*) and thus representation of cloud and convective effects in climate models inherently hold large uncertainties. Cloud and convective parameterizations, aside from aerosol schemes and aerosol-cloud interactions (*3*), are considered the leading source of inter-model spread in equilibrium climate sensitivity (ECS) estimates (*4*–*7*) and consequently, the broad range of future climate projections (*5*, *8*). The latest generation of climate models participating in Coupled Model Intercomparison Project Phase 6 (CMIP6) have an average ECS value of 3.9°C and range from 1.8°C to 5.6°C (*7*), which is higher and more variable than the CMIP5 models (i.e., mean of 3.3°C and range of 1.5°C to 4.5°C (*8*, *9*)) and estimates from Intergovernmental Panel on Climate Change Assessment Report 6 (i.e., mean of 3°C with a very likely range of 2°C to 5 °C, (*10*)). Constraining cloud and convective parameterizations may potentially help narrow ECS uncertainties.

A perturbed parameter ensembles (PPE) experiment, which creates different versions of a climate model by systematically changing a parameter value within a reasonable range, is particularly useful in assessing how much of the uncertainties are explained by parameter choices. Typically, clouds and convective parameterizations are chosen based on the bias score between the climate model and an observational dataset, typically from satellite remote sensing which dates back to 1994 (*11*, *12*). However, in the context of future climate change, these observational datasets only offer a fraction of the range of climate change projected over the next 100 years. Finding ways to constrain these choices on a broader variety of climates in thus desirable.

Widely observed through satellites and preserved on various paleoclimate archives, water isotopes provide a common means to understand present and past climates. Water isotopes serve as integrative tracers of the hydrologic cycle due to molecular differences in mass that drive fractionation during water phase changes. In the atmosphere, the variability in the oxygen isotopic composition of precipitation ($\delta^{18}O_p$) is driven by several local and non-local processes including the origin and initial isotopic composition of the water vapor in an air parcel, amount of rainout, evaporation of rainfall, seasonality and temperature history, and mixing with other air parcels (*12*–*15*). Increasingly incorporating water isotopes in model simulations has significantly advanced our understanding of the mechanisms that govern their variability in broader spatiotemporal scales (*12*).

Previous studies have demonstrated the sensitivity of water isotope ratios to perturbations in cloud and convective parameterizations in isotope enabled GCMs, signifying their utility in evaluating model performance and potentially identifying model biases (*16*–*21*). For example, excessive diffusive advection and high convection frequency were shown to cause significant model biases in the isotope enabled Laboratoire de Météorologie Dynamique Zoomed version 4 (LMDZ4, (*22*)) and Community Atmosphere Model version 5 (CAM5, (*21*)) models, respectively. In the atmosphere-only version of Goddard Institute for Space Studies (GISS) Model E2, water isotopes were found to be more sensitive to parameter changes than traditional diagnostics such as precipitation and temperature, likely related to cumulus entrainment strength (*18*). These models were compared against modern water isotope observations from satellites (e.g., Aura Tropospheric Emission Spectrometer (TES), (*23*)); Scanning Imaging Absorption Spectrometer for Atmospheric Cartography (SCIAMACHY), (*24*)), providing a spatially robust means of constraining model results. In a traditional PPE approach, models are not typically re-tuned into radiative balance after altering a single tuning parameter (*25*), which may have important implications in resolving or revealing biases from previous compensating errors (*26*). However, not much is known whether this tuning approach after each parameter change is preferable especially when considering a broader range of climate states.

Variability in water isotopes may also be obtained from various paleoclimate archives that are not only spatially well-distributed but are also available across timescales drastically different from today, such as the Last Glacial Maximum (LGM; 21 ka, or kilo-years before present) and mid-Holocene (MH; 6 ka) periods. The LGM corresponds to a time when global ice volume was at its maximum and greenhouse gas concentrations were lower than today, both driving major changes in the atmosphere compared to present conditions (*27*–*29*). During the MH, insolation is seasonally amplified in the Northern Hemisphere, with larger winter-to-summer temperature differences and associated changes in the hydrological cycle (*30*, *31*). Performing proxy-model comparison across these contrasting time periods thus allows for evaluating model performance over the full range of hydroclimatic variability in the Earth system.

One excellent source of past hydroclimatic information are speleothems. Speleothems are secondary cave deposits that form from dissolution of carbonate bedrock through water action. While their geographical distribution is largely constrained by the geology of a region, speleothems form under a broad range of hydroclimatic regimes ideal for investigating predominant regional patterns. Variations in speleothem $\delta^{18}O$ largely reflects the $\delta^{18}O$ of soil ($\delta^{18}O_s$) and groundwater percolation, which in turn is heavily influenced by $\delta^{18}O_p$ above the cave and other processes within the karst system (*32*, *33*). Early speleothem $\delta^{18}O$ compilations and the more recently available Speleothem Isotope Synthesis and Analysis (SISAL) database (*34*–*36*), a large global compilation of speleothem isotope records since the last glacial, have aided in evaluating GCM performance across the LGM and MH time periods (*36*–*39*) and have served as an independent validation check in reconstructions of glacial temperature fields (*40*), demonstrating their usefulness in benchmarking isotope enabled paleoclimate simulations. However, not all parts of the world are equally influenced by cloud and convective parameter changes, implying that proxy record locations may be more or less constraining against simulations. This has not been fully quantified in existing paleoproxy-model comparisons and/or analyses of model-satellite discrepancies both globally and restricted to proxy sites only.

In this study, we explore cloud and convective parameterizations (Table 1) in the GISS-E2.1 climate model (*41*) that likely have a significant impact on water isotope distribution and ECS. We use two sets of atmosphere-only simulations: one that has been re-tuned into radiative equilibrium in the pre-Industrial (hereafter referred to as the balanced version) and another which only changes the parameters (hereafter referred to as the unbalanced version, see Materials and Methods), to evaluate whether this approach is preferable in simulations of past climates with large differences in radiative forcing. We investigate the variability and sensitivity of key climate variables to cloud and convective changes and identify parameter-sensitive sites in the present-day (PD, year 2000) and paleoclimate simulations covering the pre-industrial (PI, 0 ka), MH and LGM periods. We also compare and evaluate the model simulations against multiple satellite climatologies and assess the agreement between simulated $\delta^{18}O_p$ and speleothem $\delta^{18}O$ from the SISAL version 2 (SISALv2, (*35*)) database. This proof-of-concept study presents a basis to which we determine the best suite of parameters representing clouds and convective processes across distinct time periods, critical in improving isotope-enabled models and thus, ECS and climate projections.

Results

Spatial sensitivity to perturbations in clouds and convective parameterizations

Based on the resultant spatial variability of precipitation (PREC), surface air temperature (SAT), and $\delta^{18}O_p$ (presented Supplementary Text S1), we derived scores that represent the number of ensembles per grid box showing significant difference from the PPE mean (see Materials and Methods) to highlight spatial sensitivity to parameterization choices. Using the simulations from the balanced version, PREC and $\delta^{18}O_p$ are more sensitive to parameter changes, with nearly 50% of the overall land surface showing significant difference from the mean across all time periods (Fig. 1). SAT, on the other hand, show less sensitivity, covering less than 30% of the total land surface.

The regions that are *most* sensitive to clouds and convective processes in the GISS-E2.1 simulations of SAT are spatially varying across time periods while that of PREC and $\delta^{18}O_p$ are located away from deep convection zones (Fig. 1). Sensitive regions consistently include North America, subtropical South America, Europe, western and northern Africa, north Asia, middle East, and Australia across time periods, forming the key sites to which model results may be principally constrained by the presence of viable paleo-proxy records.

Relative to the PI period, sensitive regions for each variable increase in extent in the MH and LGM periods (Fig. 2), indicating that paleoclimate simulations are more sensitive to parameter changes relative to the modern, supporting the premise of this proof-of-concept study that paleoclimate simulations may be better at discriminating cloud and convective parameterization changes across multiple PPE members than modern. This observation is consistent with that of the unbalanced version, however, the spatial extent of highly parameter-sensitive sites has decreased across all time periods (presented in Supplementary Text S1, figs. S3 and S4), indicating that tuning can impact model sensitivity.

Model evaluation using multiple satellite climatologies

Radiation, cloud, and thermodynamic variables from modern PPE simulations are compared to satellite estimates provided largely from the Obs4MIPS archive (*42*) (see Materials and Methods). It is often the case that inter-product differences for any cloud or thermodynamic variable exceeds published random noise or uncertainty estimates. Such differences arise due to systematic regime-dependent unknowns in satellite cloud and precipitation remote sensing (*43–45*). To avoid root mean square error (RMSE) scores being dependent on any one satellite product choice, we explicitly account for satellite product systematic biases by allowing no contribution to RMSE if the model field falls within the observational range bounded by the minimum and maximum product estimates.

RMSE derived for global, as well as for grid boxes co-located only with proxy sites, are shown in Fig. 3. Across the board, RMSE is lower with a more muted response across PPE members for proxy site locations, where on average, both total and convective rainfall are a factor of ~2 less than most convectively active tropical regions. Less convection implies a smaller reliance on convective and cloud parameterizations, and a less complex atmosphere to simulate. Both *entr60-40* and *tconvadjX2* are most skillful for proxy site PREC, with a 5-10% reduction in RMSE compared to *std*, the default mode for GISS-E2.1; *entr60-40* was the configuration exhibiting subtle improvement across more diagnostics than other PPE members. The top performer changes when considering global scores to *droprad50-50* and *droprad130-50*, with both exhibiting the lowest global RMSE for PREC.

Model evaluation using proxy data under PI, MH and LGM conditions

Our selected proxy database comprises a total of 257, 195 and 81 records for the PI, MH and LGM periods, respectively. From each of the models, we extracted the simulated $\delta^{18}O_p$ nearest each cave site. As shown in our proxy-model comparisons (Fig. 4), the mean $\delta^{18}O_p$ distribution in all runs and time periods are in excellent agreement with the proxies. In these comparisons, we prescribed weights to the simulated $\delta^{18}O_p$, based on Fig. 1, which gives importance to the spatial sensitivity of a particular site to parameter changes. This significantly improved the overall proxy-model agreement compared to the unweighted calculation (fig. S6-a to -s and S7).

While these first order comparisons show excellent agreement, discrepancies remain; for example, simulated $\delta^{18}O_p$ is more negative (positive) at low (mid- to high) latitude speleothem sites compared to the proxies, with those from the LGM exhibiting the largest offsets (Fig. 4). These discrepancies could be due to cave specific factors and model limitations (see Discussion) that may exacerbate proxy-model mismatches. Because simulated $\delta^{18}O_s$ has the potential to better reflect processes within the karst system, we then compared the proxies with the $\delta^{18}O_s$ model results. Comparisons show high and significant correlations across all time periods (fig. S8) with the enriched $\delta^{18}O_s$ values showing a better match. However, the mismatch between the depleted $\delta^{18}O_s$ values remain leading to an overall lower agreement compared from using simulated $\delta^{18}O_p$ (fig. S9).

Spread among the weighted r^2 values in each parameterization is small (standard deviation, $\sigma < 0.05$, Fig. 5), indicating that the parameterization choices do not drastically impact $\delta^{18}O_p$ simulations, consistent with the proxy site-collocated satellite results. Nonetheless, certain simulations represent an improvement from the *std* run. The entrainment rate for plume (*entr20-80*) parameterization exhibits the highest skill for the PI period, whereas the convection adjustment time (*tconvadjX2*) parameterization best represents cloud and convective processes for the MH and LGM periods. Considering only the sites common across the time periods (i.e., limited by the number of LGM sites), the *entr20-80* parameterization became one of the poorest performing models for the PI period. However, another entrainment rate scheme, *entr60-40*, emerged as the best performing parameterization for PI. The *tconvadjX2* parameterization remained the best performing scheme for the MH, indicating that the reduced number of data points did not affect the model evaluation for this time period. These results, broadly consistent with best performers derived from satellite comparisons (considering only the proxy sites), suggest that while different cloud and convective scheme settings do not necessarily impose large changes on the model results for the sites considered, the *best* parameterization for each time period varies depending upon the boundary conditions.

LGM and MH isotopic changes and model performance

To investigate the impact of parameter changes on the relative shift in $\delta^{18}O_p$, we computed anomalies between the LGM and MH relative to the PI. LGM-PI anomalies consist of 17 records whereas MH-PI anomalies contain 79 records. Similar to the absolute value comparisons, we prescribed weights (extracted from Fig. 2) to the simulated $\delta^{18}O_p$ anomalies. The spatial distribution of simulated LGM-PI $\delta^{18}O_p$ in the PPE mean shows an overall depletion over land, with the northern latitudes (i.e., ice sheet over North America and Europe) exhibiting the greatest negative $\delta^{18}O_p$ excursions (Fig. 6A). In contrast, the mid-latitudes are only slightly depleted while the Amazon, northern Africa, Himalayas, and oceanic regions show overall positive $\delta^{18}O_p$ anomalies. Comparison with SISAL $\delta^{18}O$ anomalies show moderate and statistically significant ($p < 0.011$) proxy-model relationship (Fig. 6B, Fig. 7) with at least 70% of the records sharing similar signs. The strong positive and negative anomalies observed in Paraiso cave, Brazil, and Sofular cave, Turkey, respectively, are not captured by the models, where simulated $\delta^{18}O_p$ changes instead show values closer to zero. The spread among the weighted r^2 values remains small ($\sigma < 0.08$, Fig. 7). The *tconvadjX2* parameterization outperformed the *std* run, exhibiting the lowest proxy-model mismatch compared to other parameterization results (Fig. 7). Notably, this simulation also performed best in the absolute value comparisons for the LGM period.

Compared to LGM variations, MH changes relative to PI are more modest. Interior South America, India and Australia show positive $\delta^{18}O_p$ anomalies in the PPE mean (Fig. 6C). In contrast, North America, Eurasia, Himalayas, and East Asia show negative $\delta^{18}O_p$ anomalies, with the western and central African region showing the greatest negative $\delta^{18}O_p$ excursions. Proxy-model agreement across runs lack skill in replicating MH-PI isotopic changes observed in the SISAL records (Fig. 6D, 7), with only 40% of the records showing similar signs in the PPE mean. Isotopic changes over East Asia and the Maritime Continent are quite robust with respect to the proxies. The largest deviations are found in North and Central America (South America) where positive (negative) anomalies are not reflected in the simulated $\delta^{18}O_p$ changes. Overall, the magnitude of change is consistently smaller in the simulations (Fig. 6D). Of the 19 simulations, only 9 PPE members show statistically significant ($p < 0.04$) relationship, outperforming the *std* $\delta^{18}O_p$ run (Fig. 7). The best performing parameterization is *droprad130-50* (weighted r^2 = 0.11, Fig. 7), where 59% of the data points now share similar signs. Notable regions of observed improvement are in Europe and Central Asia (fig. S10). Reducing the number of datapoints to match the sites from the LGM-PI changes shows a different result such that the *critQ2-4* parameterization now shows the highest skill (weighted r^2 = 0.45).

Discussion

In this study, we have identified parts of the world that are most sensitive to convective and cloud parameterizations, which may provide the best opportunity for constraining key metrics in climate models. Parameter-sensitive sites are different between the balanced and unbalanced versions of the models with the latter showing more regions of lower sensitivity scores. This is likely related to the greater variability among PPE members induced by random changes in certain variable fields by the parameter perturbations, affecting more indiscriminate regions in the world. This outcome from the unbalanced version is less useful in constraining biases related to cloud and convective parameterizations.

Our satellite-model analyses, stratified by global and proxy-specific skill scores, reveal that the distribution of proxy sites here lie outside of the spatial domains most impacted by cloud and convective parameterization choices. This suggests a need for additional optimally suited sites distributed across more complex convection-cloud schemes to constrain global simulations. Additionally, conducting these experiments using different coupled atmosphere-ocean-vegetation models could provide an excellent framework for targeted paleoclimate fieldwork to develop archives from these convective- and parameter-sensitive areas across the world.

Though the proxy sites sample less complex atmospheric scenes, the first order spatial pattern of $\delta^{18}O_p$ is in excellent agreement between proxy data and all PPE members across all time periods. Also supported by the satellite analyses, two parameterizations with highest model skill emerged: a 20:80 split of entrainment rate for plume (*entr20-80*) for the PI period and doubled convection adjustment time (*tconvadjX2*) for the MH and LGM periods. The simulations are able to capture broad scale LGM-PI $\delta^{18}O_p$ patterns where *tconvadjX2* parameterization performed best among parameterizations. On the other hand, model skill is significantly reduced in the MH-PI runs where the magnitude of change is consistently smaller in all simulations compared to the proxies.

It is highly likely that the coupled simulations of these same experiments will exhibit a greater range of variability across simulations. The fixed SSTs in our runs allowed us the ability to explore this approach with computationally inexpensive simulations; however, it also throttles coupled feedbacks muting LGM and MH variability across ensemble members and precluded us from calculating ECS for every perturbed parameter. Further, these fixed surface ocean conditions limit the paleoclimate constraints to land-based proxy archives. Other potential sources of model discrepancies are related to ice sheet topography changes and dust concentrations (LGM), along with the lack of vegetation and dust concentration feedbacks (LGM and MH) (*46*–*49*), which may be best evaluated using fully coupled atmosphere-ocean models.

Speleothem proxy climate records have their own set of uncertainties. Speleothem $\delta^{18}O$ primarily reflects local and regional climate signals controlling $\delta^{18}O_p$. However, this signal may be altered as it enters the soil zone and epikarst, a zone that stores infiltrated rainwater, through mixing with existing waters, seasonality of recharge rates, and fractionation by evaporation before reaching the cave system (*50*, *51*). Within the cave itself, the calcite $\delta^{18}O$ signal can be further altered by non-equilibrium fractionation processes and temperature-dependent fractionation during speleothem deposition (*33*, *50*, *51*). Using $\delta^{18}O_s$ instead of $\delta^{18}O_p$ in the comparisons did not show an improvement either (fig. S8, S9). These cave specific factors are not reproduced in the models, exacerbating discrepancies between proxies and simulations. Converting speleothem $\delta^{18}O$ to its drip water equivalent similarly introduces uncertainties as past cave temperatures are unknown (*36*). A natural next step to better comparing the models to proxies is to convert the model output into proxy space via proxy system models, an area of ongoing research (*52*, *53*).

While model biases and proxy uncertainties remain, our initial results add to the growing body of work that demonstrates the utility of paleoclimate data in better constraining model skill, particularly at the model development stage (*29*, *40*, *54*). Our approach and results may be extended to other GCMs and could be especially useful for other models using similar parameters in their cloud and convective parameterization setups. Because cloud feedbacks within the climate system are non-stationary under varying boundary conditions (*54*), hence leading to differences in which parameterization experiment performs best for each time period, fine-tuning future simulations requires determining all plausible parameter combinations and testing the limits of parameter values used in this study. Future work applying this framework to coupled ocean-atmosphere simulations and incorporating vegetation and dust change is needed to fully investigate the impact of parameter choices on paleoclimate simulations. Incorporation of other proxies for water isotopes, like leaf wax δD, may allow for further model evaluation. Techniques like paleoclimate data assimilation could also be leveraged to identify optimal parameter choices.

Materials and Methods

NASA GISS E2.1

Simulations were conducted using the atmosphere-only GISS-E2.1, a CMIP6 submission described in length in Kelley et al., 2020. Relative to GISS-E2 (*55*)), the default E2.1 configuration has an improved treatment of mixed-phase clouds, improvements in the planetary boundary layer parameterization, and systematic increases in convective entrainment rates (*41*), though these rates are perturbed as part of this study as detailed below.

Water tracers ($^{1}H_2{}^{16}O$, “normal” water; $^{2}H^{1}H^{16}O$, δD; and $^{1}H_2{}^{18}O$, $\delta^{18}O$; where permil (‰) $\delta \equiv 1000 * [(R_{std}/R_{smow})-1]$) were included in the land surface, sea ice, sea surface, and atmosphere. These isotopes are tracked through all stages of the water cycle and are advected like water through the model with appropriate fractionation during each phase change (*20*, *56*, *57*).

Time slice experiments

We performed three paleo-time slice experiments as described for the LGM (*28*, *58*)), MH (*59*) and PI (*60*). These followed the Paleoclimate Modelling and Intercomparison Project (PMIP4) and CMIP6 protocols (*58*, *59*). For each time slice, appropriate changes to topography, bathymetry, and land-ocean-ice mask were made (LGM: Glac1D, (*61*–*64*); river routing (*65*–*67*); vegetation cover (*68*); orbital changes (*69*); greenhouse gases (*70*), and standard mean ocean water salinity and water isotopes (*71*) were made (Table 2). All these runs were completed to surface equilibrium in GISS-E2.1-G (*41*); the surface sea ice fraction, sea ice thickness, and sea surface temperatures were then recorded. Coupled simulations are computationally expensive, and thus, surface conditions were used in this proof-of-concept paper to drive a new suite of GISS-E2.1 simulation (CMIP6) in atmosphere-only mode with the same forcing conditions to create the LGM, MH and PI runs. We conduct one further present-day (PD) experiment to facilitate comparison with the satellite products, using year 2000 atmospheric constituents and a climatological mean from Hadley for 2000-2015 for ocean surface conditions (Table 2).

Cloud and convective parameterizations and model tuning

GISS-E2.1 regularly uses five tuning parameters (*41*). It is known that parameter settings have large impacts on the moisture and cloud climatology (*11*), and it is hypothesized that such settings may also have an impact on energy transports and ECS (*25*). Typically, models are not re-tuned into radiative balance after altering a single tuning parameter (*25*). For paleoclimate simulations, the forcing is relatively large, and it is not clear whether this unbalanced method for a PPE is appropriate. Thus, here we re-tuned the model by altering cloud reflectivity (*25*), after each parameter change to ensure that the decadal top of the atmosphere net planetary radiation is within 0.2 W/m^2 during a pre-industrial simulation. We conduct a parallel set of experiments where this tuning was not done to check that the tuning itself is not influencing our interpretation. Ideally, this positions us to complete fully coupled simulations to explore the full range of variability imparted by these clouds and convective changes during the paleoclimate simulations. However, these experiments are computationally expensive, and beyond the scope of this proof-of-concept study (but are planned in the future). The practical consequence is that variability over the ocean especially is throttled, and the climate system during the paleoclimate runs may no longer be in radiative equilibrium (a symptom the incomplete climate response to the strong paleoclimate forcing perturbed parameter runs); we note the net top of the atmosphere radiative balance of each simulation (Table 1).

The basic structure of the clouds and convection schemes are described in (*72*–*74*). We have chosen here to explore six different parameters utilized in the cloud and convection schemes that likely have a substantive impact on ECS as well as water isotope distribution (Table 1). A total of 19 simulations were performed for each time period. Parameters chosen are ones not directly constrained by current in situ or satellite observing platforms.

Rain re-evaporation above the cloud base (*rev*) has been a parameter considered for change previously because it improves convection and variability (e.g., Madden-Julian Oscillation in (*74*)). This parameter makes the GISSE-2.2 model distinct from the GISSE-2.1(*75*). Water isotopes are sensitive to changing this parameter (*18*). Increasing this parameter results in additional atmospheric moistening and a subsequent increase in precipitation over the Maritime Continent (i.e., increased bias); however, it does improve isotopic matches between GISS-E2.1 simulations and satellite observations (*23*).

The entrainment rate (*entr*) parameters control how much environmental mass is entrained into a less- and more-entraining convective plume. At most, two updraft plumes are permitted to initiate at each model level in the GISS convective scheme, and the only requirement is that they have different entrainment rates thus allowing a representation of shallow (i.e., more entraining) and deep (i.e., less entraining) convective towers within any convective cloud ensemble in the GCM grid box.

The convective adjustment time (*tconvadj*) is a parameter that controls how quickly convective mass reaches the tropopause, and thus how quickly the environmental profile of temperature and moisture adjusts to moist convective processes.

The convective trigger (*ctrigger*) parameter determines what environmental conditions are necessary for initiating convection. Physically this parameter can be interpreted as accounting for the multi-faceted role that the planetary boundary layer plays in convective initiation (e.g., turbulent lifting of parcels, variations in near-surface stability or moisture across a grid box), the role of vertical wind shear, the role of mesoscale ascent causing local destabilization, or the role of gravity waves in the weakening of convection-inhibiting stable layers.

The radius multiplier (*droprad*) is a parameter that governs the sizes of liquid droplets and ice particles for a given condensate amount. Though there are some observational estimates of sizes at cloud tops, within-cloud estimates are largely unconstrained (and particularly within convection, where attenuation of radiometric signals are substantial). In general, smaller sizes result in clouds reflecting more shortwave radiation coincident with reduced outgoing longwave radiation.

Auto-conversion of cloud water content to precipitation is governed by a critical cloud water content scaling parameter (*critQ*). Any liquid or ice water content above the scaled critical threshold will be converted to precipitation via auto-conversion, thus affecting cloud condensate, cloud fractions, and in turn, radiation.

Satellite data

Our perturbed parameter configurations are balanced and evaluated using multiple present-day satellite climatologies provided by the Obs4MIPS project (https://esgf-node.llnl.gov/projects/obs4mips/) hosted on the Earth System Grid Federation (https://esgf.llnl.gov). Top of the atmosphere absorbed shortwave (SWabsTOA) and outgoing longwave radiation (OLR), along with cloud radiative forcing estimates (SW_CRE, and LW_CRE) are provided by the CERES EBAF Edition 4.1 product (*76–78*). Temperature and water vapor profiles are provided by AIRS Version 6 retrievals (*79*, *80*) for altitudes at and below 600 hPa, and by MLS Version 4 satellite retrievals (*81*) at and above 200 hPa. Column integrated total (cloud plus precipitating) liquid water estimates (TLWP) are provided by the MAC-LWP (*82*) and TRMM 3A12 (*83*) products, while the column integrated ice counterparts (TIWP) are provided by the CloudSat 2C-Ice (*84*) R05 and MODIS C6 (*85–87*) products. Total precipitation (prec) is provided by GPCP Version 2.3 (*88*) and TRMM TMPA (*89*, *90*) Version 7 products. Convective precipitation (prec_mc) is provided by the GPM Dual-frequency Precipitation (DPR) Radar product (*91*). Global total cloud cover (tcc_isccp) is provided by the ISCCP (*92*) D1 total cloud fraction product, while surface wind estimates are provided by the QuikSCAT satellite and Remote Sensing Systems surface wind products (*93*, *94*).

We compared these multiple satellite climatologies to the perturbed parameter simulations and computed both global and proxy site-averaged root mean square error (RMSE) scores.

Paleoclimate data

To evaluate the atmosphere-only $\delta^{18}O_p$ simulations, we used land-based paleoclimate constraints which are less impacted by the lack of surface ocean and ice feedbacks in these runs, minimizing proxy-model mismatches that may be expected from including ice core records. We use the latest Speleothem Isotope Synthesis and Analysis (SISAL) version 2 database (*35*) and extracted 378 speleothem records from a total of 224 unique sites. In this version, multiple age models for most cave sites were generated but we used the original published chronologies in obtaining mean $\delta^{18}O$ over the following time periods: LGM (21 ± 1 ka), MH (6 ± 1 ka) and PI (last 2 ka). Depending on the mineralogy (i.e., calcite or aragonite), mean $\delta^{18}O$ values (VPDB) were converted to their drip water equivalents analogous to $\delta^{18}O_p$ (VSMOW) (*36*). We used model-generated mean annual SAT extracted at the grid points nearest the cave sites as representative for cave temperatures required in the drip water conversion. Records where mineralogy is unknown or mixed were excluded. Multiple records in a single site and model grid box were then averaged except for those that report large dating errors (e. g., Kesang Cave, (*95*)). A total of 257, 195 and 81 records were obtained for the PI, MH and LGM periods, respectively.

Sensitivity to perturbations and proxy-model comparison

To assess the spatial sensitivity of $\delta^{18}O_p$ to perturbations in cloud and convective parameterizations, we derived z-scores for each experiment, $z = \frac{(x-\mu)}{\sigma}$; where x is the mean $\delta^{18}O_p$ of an ensemble member, μ is the PPE mean and σ is the standard deviation greater than the mean decadal variability of each experiment. We counted the number of ensembles per grid box where the absolute value of z-score is greater than 1 and then normalized the total against the number of PPE runs to derive a sensitivity score. A maximum score of 1 indicates that all 19 ensemble members show significant difference from the PPE mean, and thus the highest sensitivity to parameter changes. We similarly evaluated the spatial sensitivity of PREC and SAT to parameter changes.

Simulated $\delta^{18}O_p$ were extracted from the nearest grid points to the cave sites and compared with that of the proxy for each period, and time slice anomalies with PI as baseline. Skill statistics were calculated over each time period using weighted least square regression. Weights applied to the extracted grid points were the sensitivity scores of a $\delta^{18}O_p$ grid box to changes in cloud and convective parameterizations, highlighting the strength of a proxy site in discriminating among perturbations.

References

1. O. Boucher *et al.*, in *Climate Change 2013: The Physical Science Basis. Contribution of Working Group I to the Fifth Assessment Report of the Intergovernmental Panel on Climate Change*, Eds. (Cambridge University Press, 2013), pp. 571-657.
2. P. Lopez, Cloud and precipitation parameterizations in modeling and variational data assimilation: A review. *Journal of the Atmospheric Sciences* **64(11)**, 3766-3784 (2007).
3. G. A. Meehl *et al.*, Context for interpreting equilibrium climate sensitivity and transient climate response from the CMIP6 Earth system models. *Science Advances* **6(26)**, eaba1981 (2020).
4. J.-L. Dufresne, S. Bony, An assessment of the primary sources of spread of global warming estimates from coupled atmosphere-ocean models. *Journal of Climate* **21**, 5135-5144 (2008).
5. S. C. Sherwood, S. Bony, J.-L. Dufresne, Spread in model climate sensitivity traced to atmospheric convective mixing. *Nature* **505**, 37-42 (2014).
6. M. J. Webb *et al.*, The impact of parametrized convection on cloud feedback. *Philosophical Transactions of the Royal Society A: Mathematical, Physical and Engineering Sciences* **373(2054)**, 20140414 (2015).
7. M. D. Zelinka *et al.*, Causes of higher climate sensitivity in CMIP6 models. *Geophysical Research Letters* **47(1)**, e2019GL085782 (2020).
8. G. Flato *et al.*, in *Climate Change 2013: The Physical Science Basis. Contribution of Working Group I to the Fifth Assessment Report of the Intergovernmental Panel on Climate Change*, T. F. Stocker *et al.*, Eds. (Cambridge University Press, Cambridge, United Kingdom and New York, NY, USA., 2013),
9. R. Knutti, M. A. A. Rugenstein, G. C. Hegerl, Beyond equilibrium climate sensitivity. *Nature Geoscience* **10**, 727-736 (2017).
10. IPCC, in *Climate Change 2021: The Physical Science Basis. Contribution of Working Group I to the Sixth Assessment Report of the Intergovernmental Panel on Climate Change*, V. Masson-Delmotte *et al.*, Eds. (Cambridge University Press, In Press),
11. T. Mauritsen *et al.*, Tuning the climate of a global model. *Journal of Advances in Modeling Earth Systems* **4**, M00A01 (2012).

12. J. Galewsky *et al.*, Stable isotopes in atmospheric water vapor and applications to the hydrologic cycle. *Reviews of Geophysics* **54**, 809-865 (2016).
13. W. Dansgaard, Stable isotopes in precipitation. *Tellus* **16(4)**, 436-468 (1964).
14. J. R. Gat, Oxygen and Hydrogen Isotopes in the Hydrologic Cycle. *Ann Rev Earth Planet Sci* **24**, 225-262 (1996).
15. D. Noone, The influence of midlatitude and tropical overturning circulation on the isotopic composition of atmospheric water vapor and Antarctic precipitation. *Journal of Geophysical Research* **113**, D04102 (2008).
16. M. Bolot, B. Legras, E. J. Moyer, Modeling and interpreting the isotopic composition of water vapor in convective updrafts. *Atmospheric Chemistry and Physics* **13**, 7903-7935 (2013).
17. S. Bony, C. Risi, F. Vimeux, Influence of convective processes on the isotopic composition (d18O and dD) of precipitation and water vapor in the tropics:1. Radiative-convective equilibrium and Tropical Ocean–GlobalAtmosphere–Coupled Ocean-Atmosphere ResponseExperiment (TOGA-COARE) simulations. *Journal of Geophysical Research* **113**, D19305 (2008).
18. R. D. Field *et al.*, Evaluating climate model performance in the tropics with retrievals of water isotopic composition from Aura TES. *Geophysical Research Letters* **41**, 6030-6036 (2014).
19. J.-E. Lee, R. Pierrehumbert, A. Swann, B. R. Lintner, Sensitivity of stable water isotopic values to convective parameterization schemes. *Geophysical Research Letters* **36**, L23801 (2009).
20. G. A. Schmidt, D. L. Hoffman, D. T. Shindell, Y. Hu, Modeling atmospheric stable water isotopes and the potential for constraining cloud processes and stratosphere-troposphere water exchange. *Journal of Geophysical Research* **110**, D21314 (2005).
21. J. Nusbaumer, T. E. Wong, C. Bardeen, D. Noone, Evaluating hydrological processes in the Community Atmosphere Model Version 5 (CAM5) using stable isotope ratios of water. *Journal of Advances in Modelling Earth Systems* **9**, 949-977 (2017).
22. C. Risi *et al.*, Process-evaluation of tropospheric humidity simulated by general circulation models using water vapor isotopic observations: 2. Using isotopic diagnostics to understand the mid and upper tropospheric moist bias in the tropics and subtropics. *Journal of Geophysical Research* **117**, D05304 (2012).
23. H. M. Worden *et al.*, Comparisons of Tropospheric Emission Spectrometer (TES) ozone profiles to ozonesondes: Methods and initial results. *Journal of Geophysical Research: Atmospheres* **112(D3)**, (2007).
24. C. Frankenberg *et al.*, Dynamic processes governing lower-tropospheric HDO/H2O ratios as observed from space and ground. *science* **325(5946)**, 1374-1377 (2009).
25. G. A. Schmidt *et al.*, Practice and philosophy of climate model tuning across six US modeling centers. *Geoscientific Model Development* **10**, 3207-3223 (2017).
26. M. Collins *et al.*, Climate model errors, feedbacks and forcings: a comparison of perturbed physics and multi-model ensembles. *Climate Dynamics* **36**, 1737-1766 (2011).

27. F. S. R. Pausata, C. Li, J. J. Wettstein, M. Kageyama, K. H. Nisancioglu, The key role of topography in altering North Atlantic atmospheric circulation during the last glacial period. *Climate of the Past* **7(4)**, 1089-1101 (2011).
28. M. Kageyama *et al.*, The PMIP4-CMIP6 Last Glacial Maximum experiments: preliminary results and comparison with the PMIP3-CMIP5 simulations. *Climate of the Past* **17**, 1065-1089 (2021).
29. J. E. Tierney *et al.*, Past climates inform our future. *Science* **370(6517)**, (2020).
30. C. M. Brierley *et al.*, Large-scale features and evaluation of the PMIP4-CMIP6 midHolocene simulations. *Climate of the Past Discussions* (2020).
31. B. L. Otto-Bliesner *et al.*, Last Glacial Maximum and Holocene Climate in CCSM3. *Journal of Climate* **19**, 2526-2544 (2006).
32. I. J. Fairchild, A. Baker, in *Speleothem Science: From Process to Past Environments*, R. Bradley, Ed. (Wiley-Blackwell, UK, 2012), pp. 432.
33. M. Lachniet, Climatic and environmental controls on speleothem oxygen-isotope values. *Quaternary Science Reviews* **28**, 412-432 (2009).
34. K. Atsawawaranunt *et al.*, The SISAL database: a global resource to document oxygen and carbon isotope records from speleothems. *Earth System Science Data* **10**, 1687-1713 (2018).
35. L. Comas-Bru *et al.*, SISALv2: A comprehensive speleothem isotope database with multiple age-depth models. *Earth System Science Data* **12**, 2579-2606 (2020).
36. L. Comas-Bru *et al.*, Evaluating model outputs using integrated global speleothem records of climate change since the last glacial. *Climate of the Past* **15**, 1157-1579 (2019).
37. T. Caley, D. M. Roche, C. Waelbroeck, E. Michel, Oxygen stable isotopes during the Last Glacial Maximum climate: perspectives from data-model (iLOVECLIM) comparison. *Climate of the Past* **10**, 1939-1955 (2014).
38. A. Cauquoin, M. Werner, G. Lohmann, Water isotopes-climate relationships for the mid-Holocene and preindustrial period simulated with an isotope-enabled version of MPI-ESM. *Climate of the Past* **15**, 1913-1937 (2019).
39. M. Werner *et al.*, Glacial-interglacial changes in H218O, HDO and deuterium excess - results from the fully coupled ECHAM5/MPI-OM Earth system model. *Geoscientific Model Development* **9**, 647-670 (2016).
40. J. E. Tierney *et al.*, Glacial cooling and climate sensitivity revisited. *Nature* **584**, 569-573 (2020).
41. M. Kelley *et al.*, GISS-E2. 1: Configurations and climatology. *Journal of Advances in Modeling Earth Systems* **12(8)**, e2019MS002025 (2020).
42. D. Waliser *et al.*, Observations for model Intercomparison project (Obs4MIPs): Status for CMIP6. *Geoscientific Model Development* **13**, 2945-2958 (2020).
43. D. I. Duncan, P. Eriksson, An update on global atmospheric ice estimates from satellite observations and reanalyses. *Atmospheric Chemistry and Physics* (2018).
44. G. S. Elsaesser, C. D. Kummerow, The sensitivity of rainfall estimation to error assumptions in a Bayesian passive microwave retrieval algorithm. *Journal of Applied Meteorology and Climatology* **54**, 408-422 (2015).
45. J. Liu, C. D. Kummerow, G. S. Elsaesser, Identifying and analysing uncertainty structures in the TRMM microwave imager precipitation product over tropical ocean basins. *International Journal of Remote Sensing* **38(1)**, 23-42 (2017).

46. M. Crucifix, C. D. Hewitt, Impact of vegetation changes on the dynamics of the atmosphere at the Last Glacial Maximum. *Climate Dynamics* **25(5)**, 447-459 (2005).
47. S. P. Harrison *et al.*, Climate model benchmarking with glacial and mid-Holocene climates. *Climate Dynamics* **43**, 671-688 (2014).
48. V. Masson-Delmotte *et al.*, Past and future polar amplification of climate change: climate model intercomparisons and ice core constraints. *Climate Dynamics* **26**, 513-529 (2006).
49. D. J. Ullman, A. N. LeGrande, A. E. Carlson, F. S. Anslow, J. M. Licciardi, Assessing the impact of Laurentide Ice Sheet topography on glacial climate. *Climate of the Past* **10**, 487-507 (2014).
50. A. Baker *et al.*, Global analysis reveals climatic controls on the oxygen isotope composition of cave drip water. *Nature Communications* **10 (2984)**, 1-7 (2019).
51. A. Hartmann, A. Baker, Modelling karst vadose zone hydrology and its relevance for paleoclimate reconstruction. *Earth Science Reviews* **172**, 178-192 (2017).
52. S. G. Dee *et al.*, Improved spectral comparisons of paleoclimate models and observations via proxy system modeling: Implications for multi-decadal variability. *Earth and Planetary Science Letters* **476**, 34-46 (2017).
53. M. N. Evans, S. E. Tolwinski-Ward, D. M. Thompson, K. J. Anchukaitis, Applications of proxy system modeling in high resolution paleoclimatology. *Quaternary Science Reviews* **76**, 16-28 (2013).
54. J. Zhu, C. J. Poulsen, J. E. Tierney, Simulation of Eocene extreme warmth and high climate sensitivity through cloud feedbacks. *Science Advances* **5**, eaax1874 (2019).
55. G. A. Schmidt *et al.*, Using paleo-climate comparisons to constrain future projections in CMIP5. *Climate of the Past* **10**, 221-250 (2014).
56. A. N. LeGrande, G. A. Schmidt, Sources of Holocene variability of oxygen isotopes in paleoclimate archives. *Climate of the Past* **5**, 441-455 (2009).
57. G. A. Schmidt, A. N. LeGrande, G. Hoffmann, Water isotope expression of intrinsic and forced variability in a coupled ocean-atmosphere model. *Journal of Geophysical Research* **112**, D10103 (2007).
58. M. Kageyama *et al.,* The PMIP4 contribution to CMIP6 – Part 4: Scientific objectives and experimental design of the PMIP4-CMIP6 Last Glacial Maximum experiments and PMIP4 sensitivity experiments. *Geoscientific Model Development* **10(11)**, 4035-4055 (2017).
59. B. L. Otto-Bliesner *et al.*, The PMIP4 contribution to CMIP6 – Part 2: Two interglacials, scientific objective and experimental design for Holocene and Last Interglacial simulations. *Geoscientific Model Development* **10(11)**, 3979-4003 (2017).
60. V. Eyring *et al.*, Overview of the Coupled Model Intercomparison Project Phase 6 (CMIP6) experimental design and organization. *Geoscientific Model Development* **9**, 1937-1958 (2016).
61. A. Abe-Ouchi *et al.*, Insolation-driven 100,000-year glacial cycles and hysteresis of ice-sheet volume. *Nature* **500**, 190-193 (2013).
62. R. D. Briggs, D. Pollard, L. Tarasov, A data-constrained large ensemble analysis of Antarctic evolution since the Eemian. *Quaternary Science Reviews* **103**, 91-115 (2014).

63. L. Tarasov, W. R. Peltier, Greenland glacial history and local geodynamic consequences. *Geophysical Journal International* **150(1)**, 198-229 (2002).
64. L. Tarasov, A. S. Dyke, R. M. Neal, W. R. Peltier, A data-calibrated distribution of deglacial chronologies for the North American ice complex from glaciological modeling. *Earth and Planetary Science Letters* **315-316**, 30-40 (2012).
65. J. M. Licciardi, P. U. Clark, J. W. Jenson, M. DR, Deglaciation of a soft-bedded Laurentide Ice Sheet. *Quaternary Science Reviews* **17 (4-5)**, 427-448 (1998).
66. J. M. Licciardi, J. T. Teller, P. U. Clark, Freshwater routing by the Laurentide Ice Sheet during the last deglaciation. *Geophysical Monograph-American Geophysical Union* **112**, 177-202 (1999).
67. W. R. Peltier, Global glacial isostasy and the surface of the ice-age Earth: the ICE-5G (VM2) model and GRACE. *Annu. Rev. Earth Planet. Sci.* (2004).
68. N. Ray, J. Adams, A GIS-based vegetation map of the world at the Last Glacial Maximum (25,000-15,000 BP). *Internet Archaeology* **11**, 1-44 (2001).
69. A. Berger, M. F. Loutre, Insolation values for the climate of the last 10 million years. *Quaternary Science Reviews* **10(4)**, 297-317 (1991).
70. A. Indermühle *et al.*, Holocene carbon-cycle dynamics based on CO2 trapped in ice at Taylor Dome, Antarctica. *Nature* **398**, 121-126 (1999).
71. R. G. Fairbanks, A 17,000-year glacio-eustatic sea level record: influence of glacial melting rates on the Younger Dryas event and deep-ocean circulation. *Nature* **342**, 637-642 (1989).
72. A. D. Del Genio, Representing the sensitivity of convective cloud systems to tropospheric humidity in general circulation models. *Surveys in Geophysics* **33**, 637-656 (2012).
73. A. D. Del Genio *et al.*, Constraints on Cumulus Parameterization from Simulations of Observed MJO Events. *Journal of Climate* **28(16)**, 6419-6442 (2015).
74. D. Kim, I. S. Kang, A bulk mass flux convection scheme for climate model: Description and moisture sensitivity. *Climate Dynamics* **38**, 411-429 (2012).
75. D. Rind *et al.*, GISS Model E2. 2: A climate model optimized for the middle atmosphere—Model structure, climatology, variability, and climate sensitivity. *Journal of Geophysical Research: Atmospheres* **125(10)**, e2019JD032204 (2020).
76. S. Kato *et al.*, Surface Irradiances of Edition 4.0 Clouds and the Earth's Radiant Energy System (CERES) Energy Balanced and Filled (EBAF) Data Product. *Journal of Climate* **31(11)**, 4501-4527 (2018).
77. N. G. Loeb *et al.*, Clouds and the Earth's Radiant Energy System (CERES) Energy Balanced and Filled (EBAF) Top-of-Atmosphere (TOA) Edition-4.0 Data Product. *Journal of Climate* **31**, 895-918 (2018).
78. N. G. Loeb *et al.*, Toward a Consistent Definition between Satellite and Model Clear-Sky Radiative Fluxes. *Journal of Climate* **33**, 61-75 (2020).
79. B. Tian, E. J. Fetzer, E. M. Manning, TThe Atmospheric Infrared Sounder Obs4MIPs Version 2 Data Set. *Earth and Space Science* **6(2)**, 324-333 (2019).
80. B. Tian, T. Hearty, Estimating and removing the sampling biases of the AIRS Obs4MIPs V2 data. *Earth and Space Science* **7(12)**, e2020EA001438 (2020).
81. J. W. F. Waters, L. Harwood, R.S. Jarnot, R.F. Pickett, H.M. Read, W.G. Siegel, P.H. Cofield, R.E. Filipiak, M.J. Flower, D.A. Holden, J.R. *et al.*, The earth

observing system microwave limb sounder (EOS MLS) on the Aura satellite. *IEEE Transactions on Geoscience and Remote Sensing* **44(5)**, 1075-1092 (2006).

82. G. S. Elsaesser *et al.*, The Multisensor Advanced Climatology of Liquid Water Path (MAC-LWP). *Journal of Climate* **30**, 10193-10210 (2017).
83. C. Kummerow *et al.*, The Evolution of the Goddard Profiling Algorithm (GPROF) for Rainfall Estimation from Passive Microwave Sensors. *Journal of Applied Meteorology* **40**, 1801-1820 (2001).
84. M. Deng, G. G. Mace, Z. Wang, E. Berry, CloudSat 2C-ICE product update with a new Ze parameterization in lidar-only region. *Journal of Geophysical Research: Atmosphere* **120(23)**, 12198-12208 (2015).
85. B. Marchant, S. Platnick, K. Meyer, G. Thomas Arnold, J. Riedi, MODIS Collection 6 shortwave-derived cloud phase classification algorithm and comparisons with CALIOP. *Atmospheric Measurement Techniques* **9**, 1587-1599 (2016).
86. S. Platnick *et al.*, http://modis-atmos.gsfc.nasa.gov/_docs/C6MOD06OPUserGuide.pdf (2015).
87. B. Yi, A. D. Rapp, P. Yang, B. A. Baum, M. D. King, A comparison of Aqua MODIS ice and liquid water cloud physical and optical properties between collection 6 and collection 5.1: Cloud radiative effects. *Journal of Geophysical Research: Atmospheres* **122(8)**, 4550-4564 (2017).
88. R. F. Adler *et al.*, The Version-2 Global Precipitation Climatology Project (GPCP) Monthly Precipitation Analysis (1979-Present). *Journal of Hydrometeorology* **4**, 1147-1167 (2003).
89. R. F. Adler, J. J. Wang, G. Gu, G. J. Huffman, A ten-year tropical rainfall climatology based on a composite of TRMM products. *Journal of the Meteorological Society of Japan* **87A**, 281-293 (2009).
90. G. J. Huffman, D. T. Bolvin, E. J. Nelkin, D. B. Wolff, R. F. Adler, The TRMM Multisatellite Precipitation Analysis (TMPA): Quasi-global, multiyear, combined-sensor precipitation estimates at fine scales. *Journal of Hydrometeorology* **8(1)**, 38-55 (2007).
91. T. Iguchi *et al.*, An overview of the precipitation retrieval algorithm for the Dual frequency Precipitation Radar (DPR) on the Global Precipitation Measurement (GPM) mission's core satellite. *Proc. SPIE 8528, Earth Observing Missions and Sensors: Development, Implementation, and Characterization II* **8528**, 85281C (2012).
92. W. B. Rossow, R. A. Schiffer, Advances in Understanding Clouds from ISCCP. *Bulletin of the American Meteorological Society* **80(11)**, 2261-2288 (1999).
93. F. J. Wentz, M. Schabel, Precise climate monitoring using complementary satellite data sets. *Nature* **403**, 414-416 (2000).
94. F. J. Wentz, L. Ricciardulli, K. Hilburn, C. Mears, How Much More Rain Will Global Warming Bring? *Science* **317(5835)**, 233-235 (2007).
95. Y. Cai *et al.*, Holocene moisture changes in western China, Central Asia, inferred from stalagmites. *Quaternary Science Reviews* **158**, 15-28 (2017).

Acknowledgments

We thank NASA GISS and the NASA Center for Climate Simulation for institutional support.

Funding:
NASA Data for Operations and Assessments grant NNX17AF46G (GSE)
Science of Terra, Aqua and Suomi NPP Program grant 80NSSC18K1030 (GSE)
Precipitation Measurement Mission grant RTOP WBS #573945.04.18.03.60 (GSE)
National Science Foundation Paleo Perspectives on Climate Change (P2C2) Award Number 1805544 (MLG)

Author contributions:
- Conceptualization: ANL, GSE, JN, MLG
- Methodology: RDR, ANL, MLG, GSE, DTL, JN
- Investigation: RDR, ANL, MLG, GSE
- Visualization: RDR, GSE
- Supervision: ANL, MLG, GSE, JET, FSRP
- Writing—original draft: RDR, ANL, GSE
- Writing—review & editing: RDR, ANL, MLG, GSE, DTL, JET, FSRP, JN

Competing interests: Authors declare that they have no competing interests.

Data and materials availability: All data needed to evaluate the conclusions of the paper are available in the main text and/or the supplementary materials. Additional data and corresponding analysis of the model outputs related to this paper maybe requested from the authors.

Figures and Tables

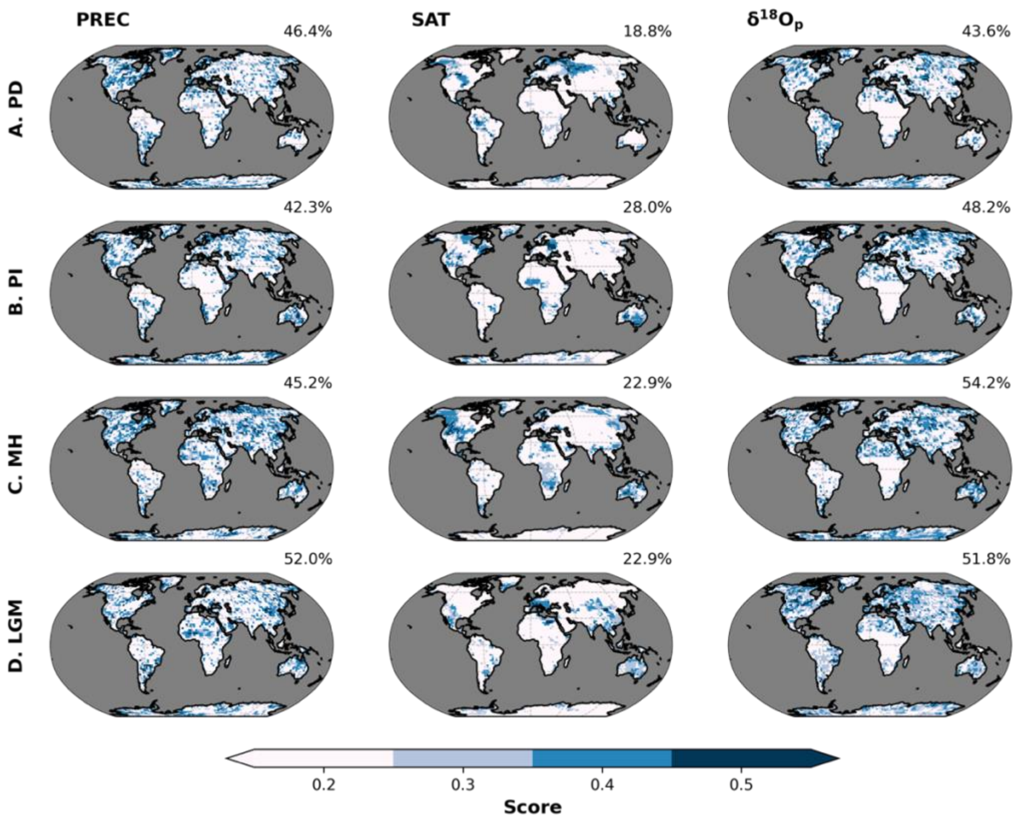

Fig. 1. Spatial sensitivity of precipitation (PREC), surface air temperature (SAT), and $\delta^{18}O_p$ to perturbed cloud and convective parameters for different time periods (A-D). Shading represents the scores or the fraction of the total number of ensembles per grid box showing significant difference from the PPE mean. The higher the score, the more sensitive a location is to parameter changes. The oceans are masked to highlight changes on land for these atmosphere-only simulations. Percentages reported at the top right of each panel indicate the fraction of land surface (using PD configuration) having a score greater than 0.2.

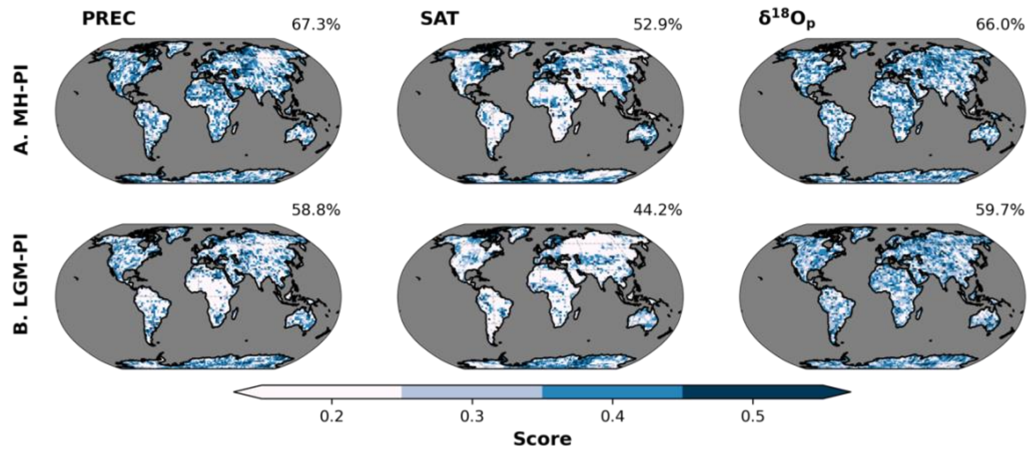

Fig. 2. Spatial sensitivity of precipitation (PREC), surface air temperature (SAT), and $\delta^{18}O_p$ to perturbed cloud and convective parameters for (A) MH-PI and (B) LGM-PI. Shading represents the scores or the fraction of the total number of ensembles per grid box showing significant difference from the PPE mean. The higher the score, the more sensitive a location is to parameter changes. The oceans are masked to highlight changes on land for these atmosphere-only simulations. Percentages reported at the top right of each panel indicate the fraction of land surface (using PD configuration) having a score greater than 0.2.

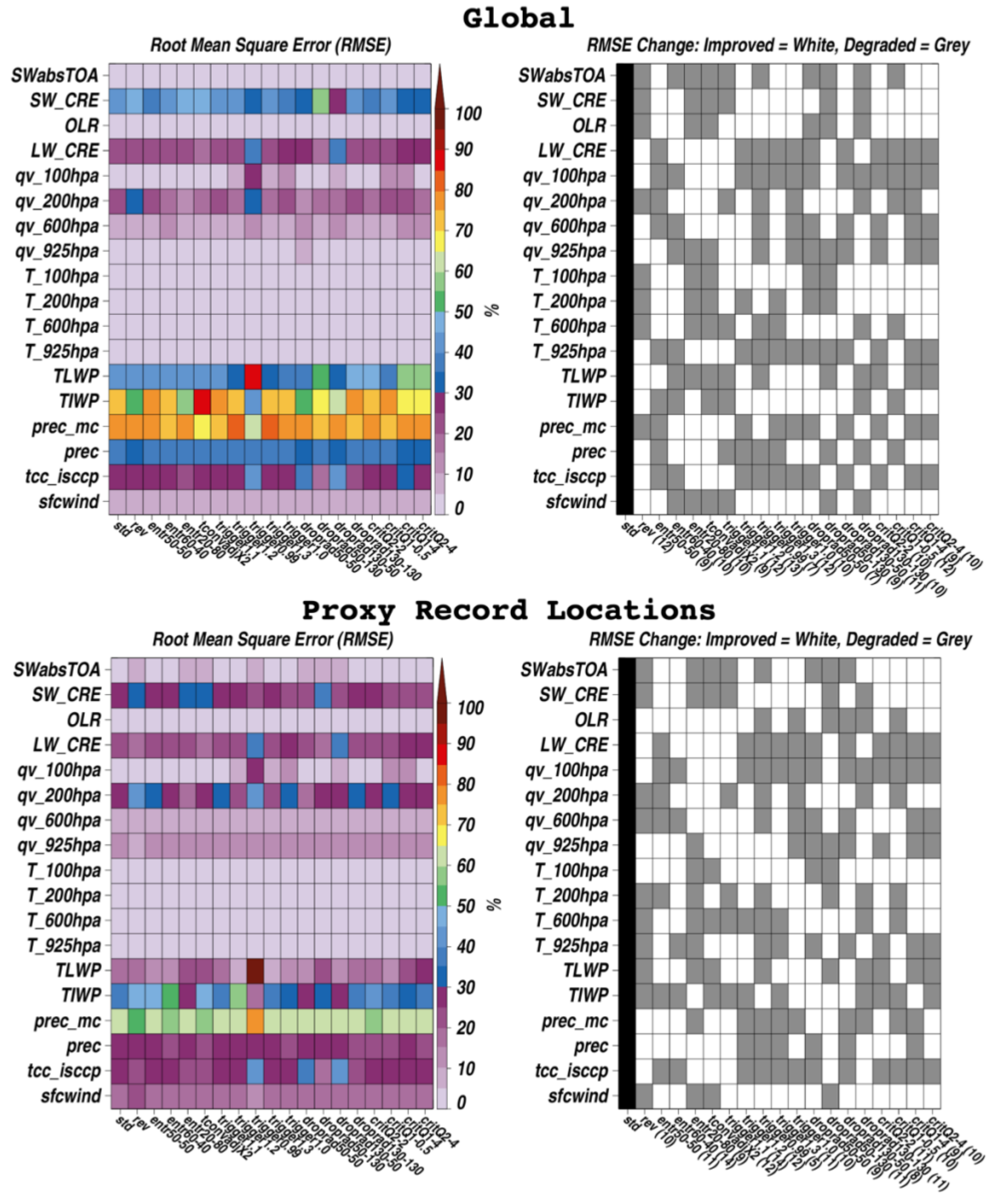

Fig. 3. Comparison of model with satellite data. (top left) Global model-satellite RMSE scores for absorbed shortwave (SW) radiation at the top of the atmosphere (SWabsTOA), SW cloud radiative effects (SW_CRE), outgoing longwave radiation (OLR), longwave (LW)_CRE, water vapor (qv) and temperature (T) at various levels, total (cloud+precipitating) liquid and ice water paths (TLWP, TIWP), convective and total precipitation (prec_mc, prec), ISCCP satellite cloud cover (tcc_isccp), and 10-meter surface wind speeds (sfcwind). (top right) binary white-gray shading indicating if RMSE scores improved for a given ensemble member relative to *std*, with numbers indicating the number of metrics exhibiting improvement. (bottom row) As in the top row, but only for model and satellite grid boxes co-located with paleo-proxy sites.

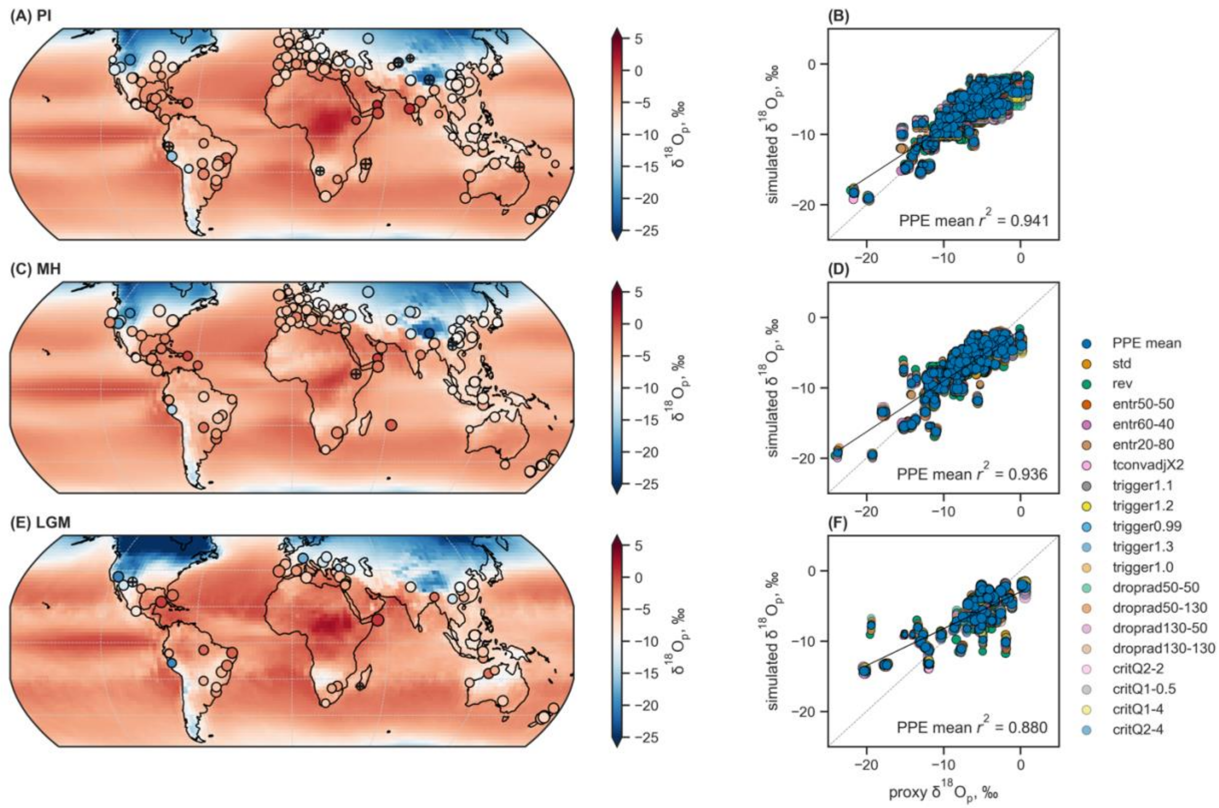

Fig. 4. Comparison of simulated $\delta^{18}O_p$ with speleothem $\delta^{18}O$. Global distribution of simulated $\delta^{18}O_p$ (background) and speleothem $\delta^{18}O$, converted to their drip water equivalents (See Materials and Methods) under (A) PI (n = 257), (C) MH (n = 195) and (E) LGM (n = 81) conditions. Background and extracted data points are from the PPE mean. SISAL $\delta^{18}O$ points with standard deviation greater than 1 are marked with '+'. Scatterplots between simulated and proxy $\delta^{18}O_p$ for the respective time periods (B, D, F). PPE members are differentiated by color. Black lines represent the weighted least squares regression fits to data points while the gray dashed lines represent the 1:1 line. Weighted r^2 for the PPE mean is reported in the lower right corner of each scatterplot. The size of the circles in all plots are scaled to the sensitivity scores derived in Fig. 1. Results for each ensemble member are in the supplementary materials (fig. S6-a to S6-s).

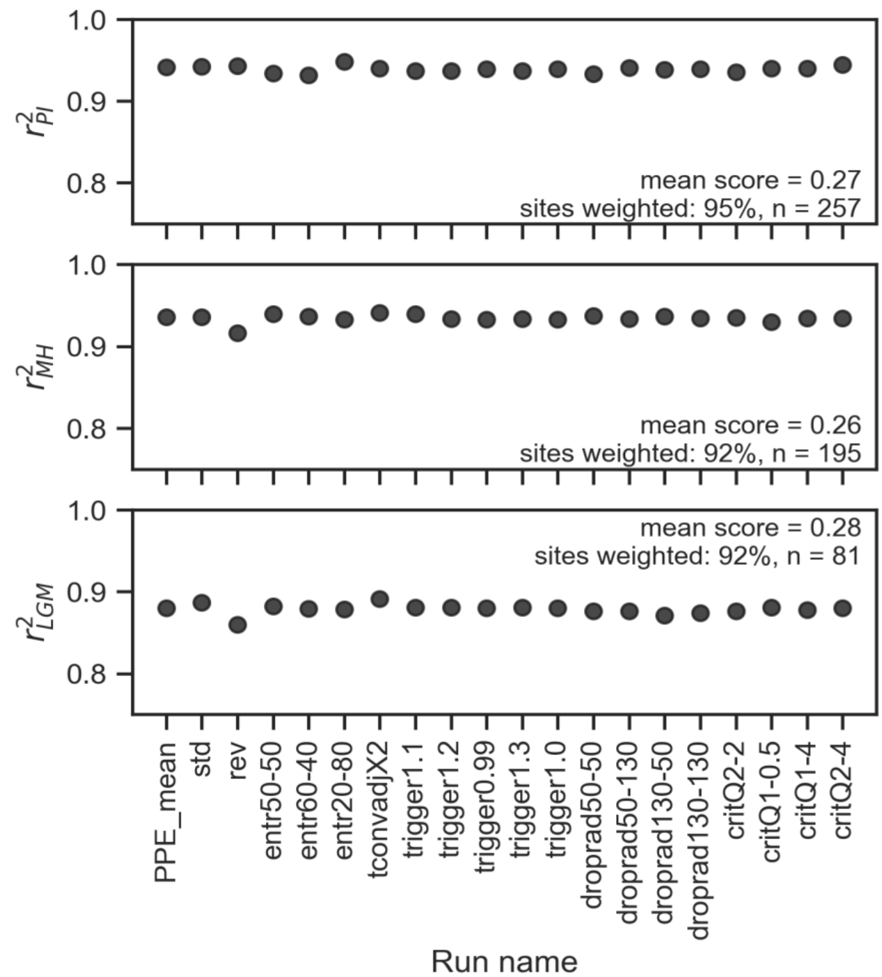

Fig. 5. Weighted r^2 values between simulated $\delta^{18}O_p$ and SISAL $\delta^{18}O$. All speleothem $\delta^{18}O$ were converted to their drip water equivalent.

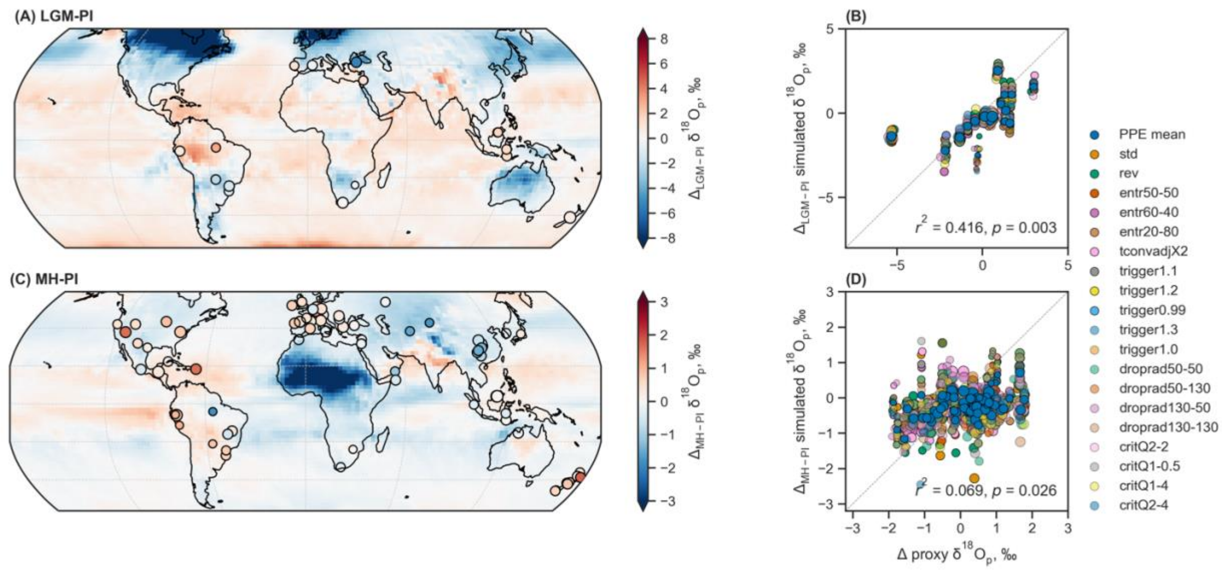

Fig. 6. Comparison of simulated $\delta^{18}O_p$ anomalies (background) with speleothem $\delta^{18}O$ (filled circles) for each time slices: (A) LGM-PI (n = 17), (C) MH-PI (n = 79). Background and extracted data points are from the PPE mean. Scatterplots between simulated and proxy $\delta^{18}O_p$ for the respective time periods (B, D). PPE members are differentiated by color. Gray dashed lines represent the 1:1 line. Weighted r^2 for the PPE mean is reported in the lower right corner of each scatterplot. The size of the circles in all plots are scaled to the sensitivity scores derived in Fig. 2.

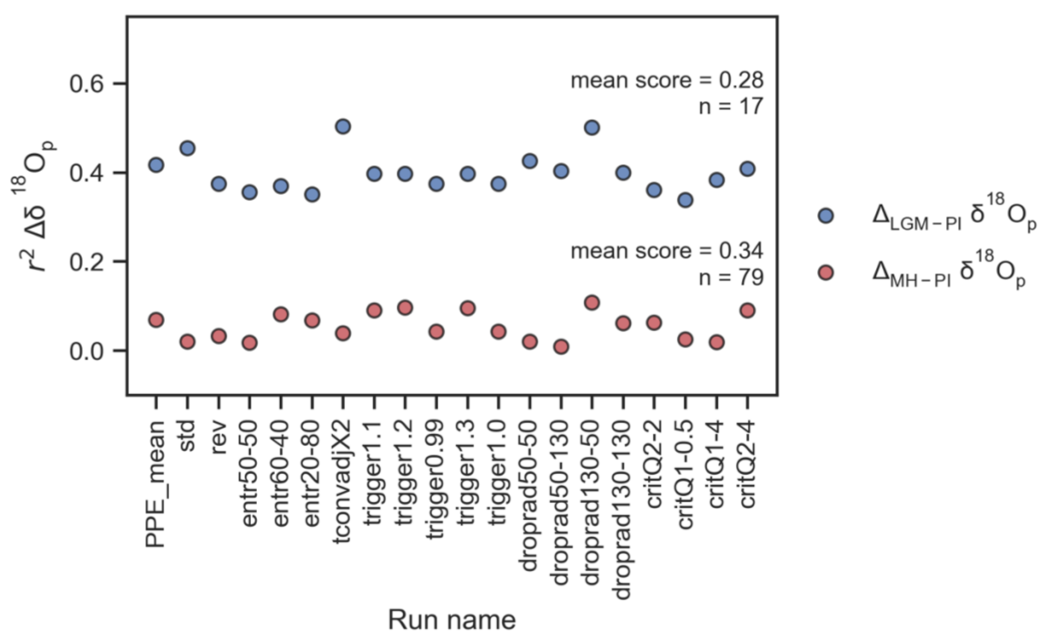

Fig. 7. Weighted r^2 values between simulated $\delta^{18}O_p$ and SISAL $\delta^{18}O$ anomalies.

Table 1. Parameter space exploration of GISS-E2.1.

Short Name	Parameter	GISS-E2.1 default	New Value	Mean Surface Air Temperature, °C (global, NH, SH)	Mean Precipitation, mm/day (global, NH, SH)	Radiation balance at TOA, W/m^2 (PI, MH, LGM)
std	standard	----	----	13.99,14.31,13.67	2.96,2.88,3.03	0.098,0.663,-1.92
rev	rain re-evaporation above cloud base	On (1)	Off (0)	13.80,14.04,13.53	2.94,2.84,3.05	0.013,0.094,1.46
entr50-50	entrainment rate for plume (1 & 2)	0.4; 0.6	0.5; 0.5	13.98.14.29,13.66	2.98,2.90,3.06	0.168,-0.04,-2.00
entr60-40			0.6; 0.4	14.02,14.33,13.70	2.95,2.87,3.02	-0.156,-0.304,-2.20
entr20-80			0.2; 0.8	14.00,14.28,13.72	2.91,2.82,3.01	0.134,0.018,-1.80
tconvadjX2	convection adjustment time	1	2	14.00,14.28,13.72	2.97,2.86,3.06	0.107,-0.062,-2.08
trigger1.1	convective trigger	2	1.1	13.96,14.29,13.63	2.98,2.90,3.06	0.289,0.061,-1.98
trigger1.2			1.2	13.96,14.29,13.62	2.98,2.90,3.06	0.289,0.162,-1.98
trigger0.99			0.99	13.98,14.30,13.66	2.98,2.89,3.06	0.046,-0.101,-2.11
trigger1.3			1.3	13.97,14.28,13.66	2.98,2.91,3.05	0.289,0.162,-1.98
trigger1.0			1.0	13.98,14.30,13.66	2.98,2.90,3.06	0.047,-0.101,-2.11
droprad50-50	cloud droplet radius (liquid- ice)	1; 1	0.5; 0.5	13.87,14.11,13.62	2.87,2.76,2.98	-0.194,-0.52,-2.92
droprad50-130			0.5; 1.3	14.17,14.52,13.82	2.91,2.81,3.00	0.249,0.067,-1.54
droprad130-50			1.3; 0.5	13.76,14.00,13.53	2.97,2.89,3.05	-0.164,-0.475,-2.96
droprad30-130			1.3; 1.3	14.01,14.36,13.67	2.99,2.91,3.06	0.032,-0.625,-1.80
critQ2-2	critical cloud water content (liquid & ice)	2; 1	2; 2	14.00,14.32,13.68	2.96,2.86,3.05	0.085,-0.153,-2.12
critQ1-0.5			1; 0.5	14.00,14.34,13.67	2.99,2.90,3.08	0.181,0.135,-1.92
critQ1-4			1; 4	13.95,14.26,13.64	2.96,2.87,3.06	-0.020,-0.168,1.13
critQ2-4			2; 4	13.96,14.30,13.63	2.95,2.85,3.05	0.142,-0.04,-2.23

Table 2. Summary of forcing and boundary conditions for each time slice experiment. All experiments applied topography, bathymetry, land-ocean-ice mask, greenhouse gas, river routing and appropriate SMOW changes.

Time slice	**Ice sheet**	**SST/SICE**	**GHG**	**Mean salinity, psu**	**SMOW (δ^{18}O, δD)**
Present Day	modern	Hadley Obs	year 2000	34.7	0‰, 0‰
PI, 0 ka	modern	CMIP6: PI	year 1850	34.7	0‰, 0‰
MH, 6 ka	modern	CMIP6: MH	6 ka	34.7	0‰, 0‰
LGM, 21 ka	Glac1D	CMIP6: LGM	21 ka	35.7	1.0‰, 8.0‰

Supplementary Materials for

Constraining clouds and convective parameterizations in a climate model from past climate

Riovie D. Ramos*, Allegra N. LeGrande*, Michael L. Griffiths*, Gregory S. Elsaesser, Daniel T. Litchmore, Jessica E. Tierney, Francesco S. R. Pausata and Jesse Nusbaumer

*Corresponding authors. Email: Riovie D. Ramos (ramosr34@wpunj.edu); Allegra N. LeGrande (allegra.n.legrade@nasa.gov); Michael L. Griffiths (griffithsm@wpunj.edu)

This PDF file includes:

Supplementary Text S1. Spatial variability and sensitivity to perturbations in clouds and convective parameterizations: balanced versus unbalanced versions

Using the balanced version, the largest variability in precipitation (PREC) in our PPE runs occurs over the tropics including the Intertropical Convergence Zone (ITCZ), the South Pacific Convergence Zone (SPCZ) and the Maritime Continent in all time periods (Fig. S1). For surface air temperature (SAT), high variability regions are confined over the continents – an expected consequence of prescribing sea surface temperatures in our simulations. In all time periods, the largest variability occurs over interior Antarctica, Greenland, and Siberia (Fig. S1). Relative to the PI period, this variability during the LGM is amplified over Siberia Arctic Ocean and Himalayas – a surprise that clouds and convective parameters, thought to be most important in the tropics and convective zones, should be so sensitive to the difference in glacial ice sheet extent. For $\delta^{18}O_p$, large variability occurs over the tropics around the 20° latitude bands in both hemispheres with a maximum spread over the western and central Africa in all time periods (Fig. S1). These observations are consistent with the unbalanced version, but the overall variability is amplified across all variables and periods (Fig. S2). In addition, $\delta^{18}O_p$ variability over the high latitude regions during the LGM exhibits the largest standard deviation (Fig. S2).

The overall large spatial variability in the unbalanced version has resulted in more regions of low sensitivity scores (Fig. S3 and S4), likely induced by random noise from perturbing parameters without re-tuning to radiative equilibrium, which limits how far these parameters push the climate system. This high standard deviation reduces the number of sites that can constrain model biases associated with different cloud and convective parameter choices given our criteria that the spread amongst ensemble members themselves exceed the standard deviation within a single simulation, and thus are less desirable particularly in considering paleoclimate simulations with larger forcing.

An analysis of satellite scoring metrics reveals some systematic variations in scores for the PPE runs that are not re-balanced relative to the balanced PPE (Fig. S5). For the balanced runs, for any given variable, there is a “checkerboard” appearance in the skill scores (i.e., more alternating improvement and degradation in the RMSE change plots) such that for one given run, there is more randomness to the skill score changes upon balancing. The opposite is observed for the unbalanced runs, where the impact of changing one physical parameter has a clearer systematic impact on aggregated groups of cloud, precipitation or thermodynamic variables. One interpretation is that the act of balancing, which requires a perturbation of a parameter not initially perturbed, adds dimensionality to the impacts and may sometimes enhance or remove the initial impact of the parameter tuning, thus adding noise to the skill scores. Furthermore, the overall changes in the skill scores are smaller when considering the proxy sites only (Fig. S5). Thus, not only is a less convectively active atmosphere easier to simulate; it may also be less susceptible to further changes in the new climatological states upon re-balancing.

Overall, the variations in scores from a balanced PPE to unbalanced PPE does suggest that interpretations of climate model PPEs designed to be in agreement with (or at least directly comparable to) observations should consider whether the PPEs were balanced or not since the act of radiative balancing itself, a necessary procedure to create a usable climate model configuration, will likely remove a non-negligible percentage of the systematic changes induced by single parameter perturbation methods.

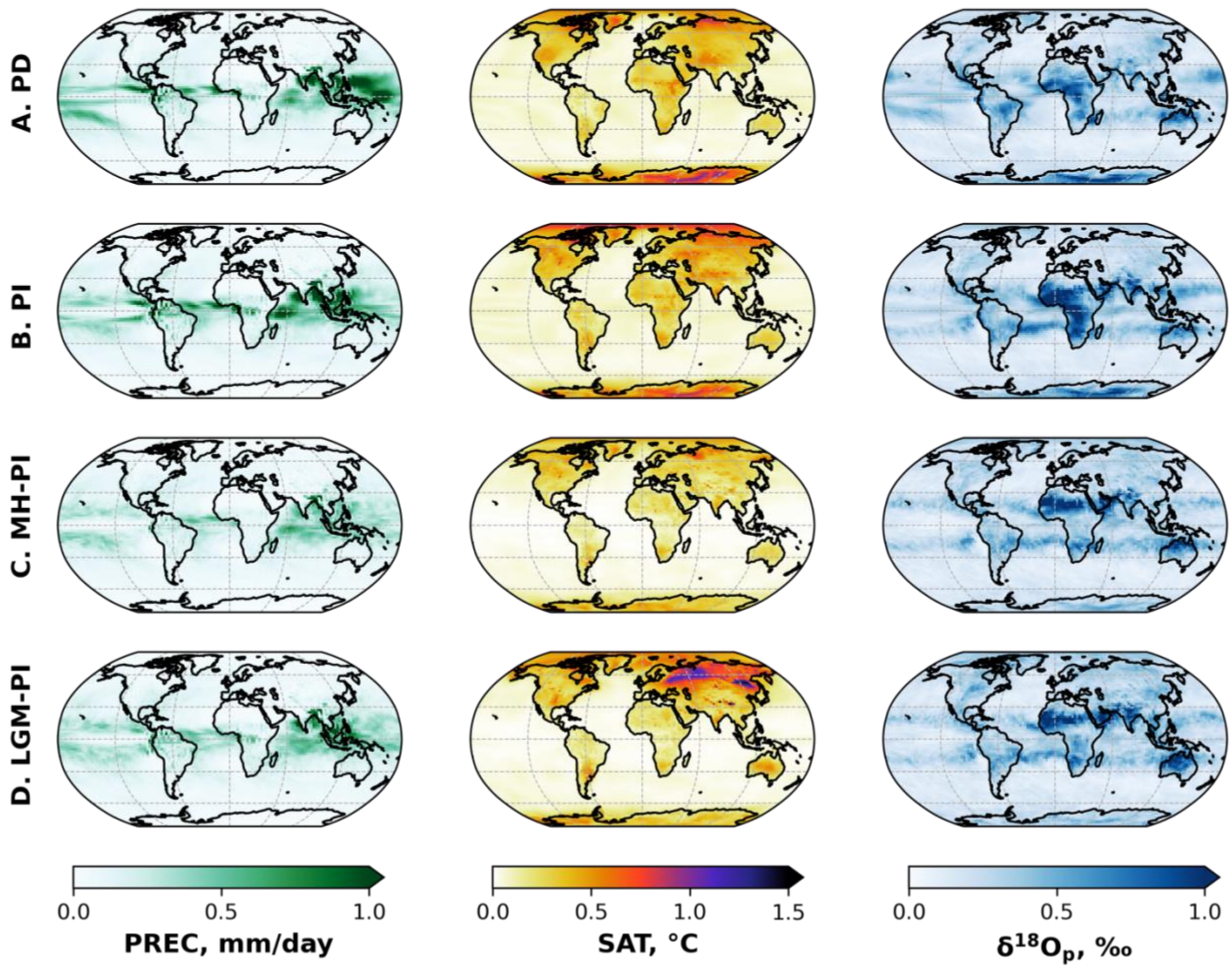

Fig. S1. Spatial variability of precipitation (PREC), surface air temperature (SAT), $\delta^{18}O_p$ using the balanced runs. A total of 19 simulations of different cloud and convective parameterizations were used to assess spatial variability (i.e., standard deviation) for each time period (A-D).

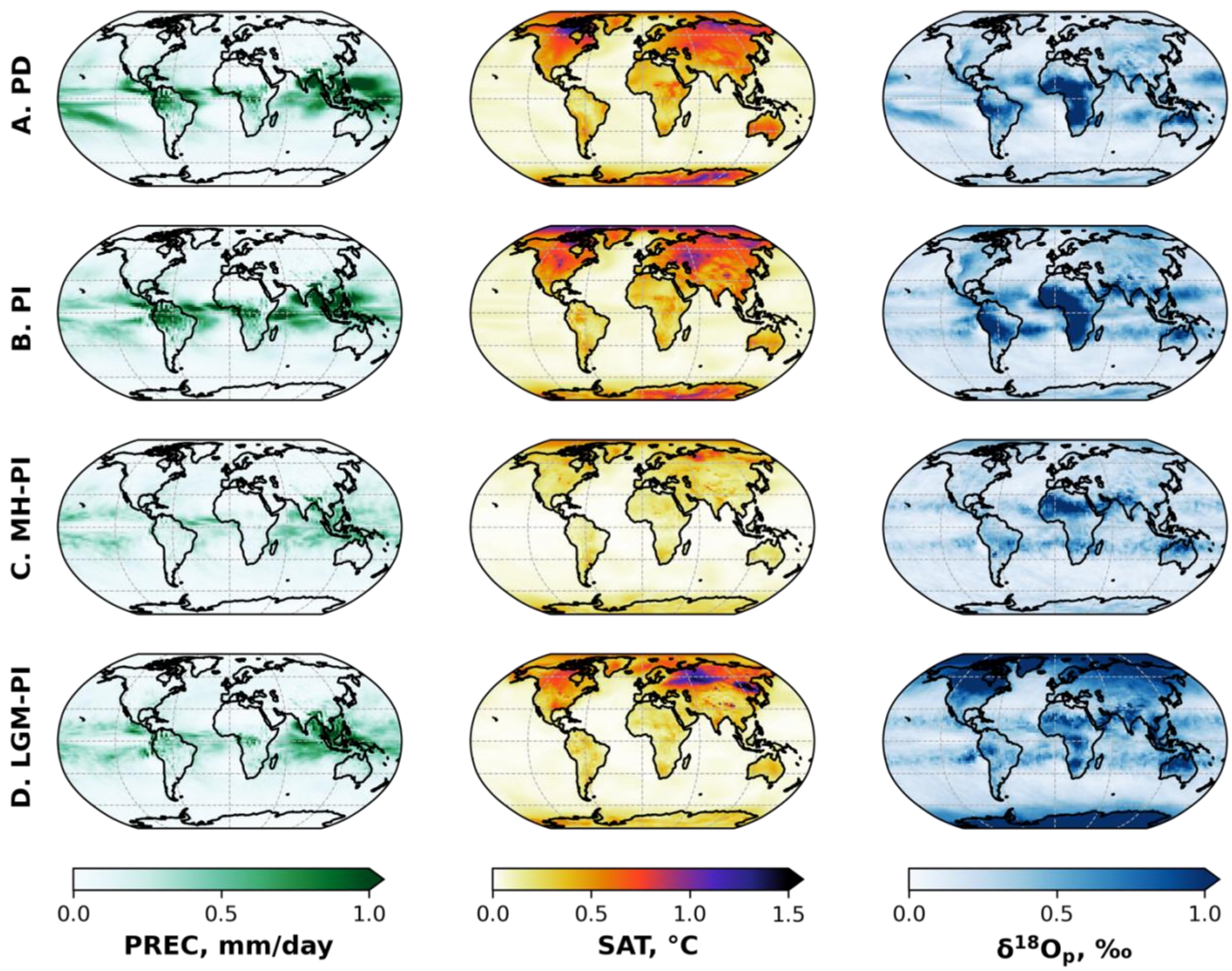

Fig. S2. Spatial variability of precipitation (PREC), surface air temperature (SAT), $\delta^{18}O_p$ using the unbalanced runs. A total of 19 simulations of different cloud and convective parameterizations were used to assess spatial variability (i.e., standard deviation) for each time period (A-D).

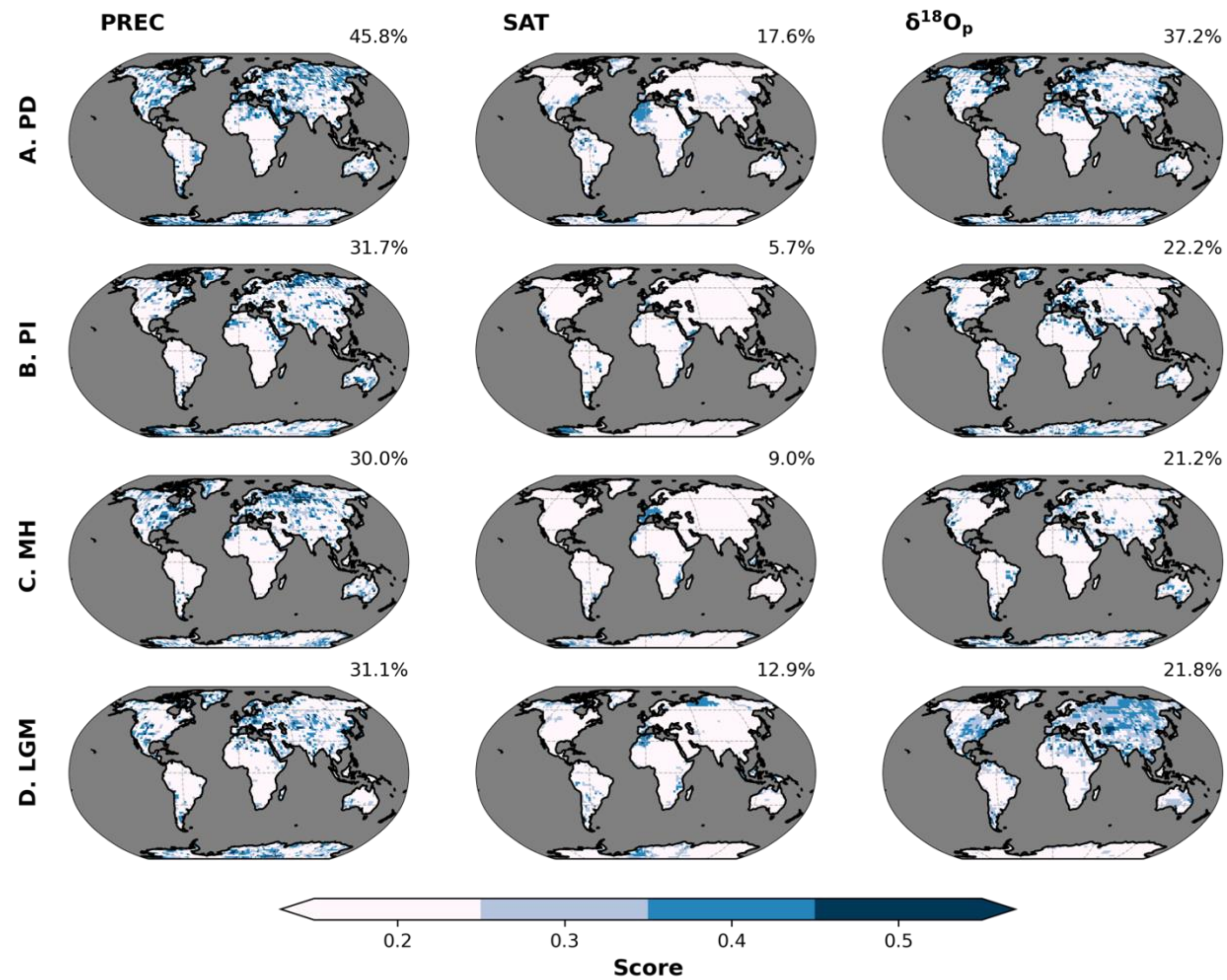

Fig. S3. Spatial sensitivity of precipitation (PREC), surface air temperature (SAT), and $\delta^{18}O_p$ to perturbed cloud and convective parameters for different time periods (A-D) using the unbalanced runs. Shading represents the scores or the fraction of the total number of ensembles per grid box showing significant difference from the PPE mean. The higher the score, the more sensitive a location is to parameter changes. The oceans are masked to highlight changes on land for these atmosphere-only simulations. Percentages reported at the top right of each panel indicate the fraction of land surface (using PD configuration) having a score greater than 0.2.

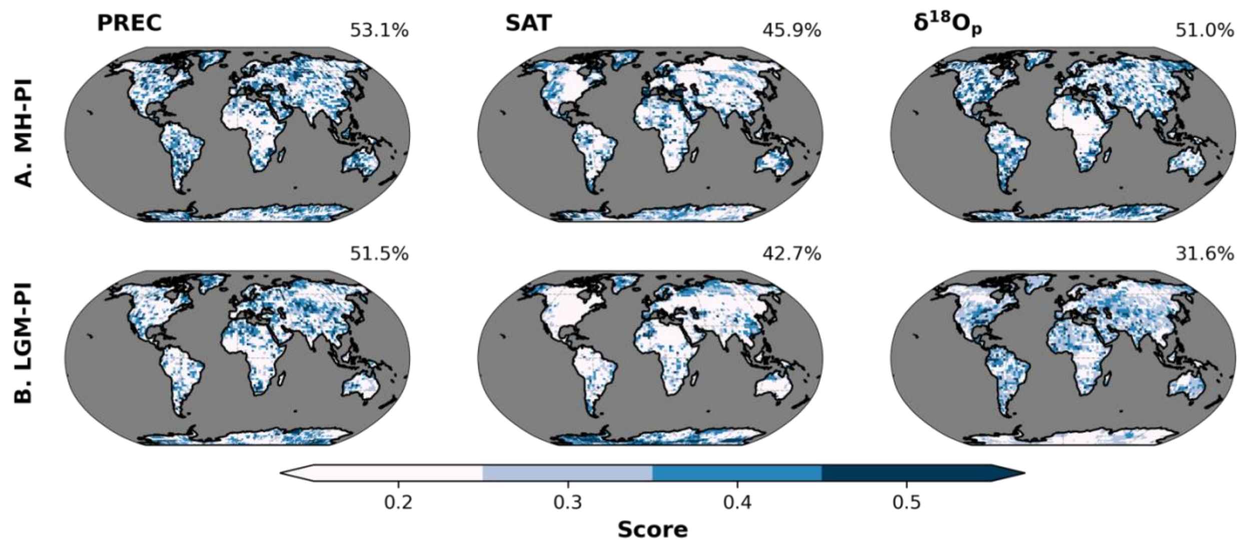

Fig. S4. Spatial sensitivity of precipitation (PREC), surface air temperature (SAT), and $\delta^{18}O_p$ to perturbed cloud and convective parameters for (A) MH-PI and (B) LGM-PI using unbalanced runs. Shading represents the scores or the fraction of the total number of ensembles per grid box showing significant difference from the PPE mean. The higher the score, the more sensitive a location is to parameter changes. The oceans are masked to highlight changes on land for these atmosphere-only simulations. Percentages reported at the top right of each panel indicate the fraction of land surface (using PD configuration) having a score greater than 0.2.

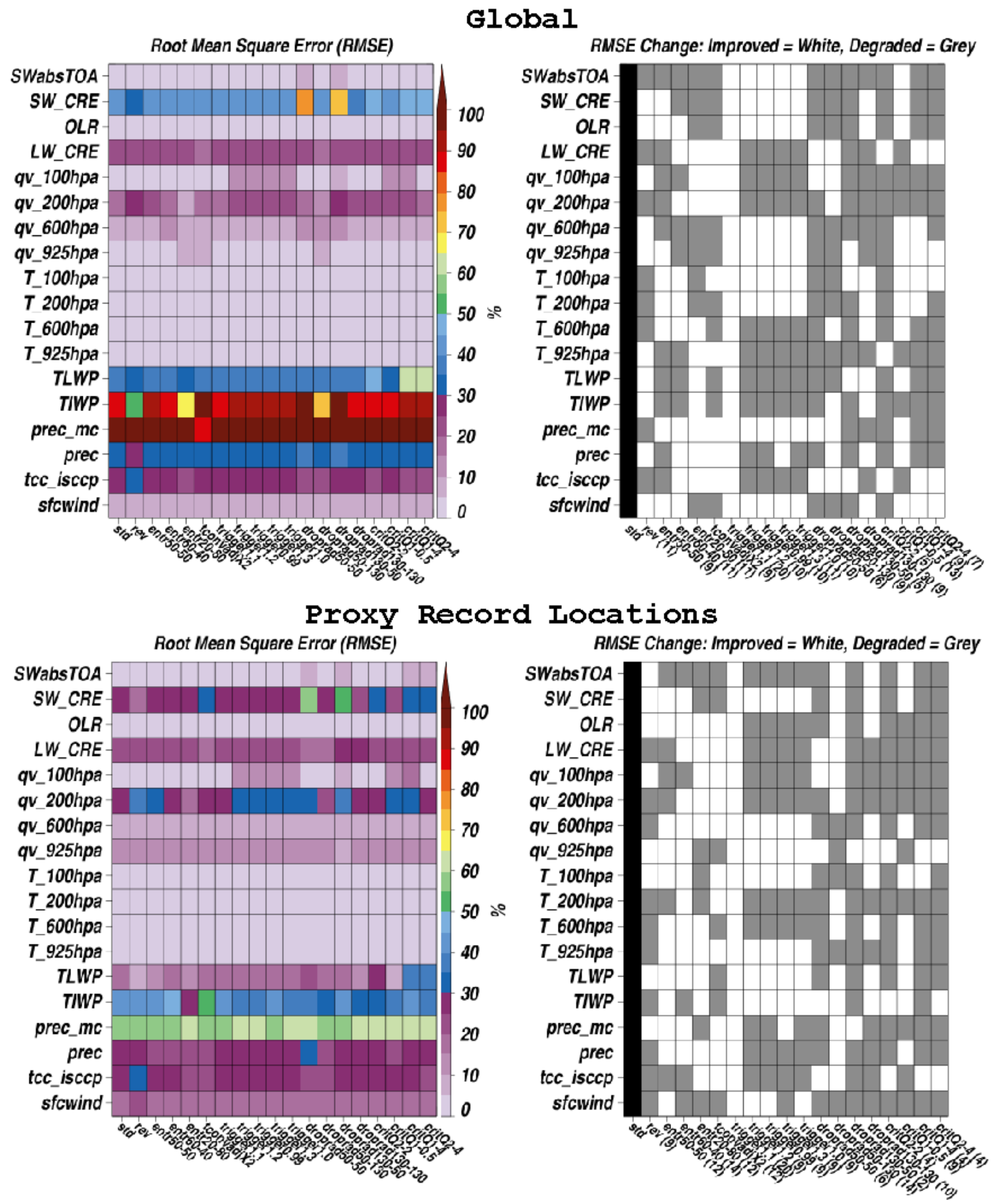

Fig. S5. Comparison of model with satellite data using unbalanced runs. (top left) Global model-satellite RMSE scores for absorbed shortwave (SW) radiation at the top of the atmosphere (SWabsTOA), SW cloud radiative effects (SW_CRE), outgoing longwave radiation (OLR), longwave (LW)_CRE, water vapor (qv) and temperature (T) at various levels, total (cloud+precipitating) liquid and ice water paths (TLWP, TIWP), convective and total precipitation (prec_mc, prec), ISCCP satellite cloud cover (tcc_isccp), and 10-meter surface wind speeds (sfcwind). (top right) binary white-gray shading indicating if RMSE scores improved for a given ensemble member relative to *std*, with numbers indicating the number of metrics exhibiting improvement. (bottom row) As in the top row, but only for model and satellite grid boxes co-located with paleo-proxy sites.

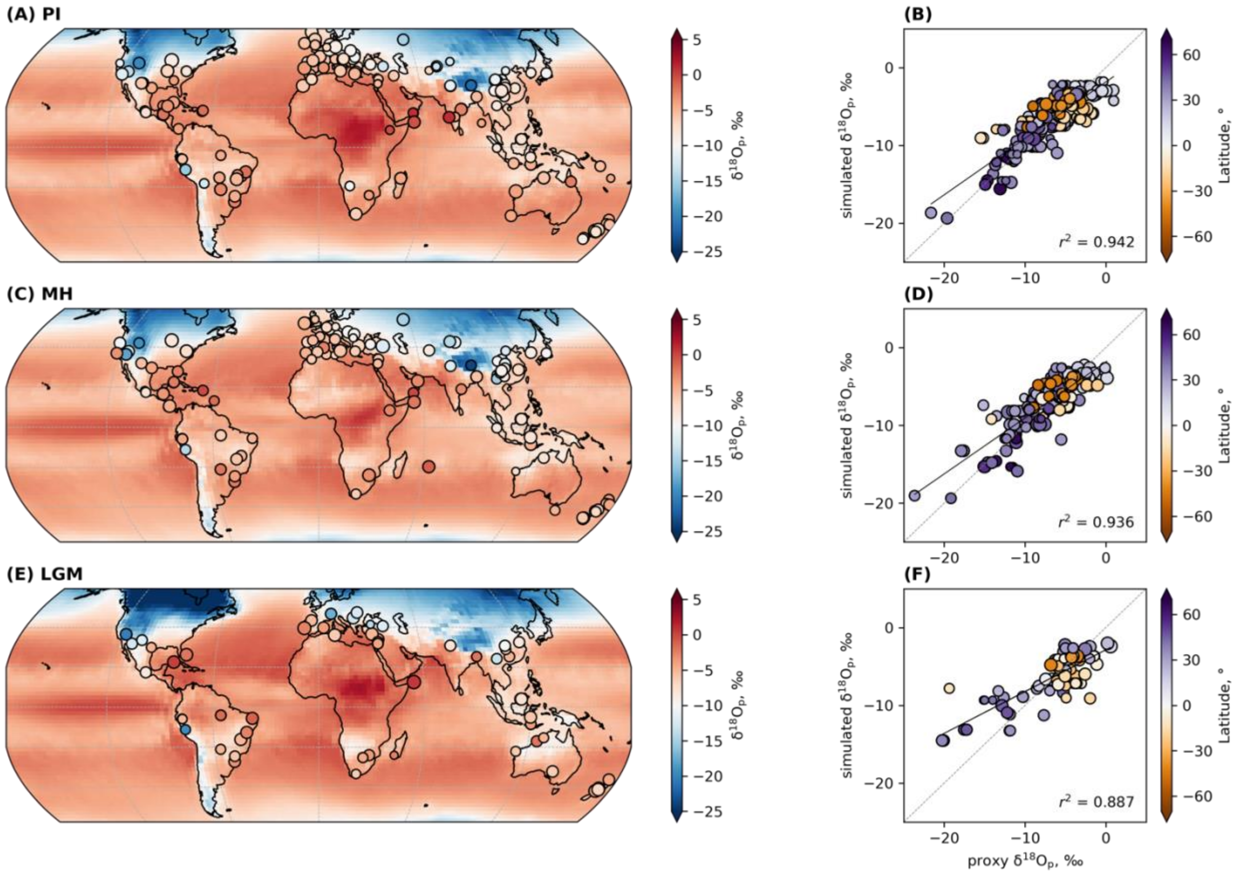

Fig. S6-a. Comparison of simulated $\delta^{18}O_p$ with speleothem $\delta^{18}O$ for the *standard (std)* parameterization. Global distribution of simulated $\delta^{18}O_p$ (background) and speleothem $\delta^{18}O$, converted to their drip water equivalents (See Materials and Methods) under (A) PI (*n* = 257), (C) MH (*n* = 195) and (E) LGM (*n* = 81) conditions. Scatterplots between simulated and proxy $\delta^{18}O_p$ for the respective time periods (B, D, F). Black lines represent the weighted least squares regression fits to data points while the gray dashed lines represent the 1:1 line. Weighted r^2 is reported in the lower right corner of each scatterplot. The size of the circles in all plots are scaled to the sensitivity scores derived in Fig. 1.

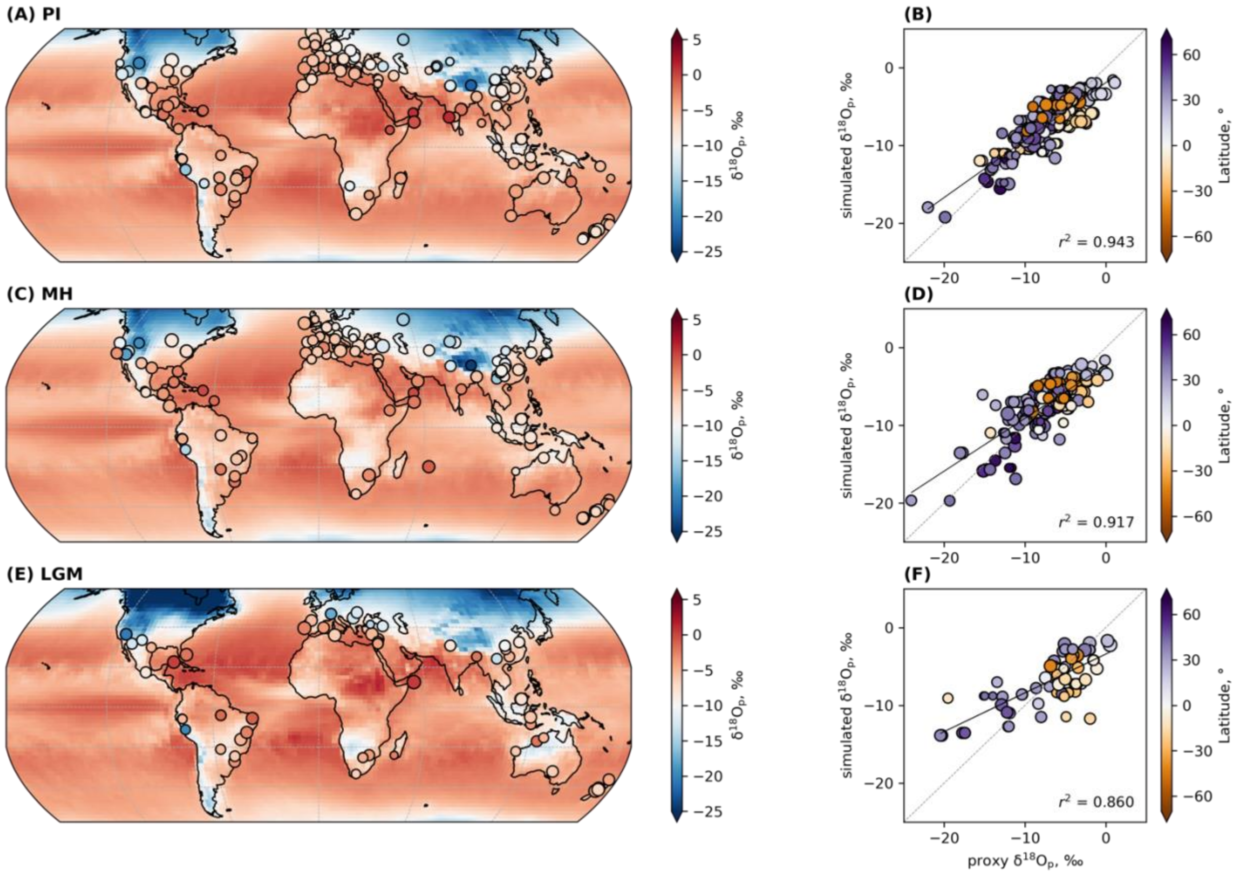

Fig. S6-b. Same as Fig. S2-a but for the *rain re-evaporation above the cloud base (rev)* parameterization.

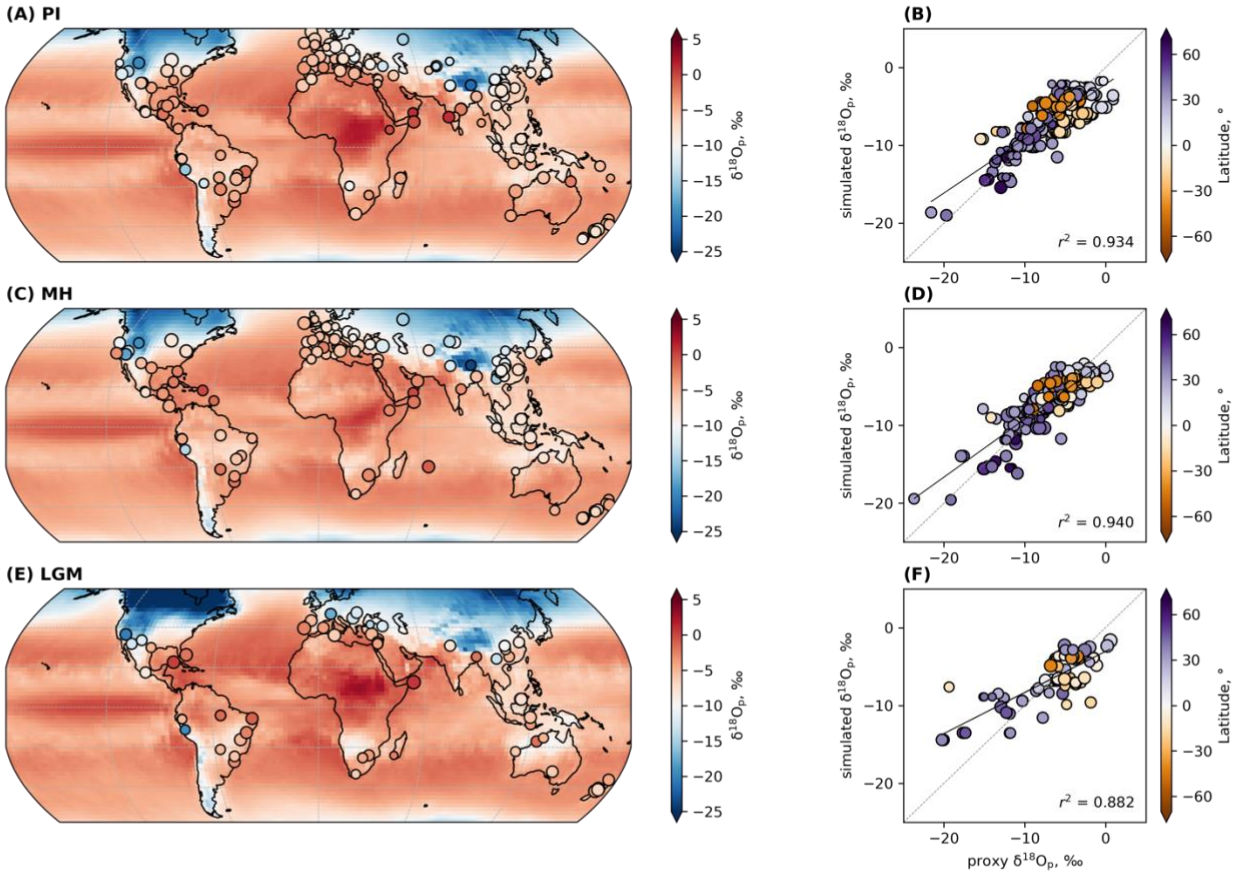

Fig. S6-c. Same as Fig. S6-a but for the *entrainment rate for plume (entr50-50)* parameterization.

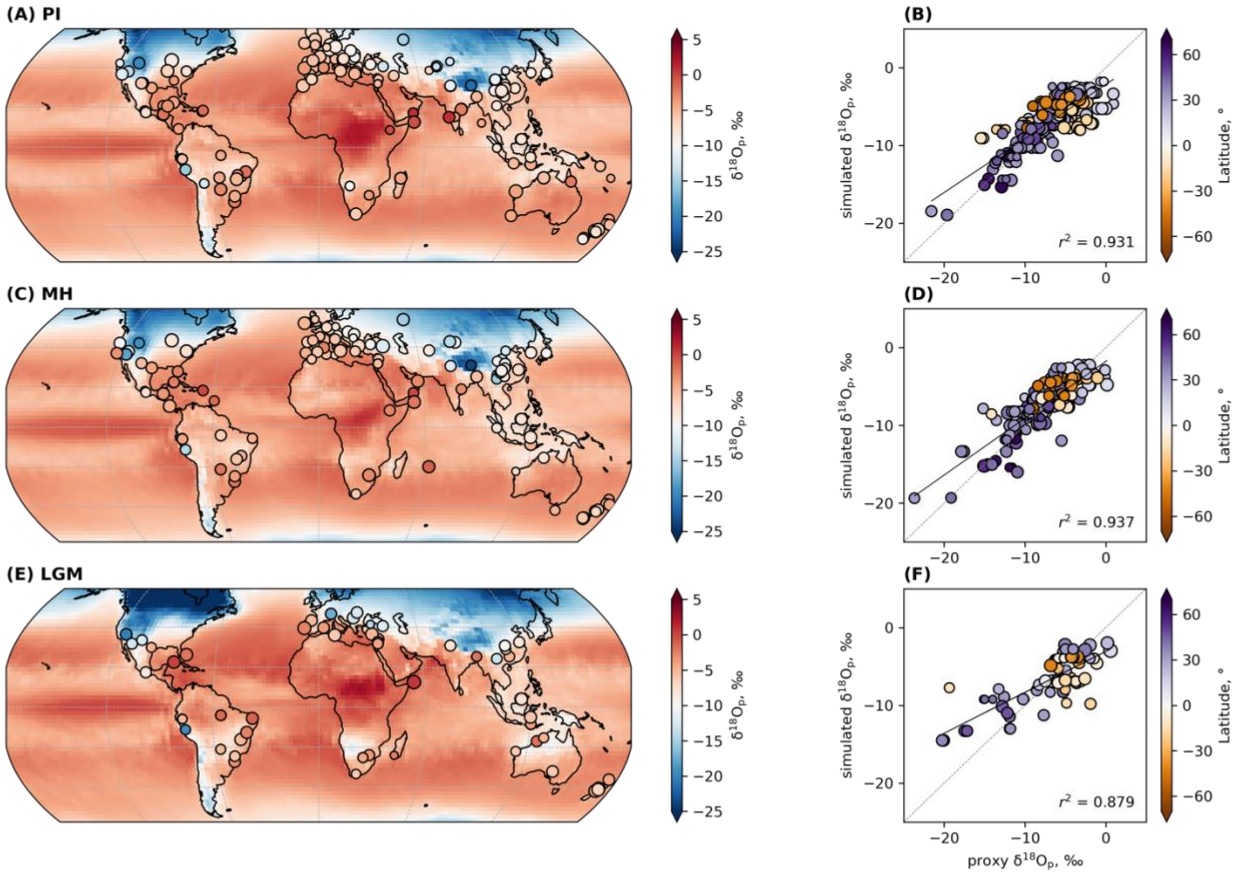

Fig. S6-d. Same as Fig. S6-a but for the *entrainment rate for plume (entr60-40)* parameterization.

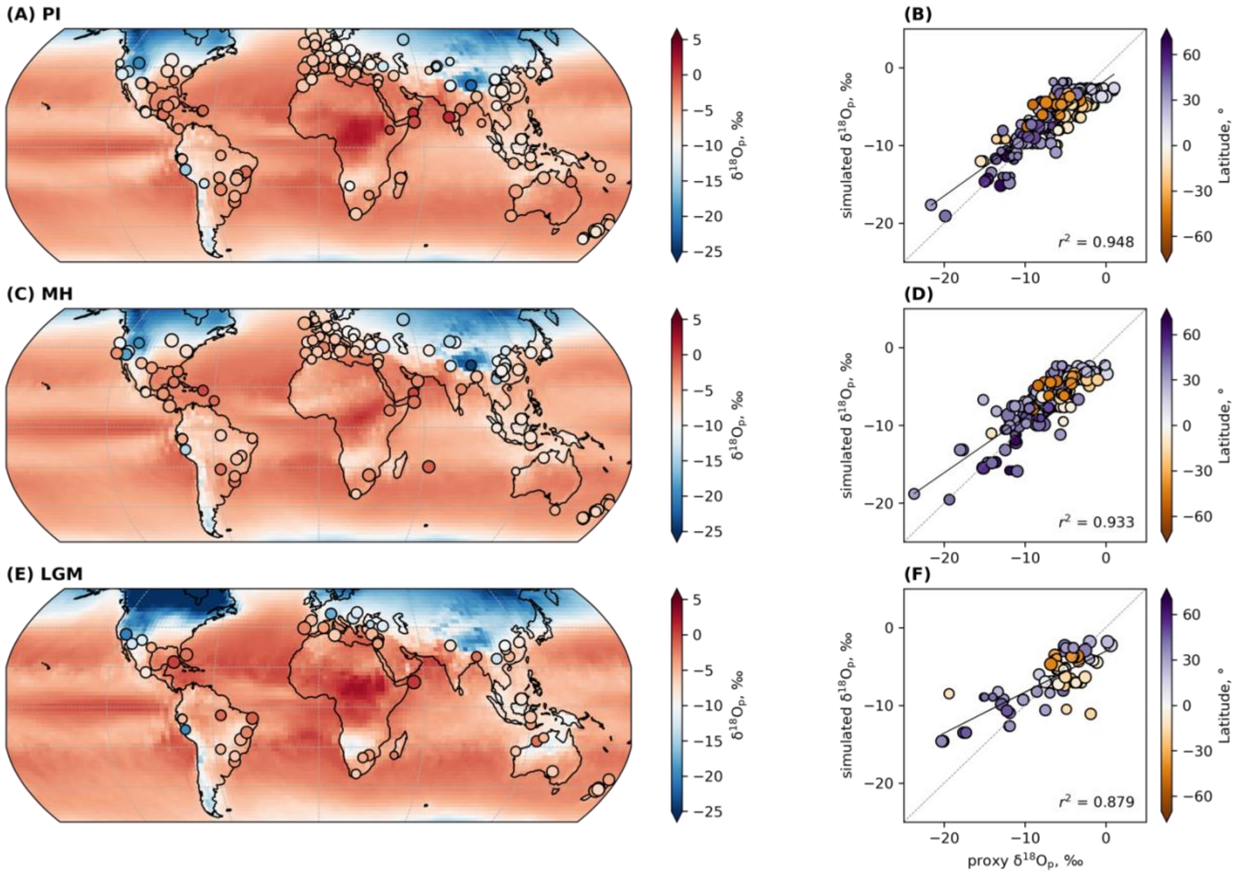

Fig. S6-e. Same as Fig. S6-a but for the *entrainment rate for plume (entr20-80)* parameterization.

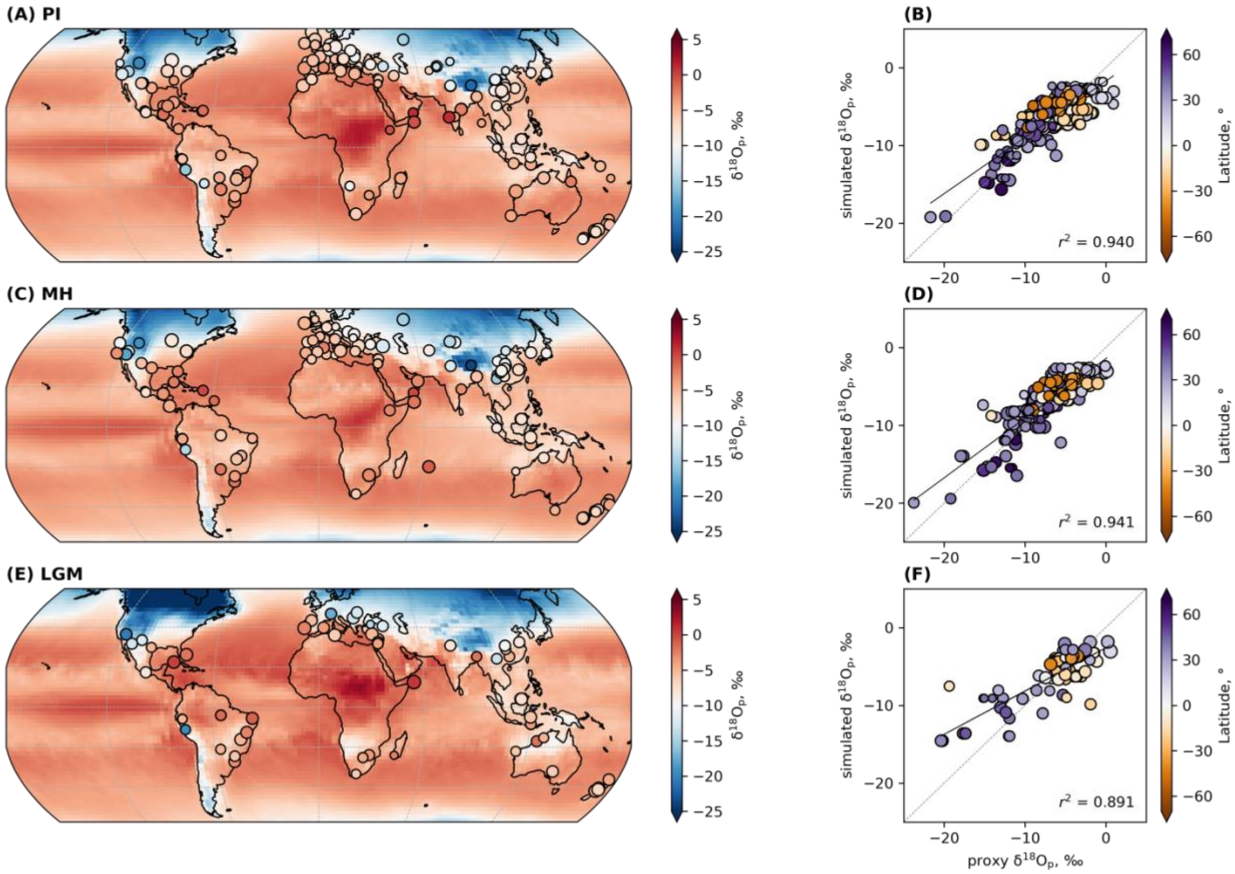

Fig. S2-f. Same as Fig. S6-a but for the *convection adjustment time (tconvadjX2)* parameterization.

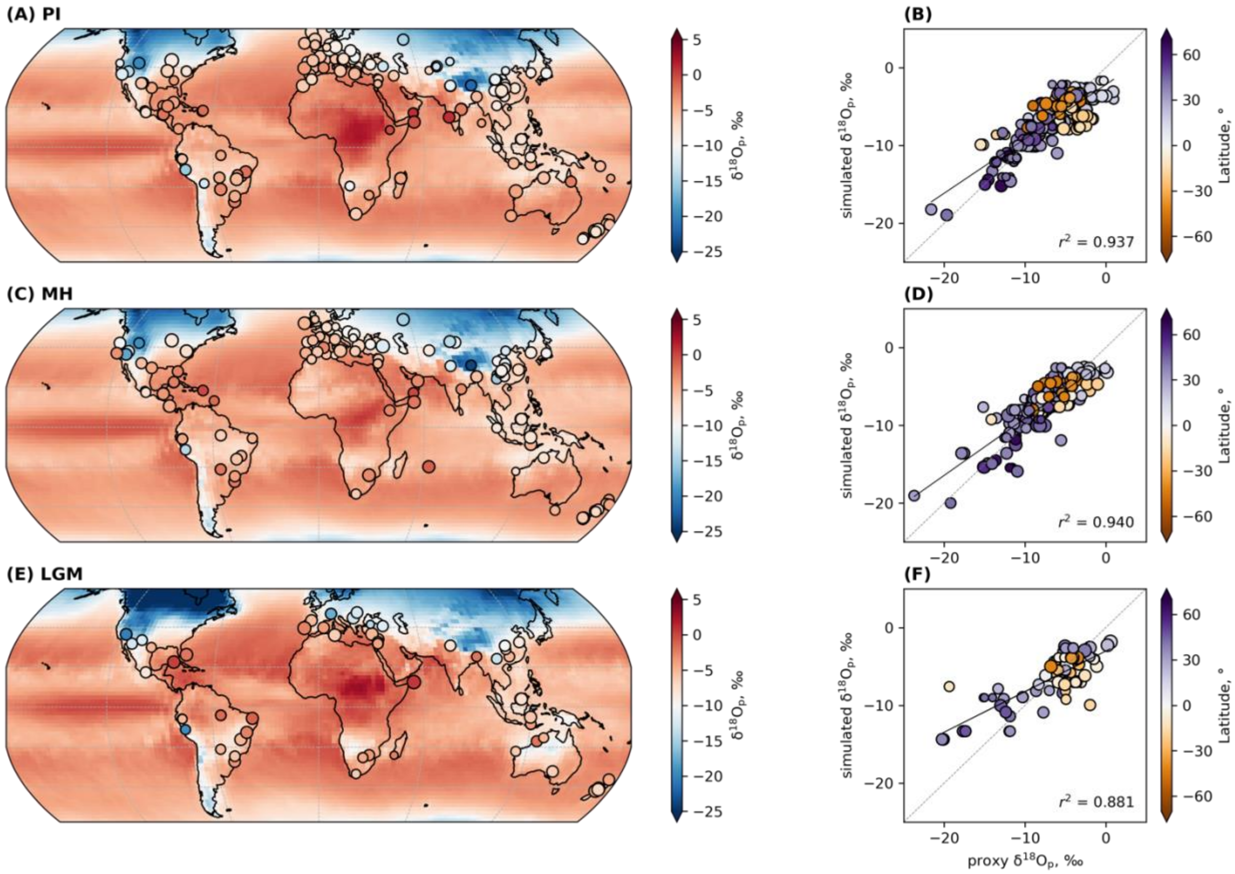

Fig. S6-g. Same as Fig. S6-a but for the *convective trigger (trigger1.1)* parameterization.

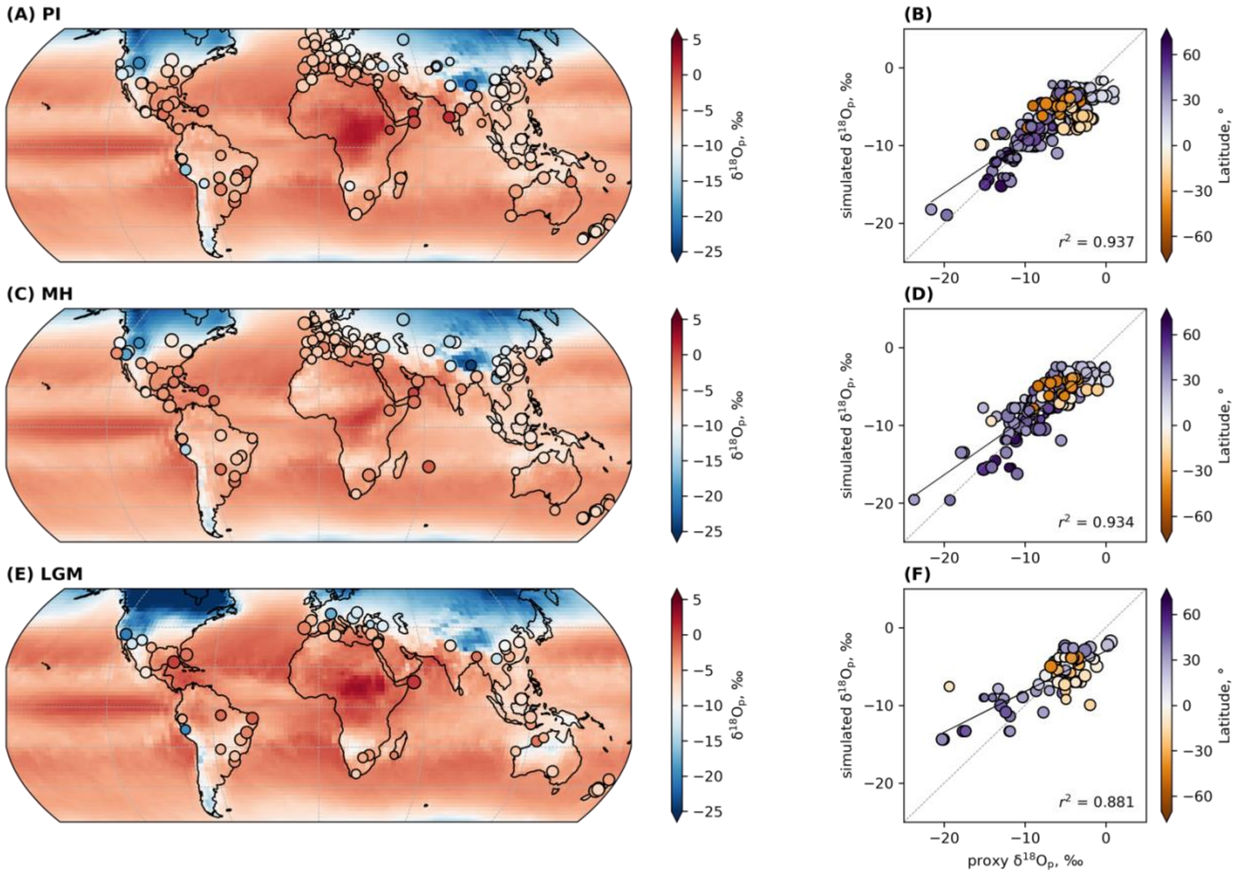

Fig. S6-h. Same as Fig. S6-a but for the *convective trigger (trigger1.2)* parameterization.

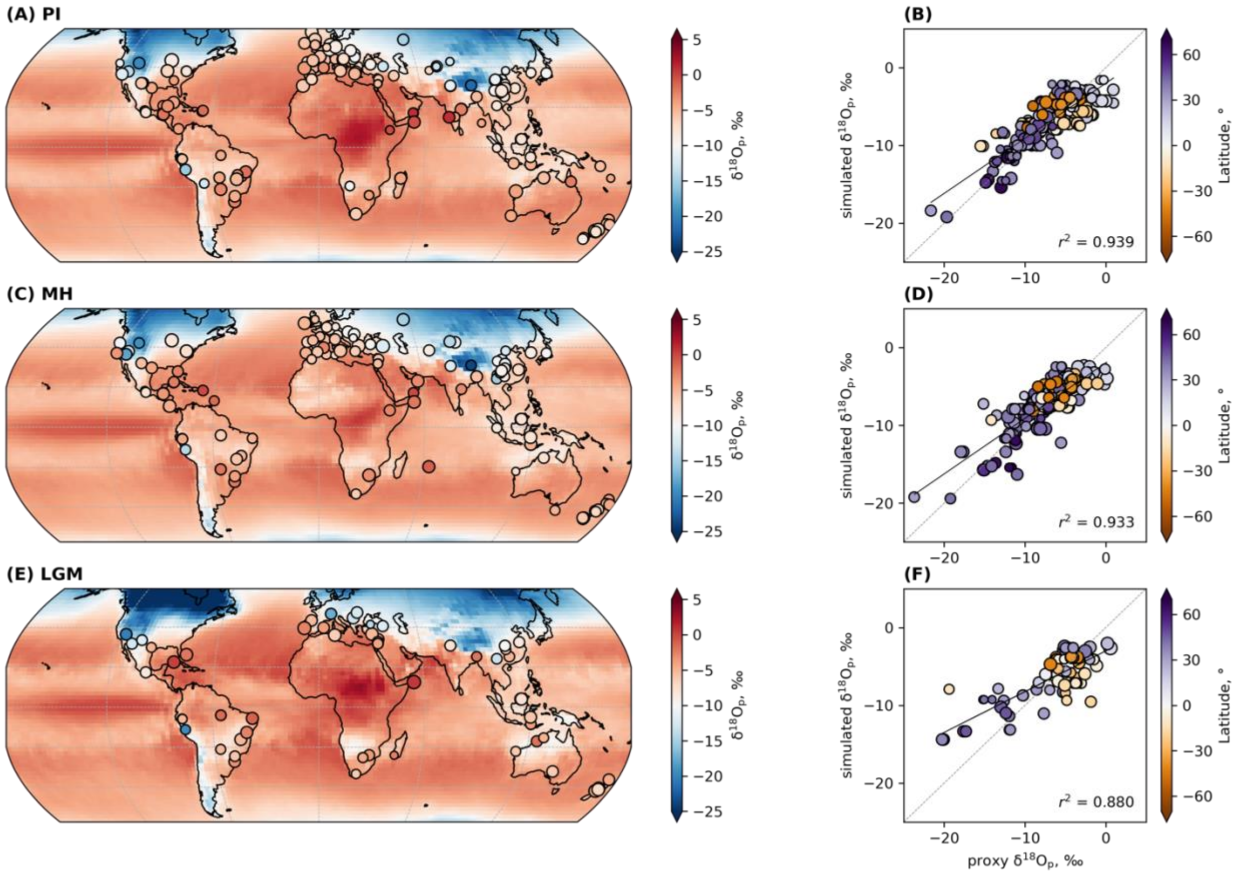

1043

1044 **Fig. S6-i. Same as Fig. S6-a but for the *convective trigger (trigger0.99)* parameterization.**

1045

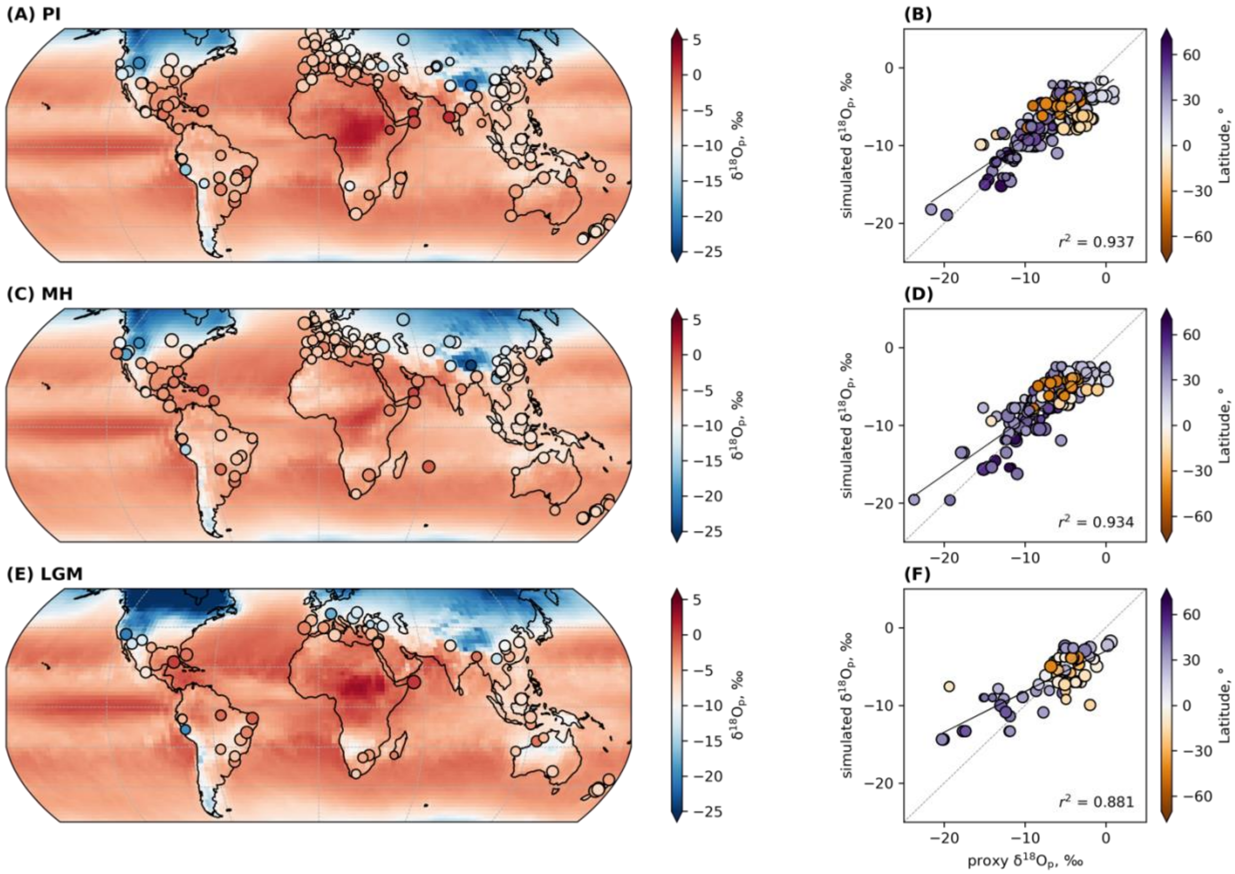

1046
1047 **Fig. S6-j. Same as Fig. S6-a but for the *convective trigger (trigger1.3)* parameterization.**

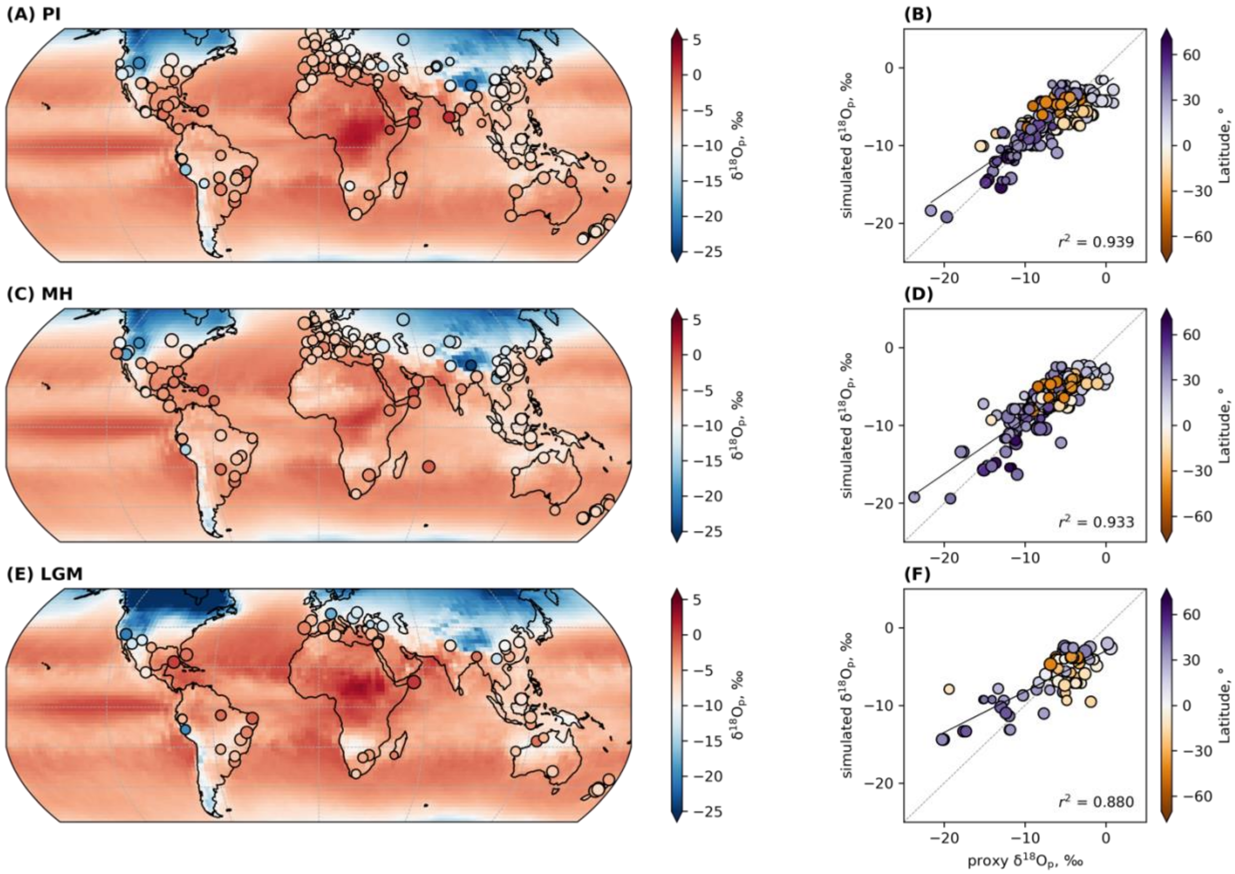

Fig. S6-k. Same as Fig. S6-a but for the *convective trigger (trigger1.0)* parameterization.

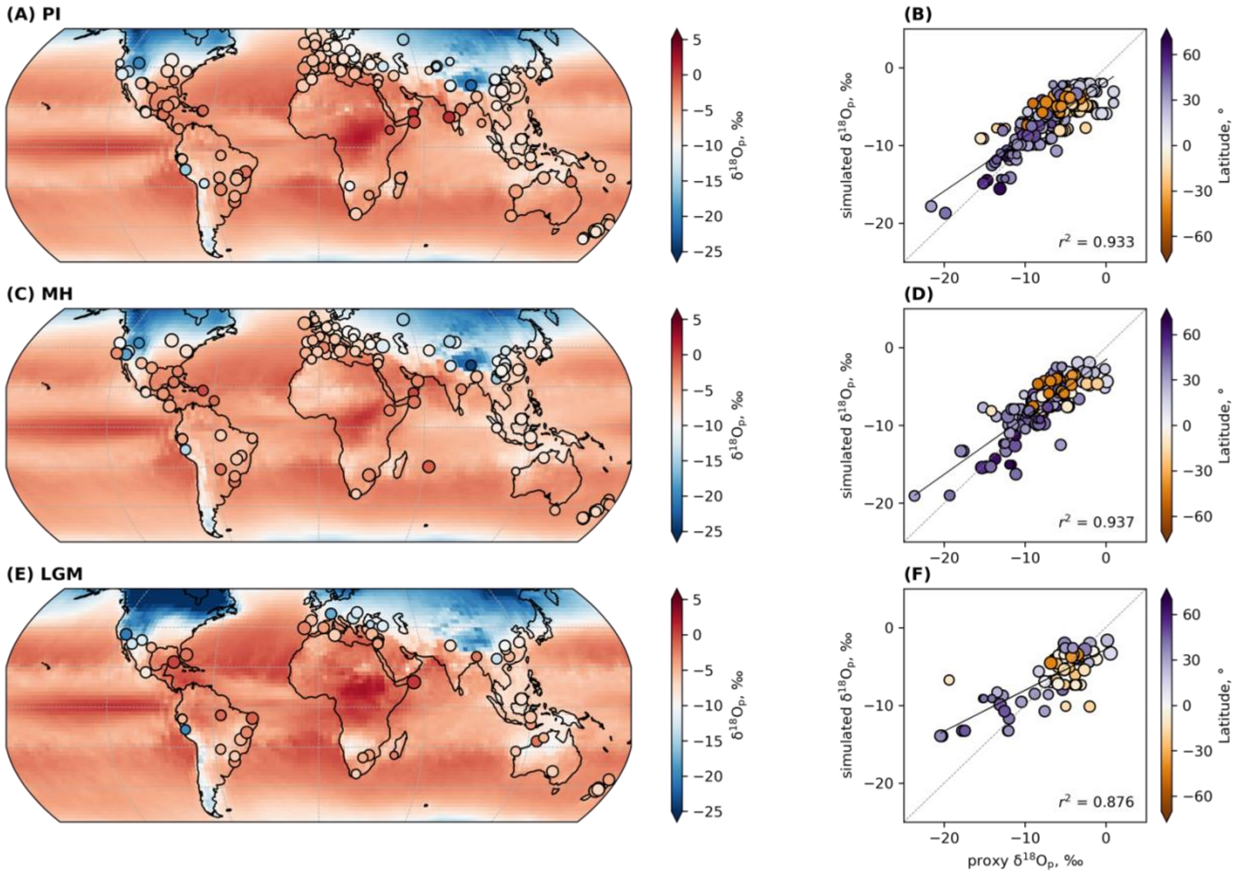

1051

1052 **Fig. S6-l. Same as Fig. S6-a but for the *cloud droplet radius (droprad50-50)* parameterization.**

1053

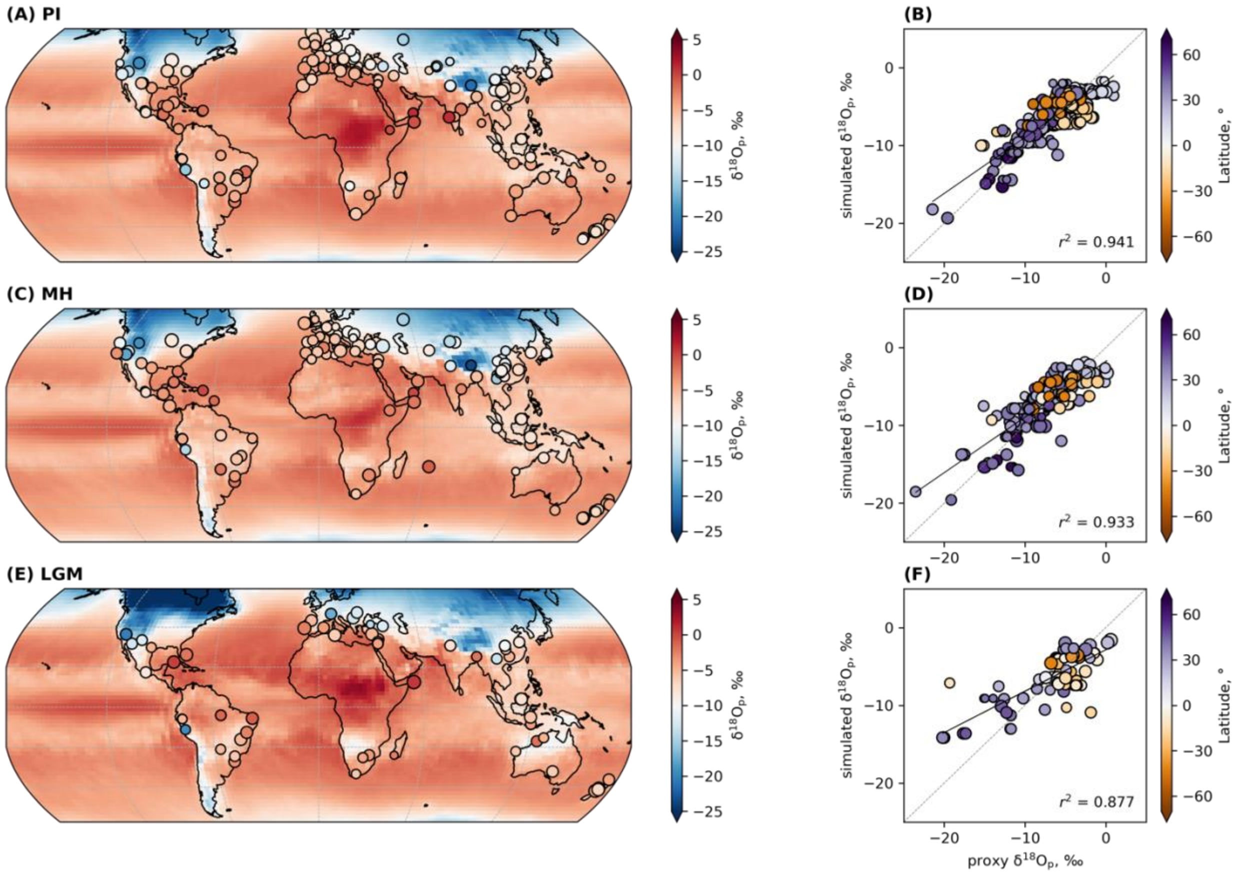

Fig. S6-m. Same as Fig. S6-a but for the *cloud droplet radius (droprad50-130)* parameterization.

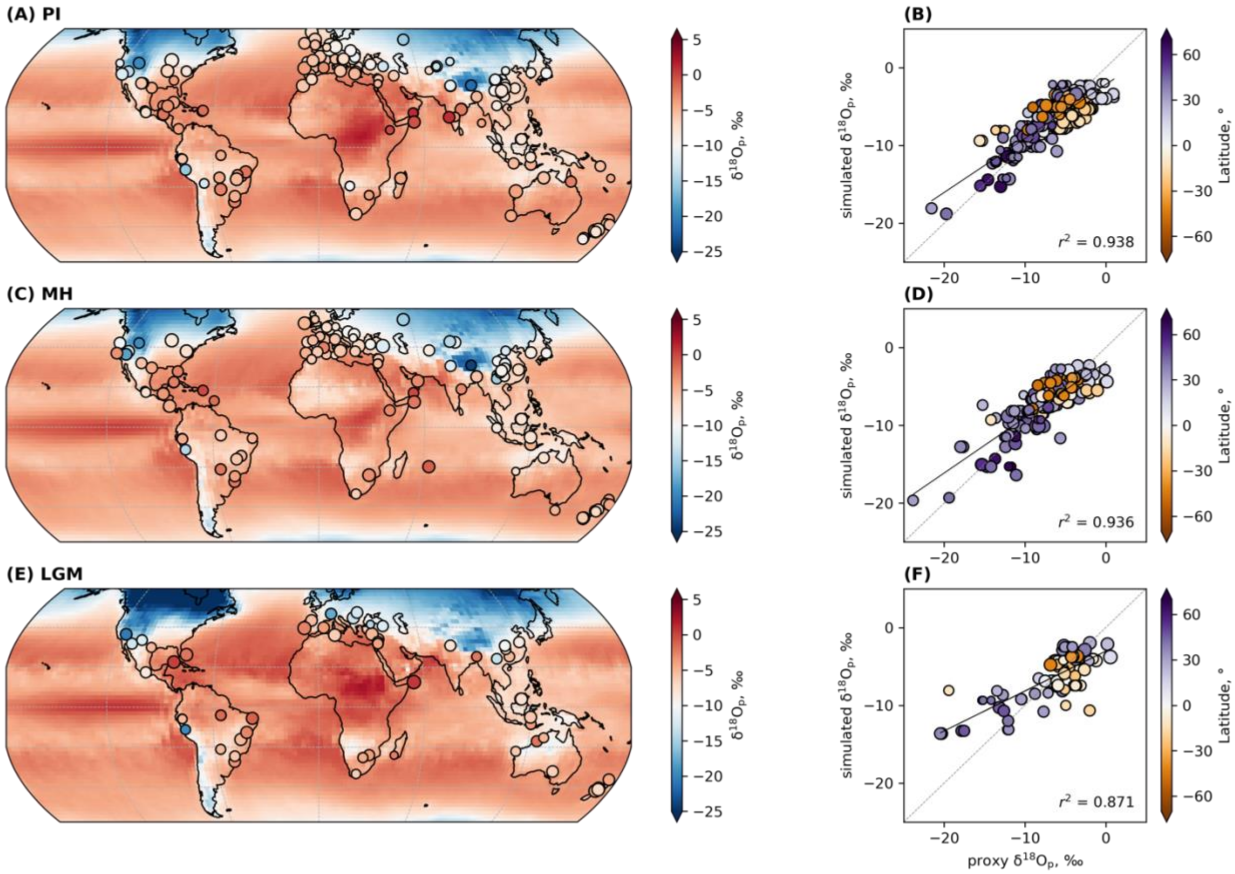

Fig. S6-n. Same as Fig. S6-a but for the *cloud droplet radius (droprad130-50)* parameterization.

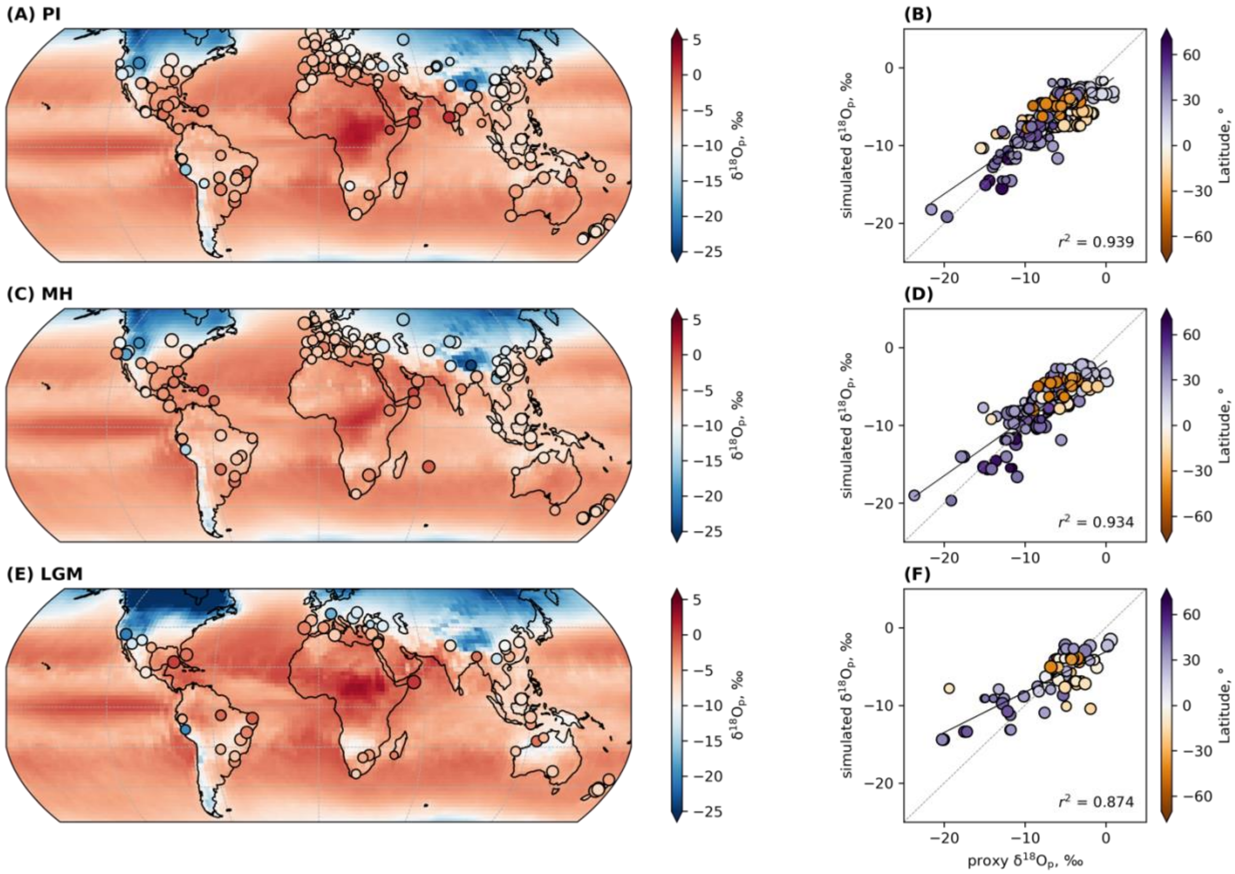

Fig. S6-o. Same as Fig. S6-a but for the *cloud droplet radius (droprad30-130)* parameterization.

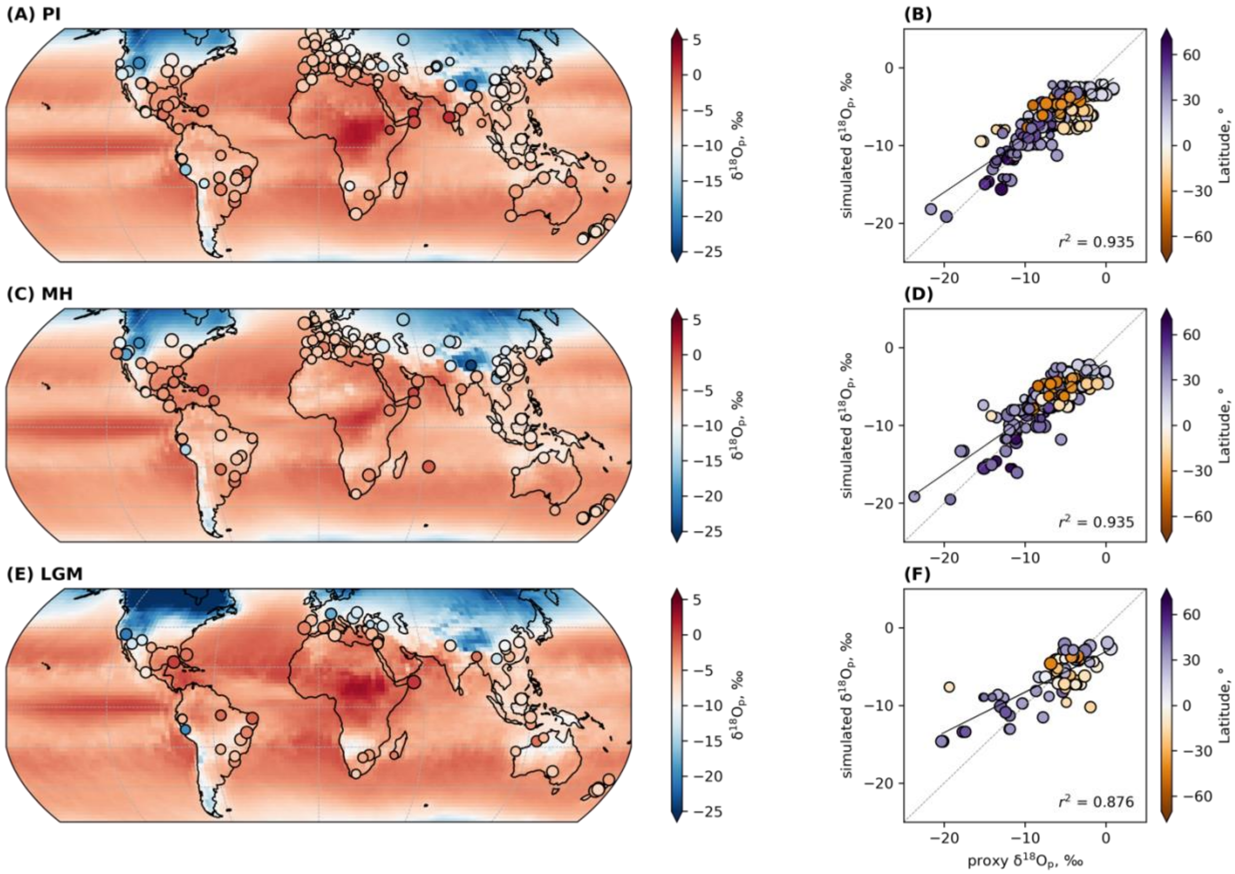

Fig. S6-p. Same as Fig. S6-a but for the *critical cloud water content (critQ2-2)* parameterization.

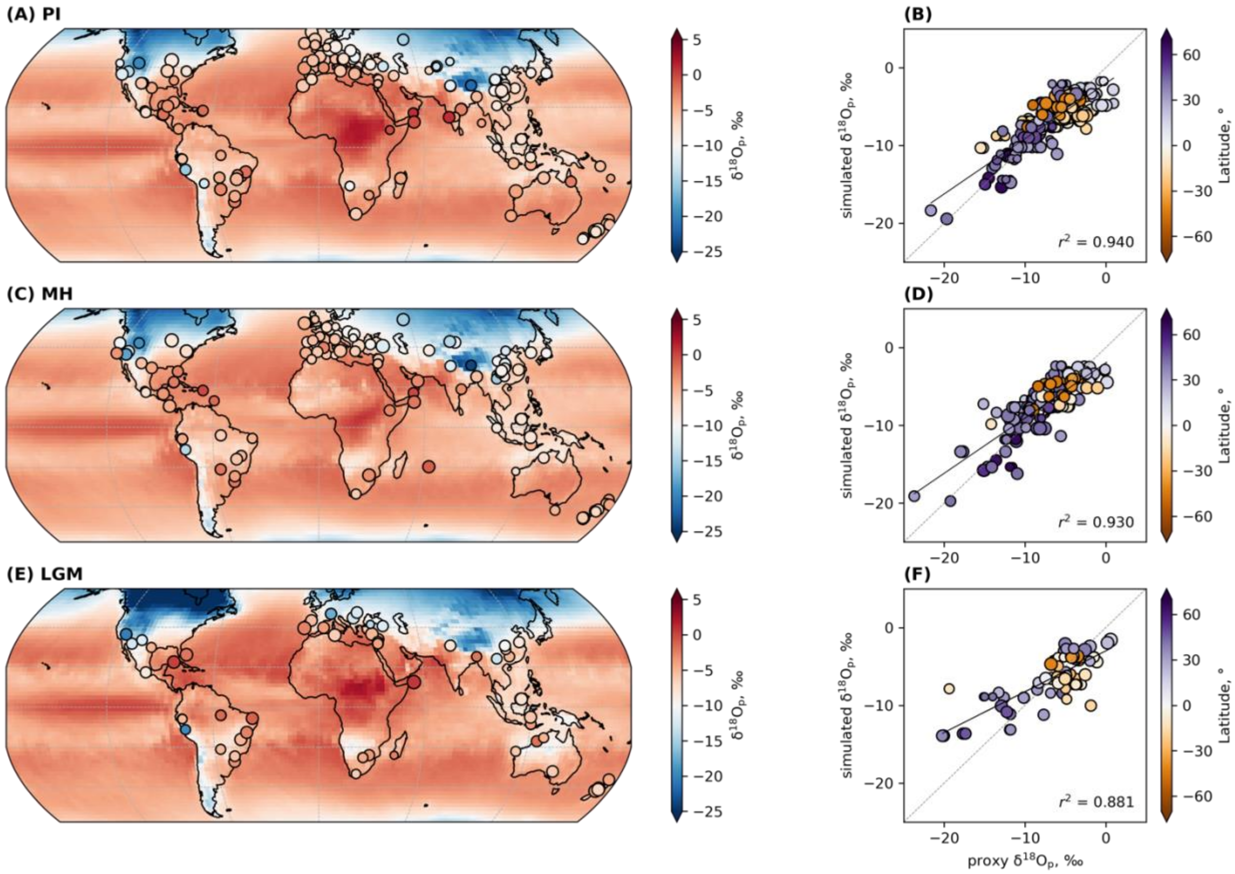

Fig. S6-q. Same as Fig. S6-a but for the *critical cloud water content (critQ1-0.5)* parameterization.

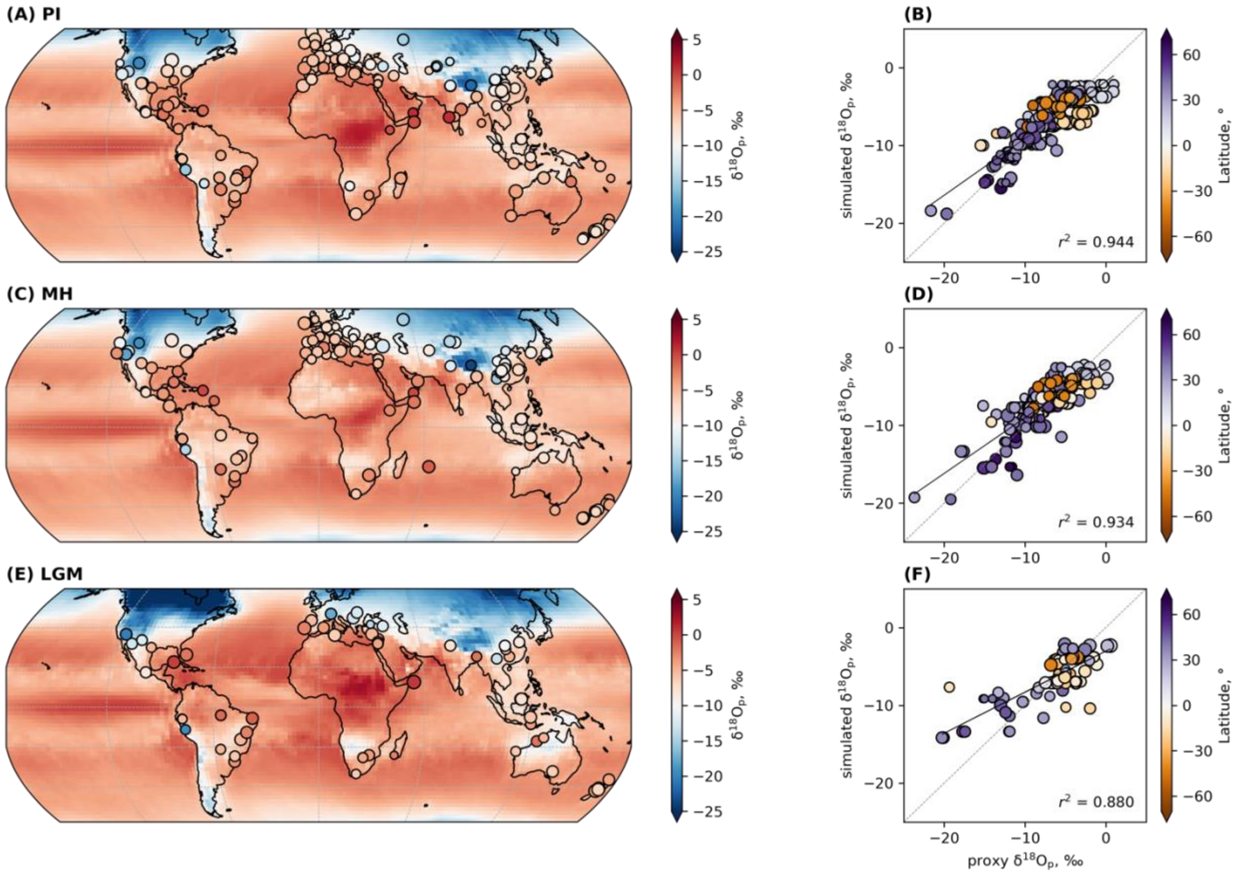

1074

1075 **Fig. S6-r. Same as Fig. S6-a but for the *critical cloud water content (critQ1-4)***
1076 **parameterization.**

1077

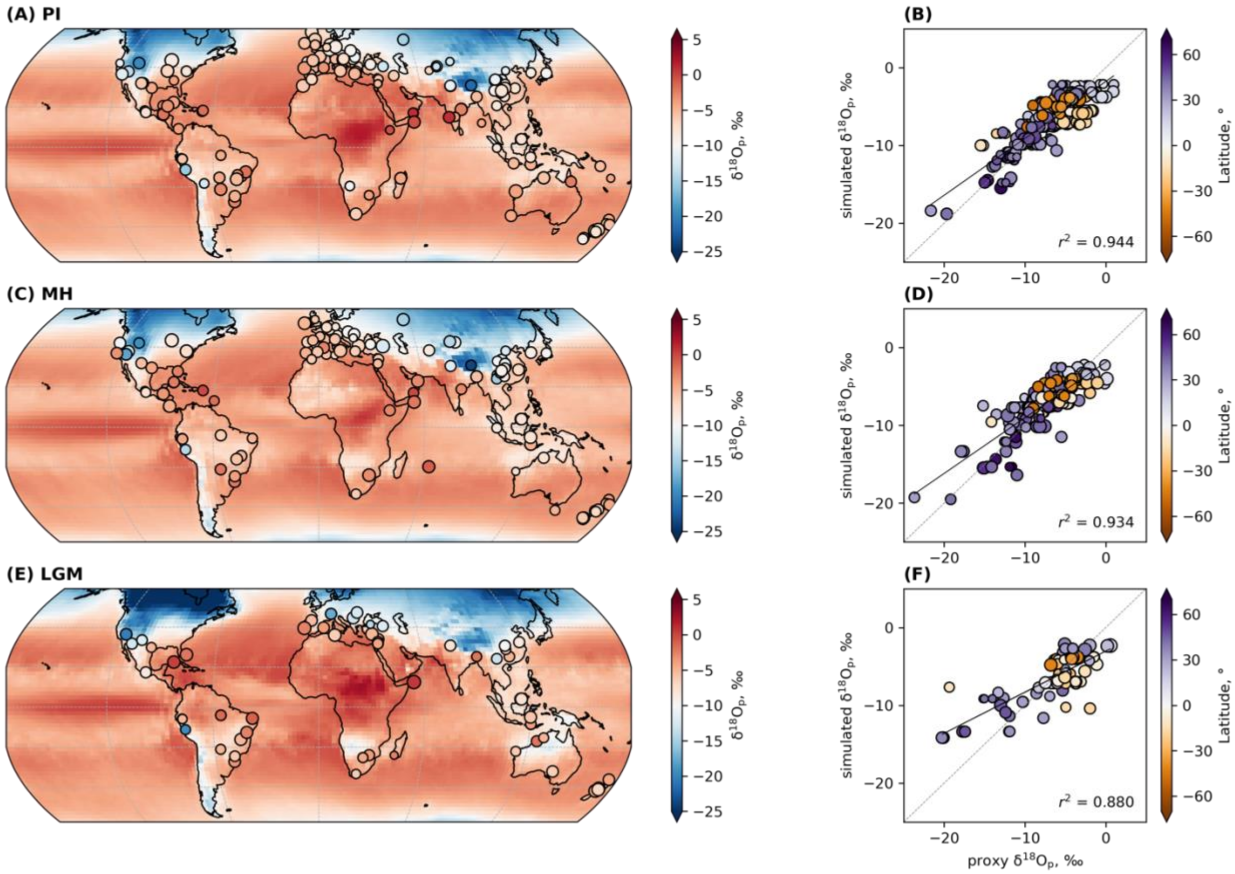

1078

1079 **Fig. S6-s. Same as Fig. S6-a but for the *critical cloud water content (critQ2-4)***
1080 **parameterization.**

1081

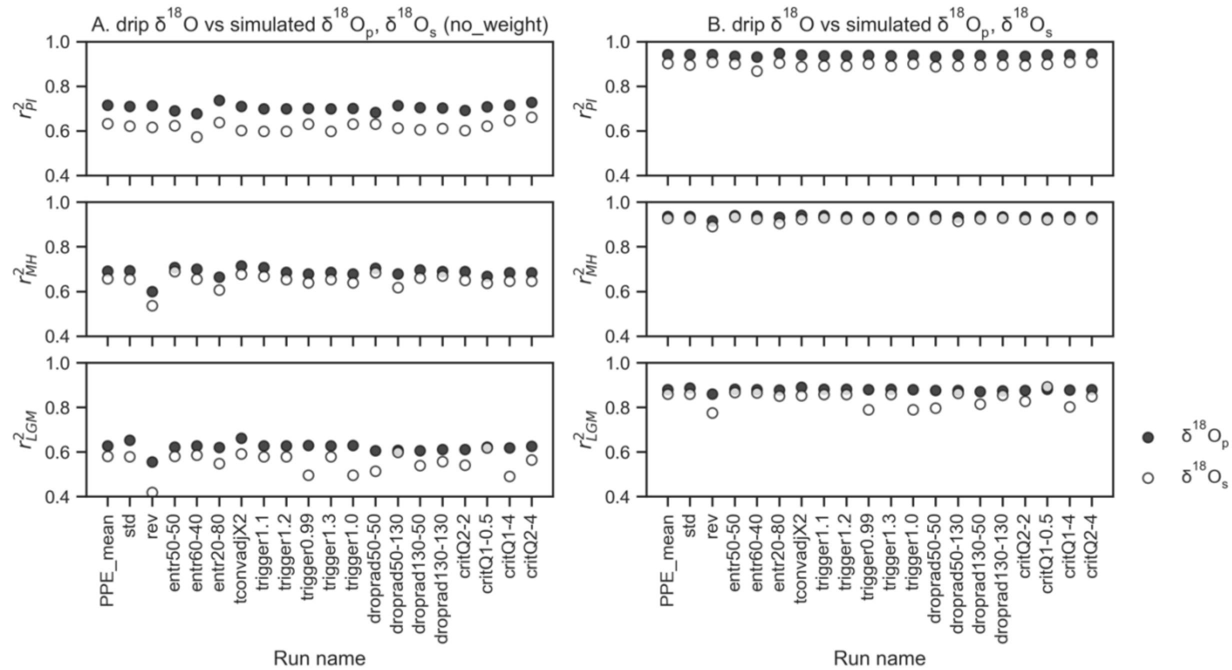

Fig. S7. (A) Non-weighted vs (B) weighted r^2 values between simulated $\delta^{18}O_p$ and SISAL $\delta^{18}O$ for each time period. All speleothem $\delta^{18}O$ were converted to their drip water equivalent.

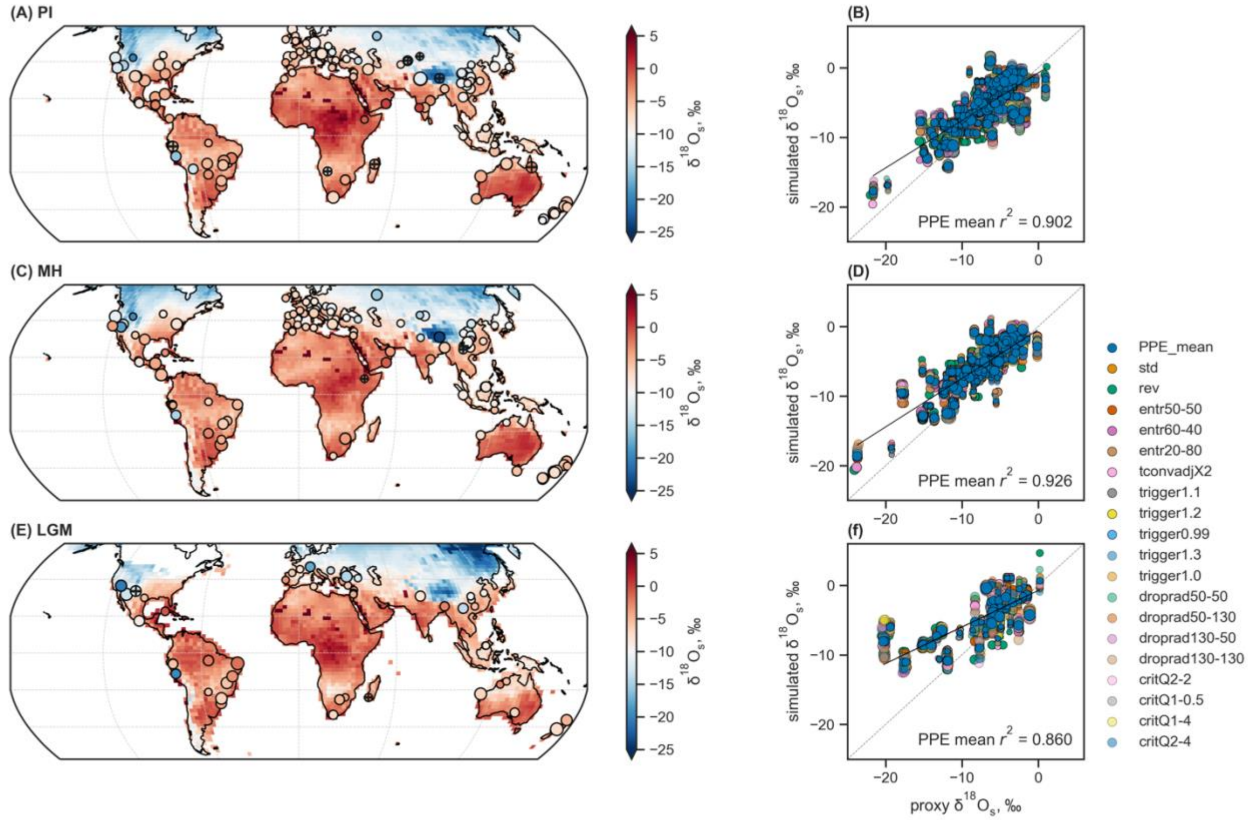

Fig. S8. Comparison of simulated $\delta^{18}O_s$ with speleothem $\delta^{18}O$. Global distribution of simulated $\delta^{18}O_s$ (background) and speleothem $\delta^{18}O$, converted to their drip water equivalents (See Materials and Methods) under (A) PI, (C) MH and (E) LGM conditions. Background and extracted data points are from the PPE mean. SISAL $\delta^{18}O$ points with standard deviation greater than 1 are marked with '+'. Scatterplots between simulated and proxy $\delta^{18}O_s$ for the respective time periods (B, D, F). PPE members are differentiated by color. Black lines represent the weighted least squares regression fits to data points while the gray dashed lines represent the 1:1 line. Weighted r^2 for the PPE mean is reported in the lower right corner of each scatterplot. The size of the circles in all plots are scaled to the sensitivity scores derived for each $\delta^{18}O_s$ simulation.

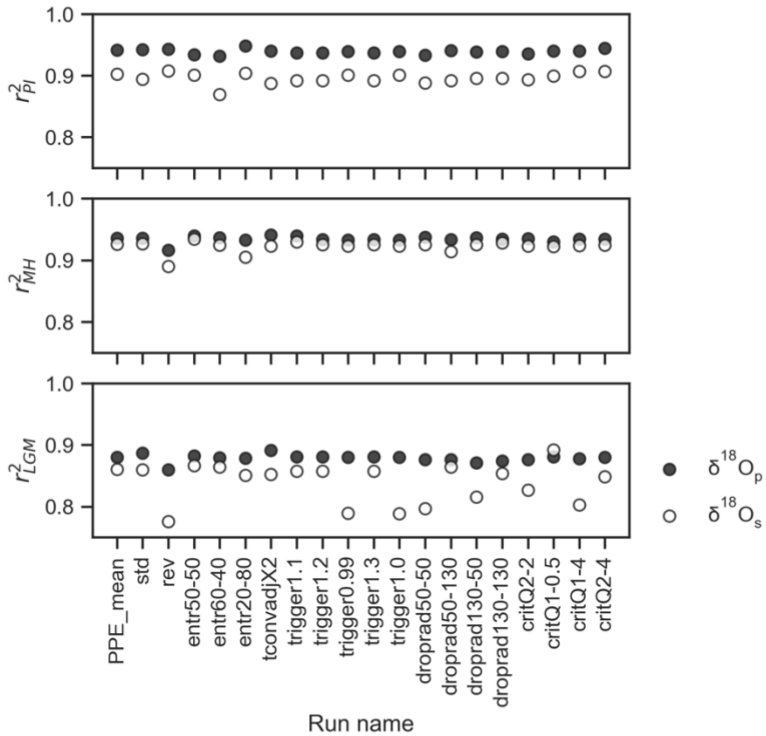

Fig. S9. Weighted r^2 values between simulated $\delta^{18}O_p$ (filled circles; n_{PI} = 257, n_{MH} = 195, n_{LGM} = 81) and $\delta^{18}O_s$ (hollow circles: n_{PI} = 248, n_{MH} = 186, n_{LGM} = 77) and SISAL $\delta^{18}O$ for each time period. All speleothem $\delta^{18}O$ were converted to their drip water equivalent.

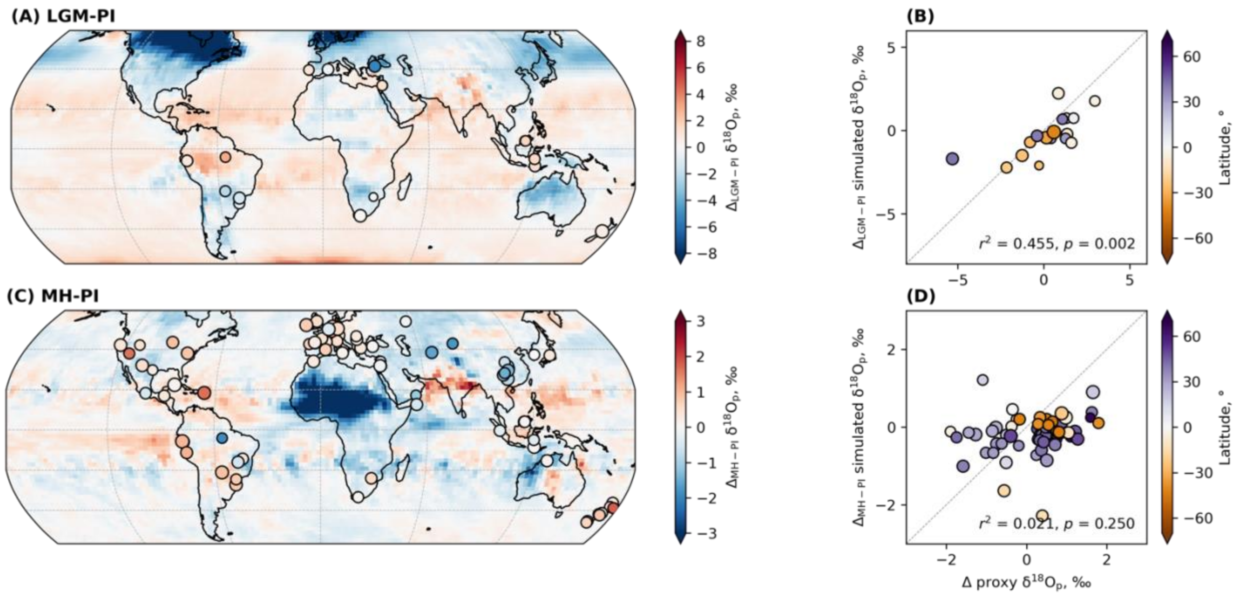

Fig. S10-a. Comparison of simulated $\delta^{18}O_p$ anomalies (background) with speleothem $\delta^{18}O$ (filled circles) for each time slices: (A) LGM-PI (*n* = 17), (C) MH-PI (*n* = 79) for the *standard (std)* parameterization. Background and extracted data points are from the PPE mean. Scatterplots between simulated and proxy $\delta^{18}O_p$ for the respective time periods (B, D). PPE members are differentiated by color. Gray dashed lines represent the 1:1 line. Weighted r^2 for the PPE mean is reported in the lower right corner of each scatterplot. The size of the circles in all plots are scaled to the sensitivity scores derived in Fig. 2.

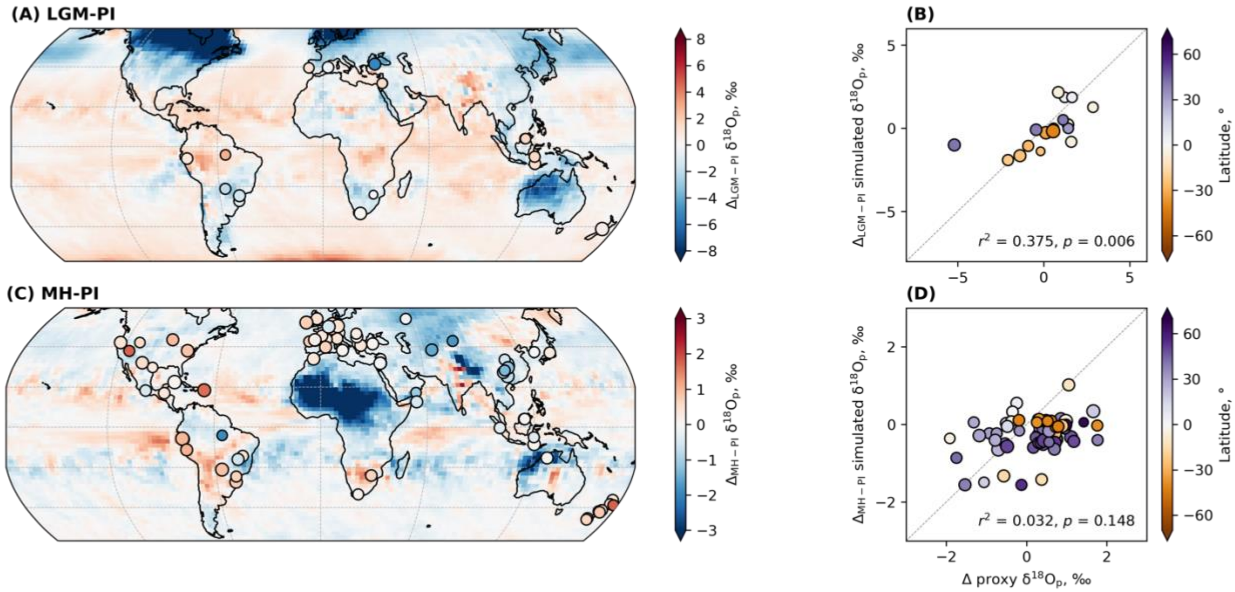

1129
1130 **Fig. S10-b. Same as Fig. S10-a but for the *rain re-evaporation above the cloud base (rev)***
1131 **parameterization.**
1132

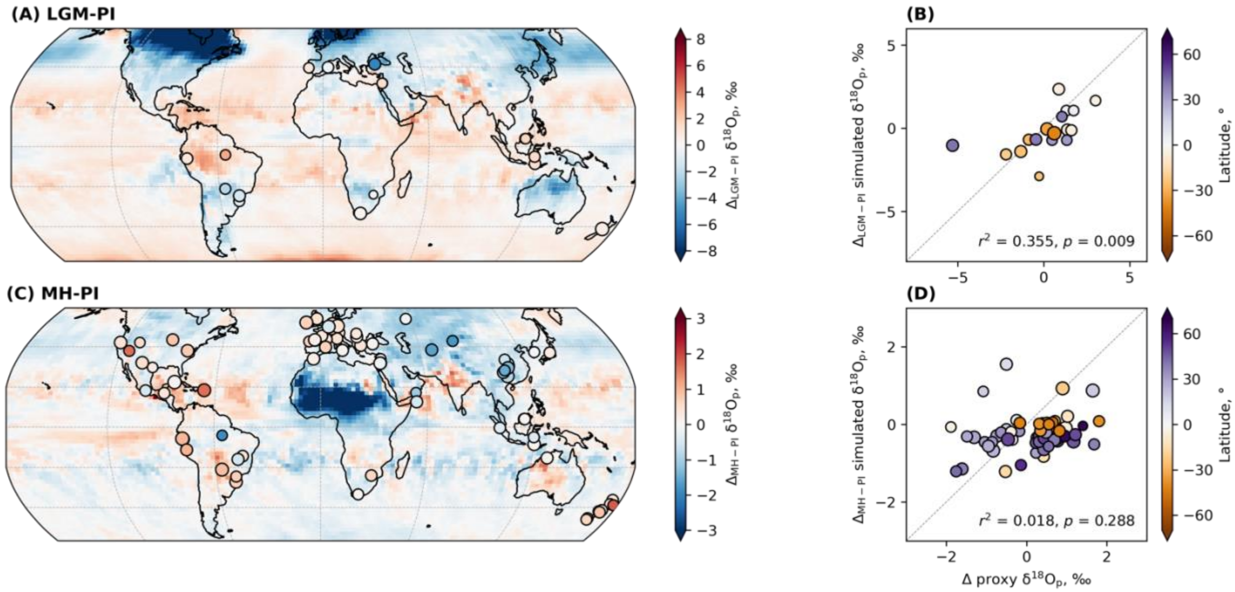

Fig. S10-c. Same as Fig. S10-a but for the *entrainment rate for plume (entr50-50)* parameterization.

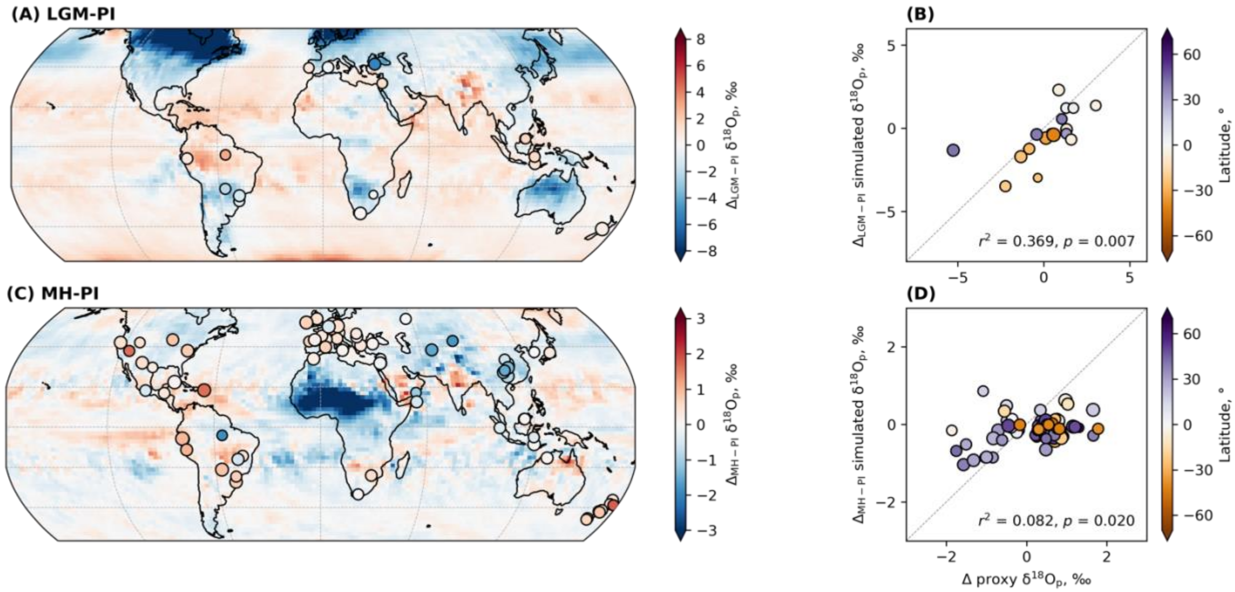

Fig. S10-d. Same as Fig. S10-a but for the *entrainment rate for plume (entr60-40)* parameterization.

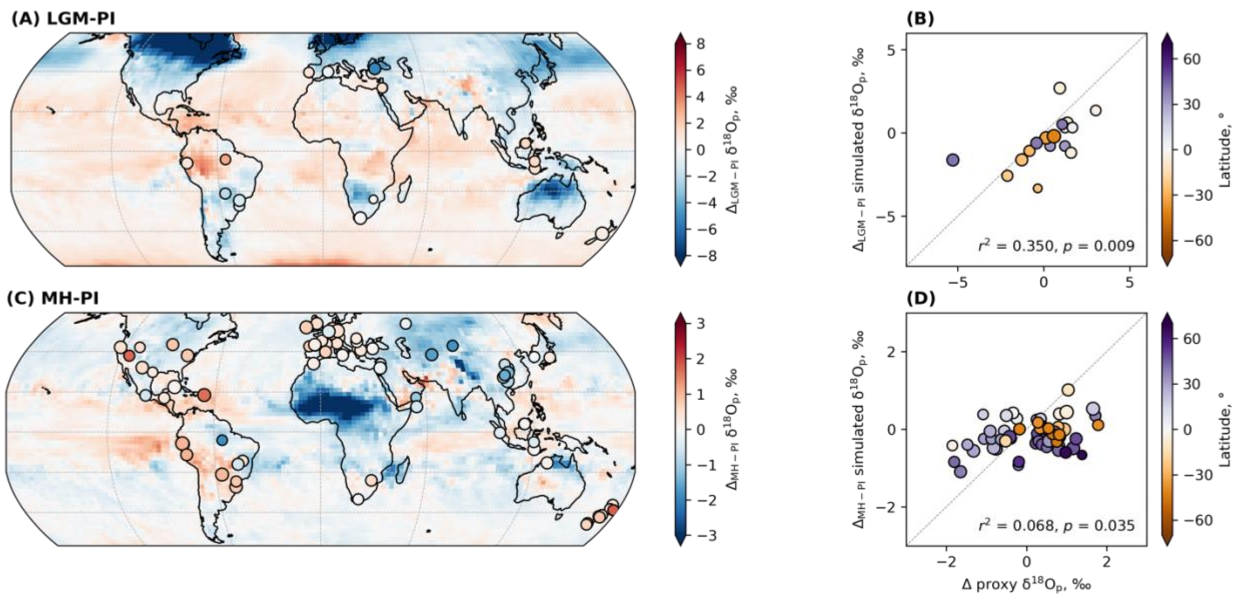

Fig. S10-e. Same as Fig. S10-a but for the *entrainment rate for plume (entr20-80)* parameterization.

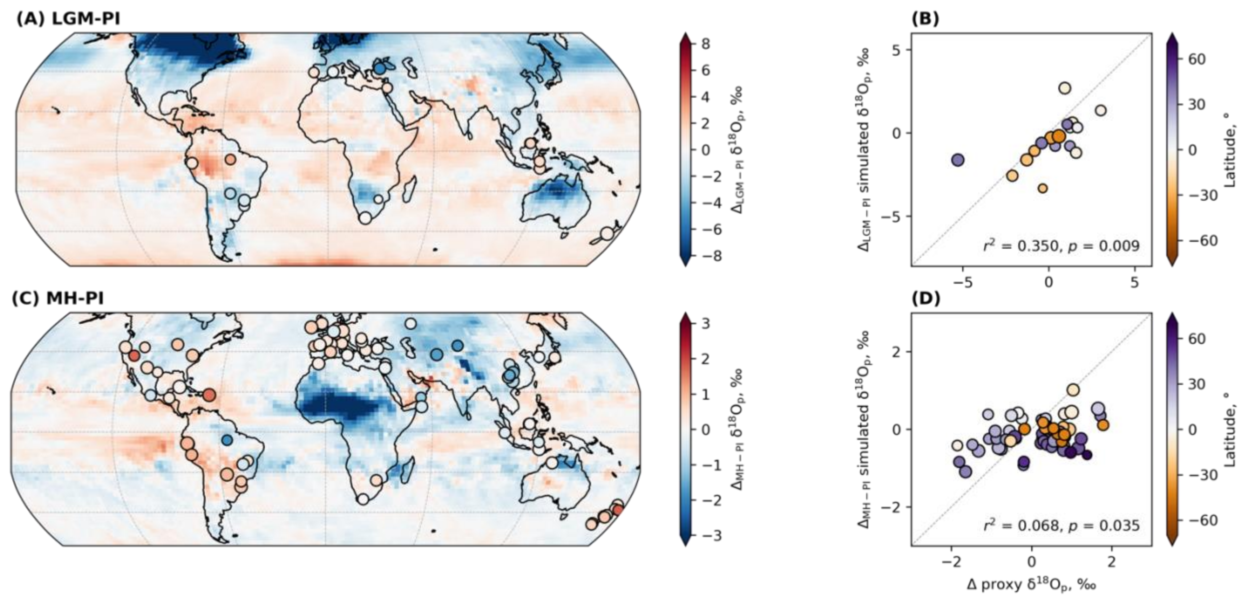

Fig. S10-f. Same as Fig. S10-a but for the *convection adjustment time (tconvadjX2)* parameterization.

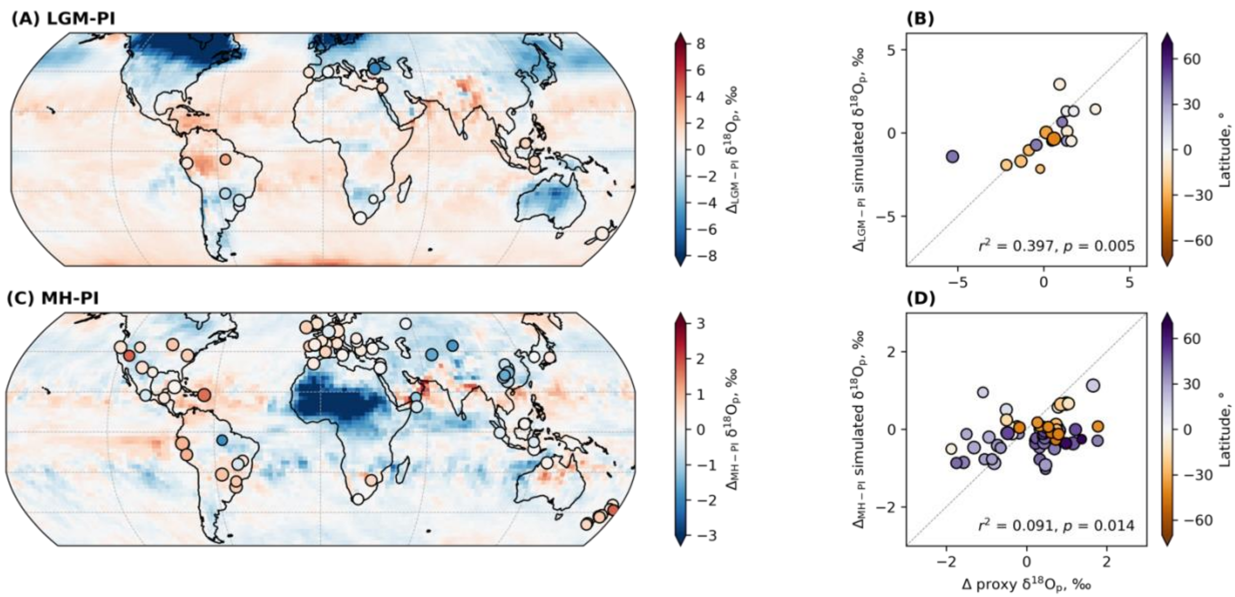

Fig. S10-g. Same as Fig. S10-a but for the *convective trigger (trigger1.1)* parameterization.

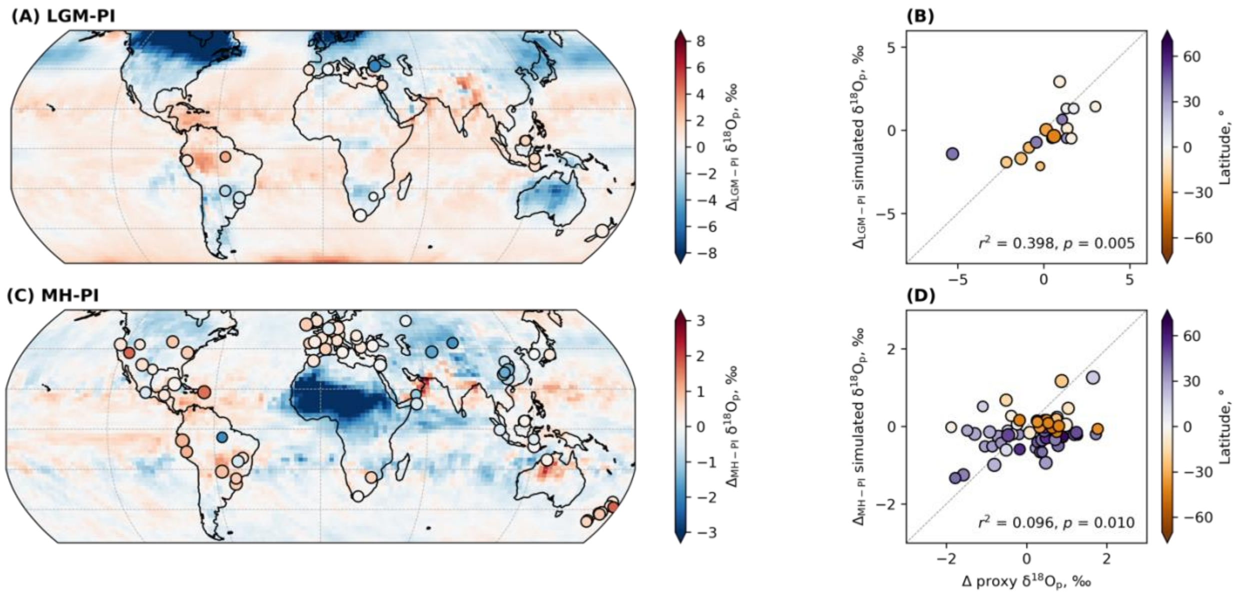

Fig. S10-h. Same as Fig. S10-a but for the *convective trigger (trigger1.2)* parameterization.

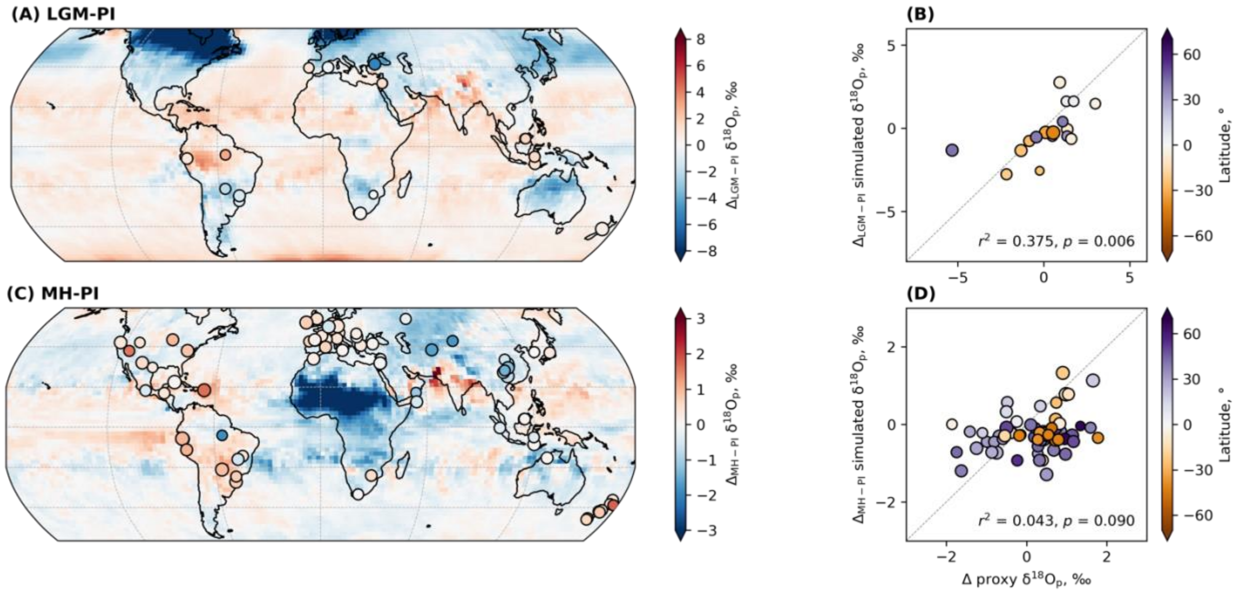

1155
1156 **Fig. S10-i. Same as Fig. S10-a but for the *convective trigger (trigger0.99)* parameterization.**
1157

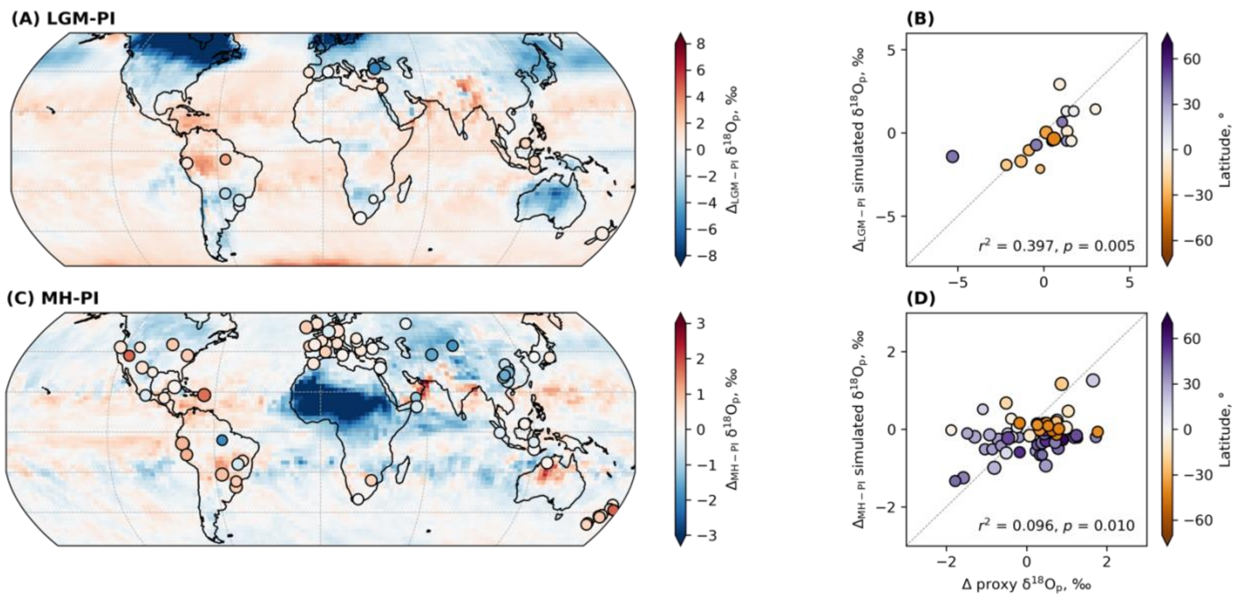

Fig. S10-j. Same as Fig. S10-a but for the *convective trigger (trigger1.3)* parameterization.

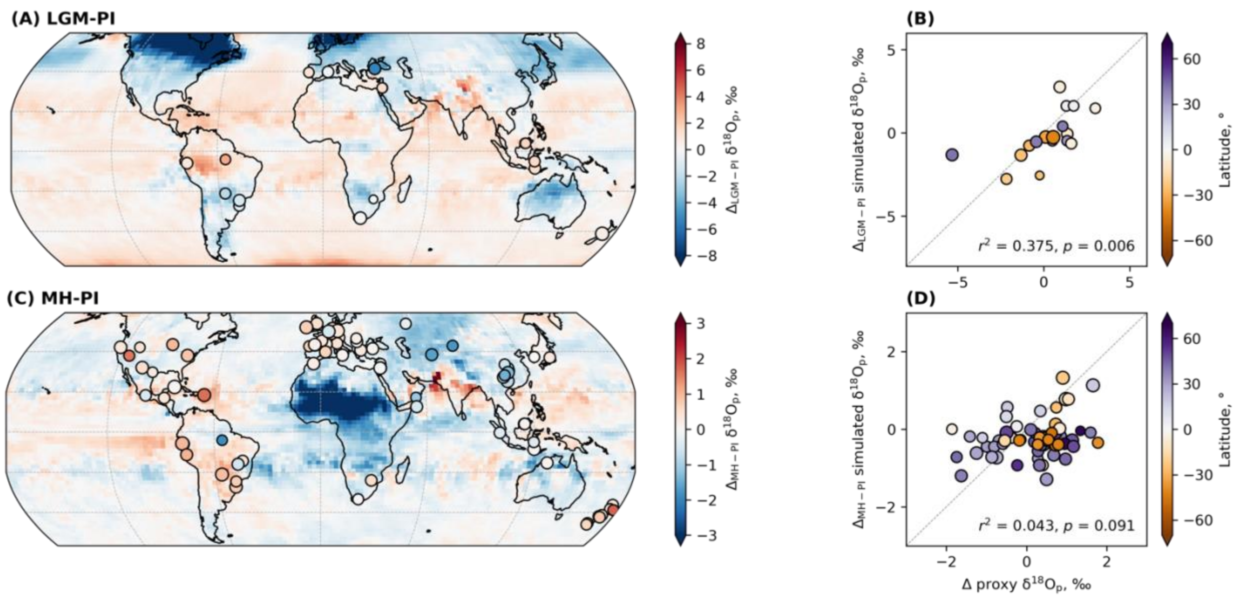

Fig. S10-k. Same as Fig. S10-a but for the *convective trigger (trigger1.0)* parameterization.

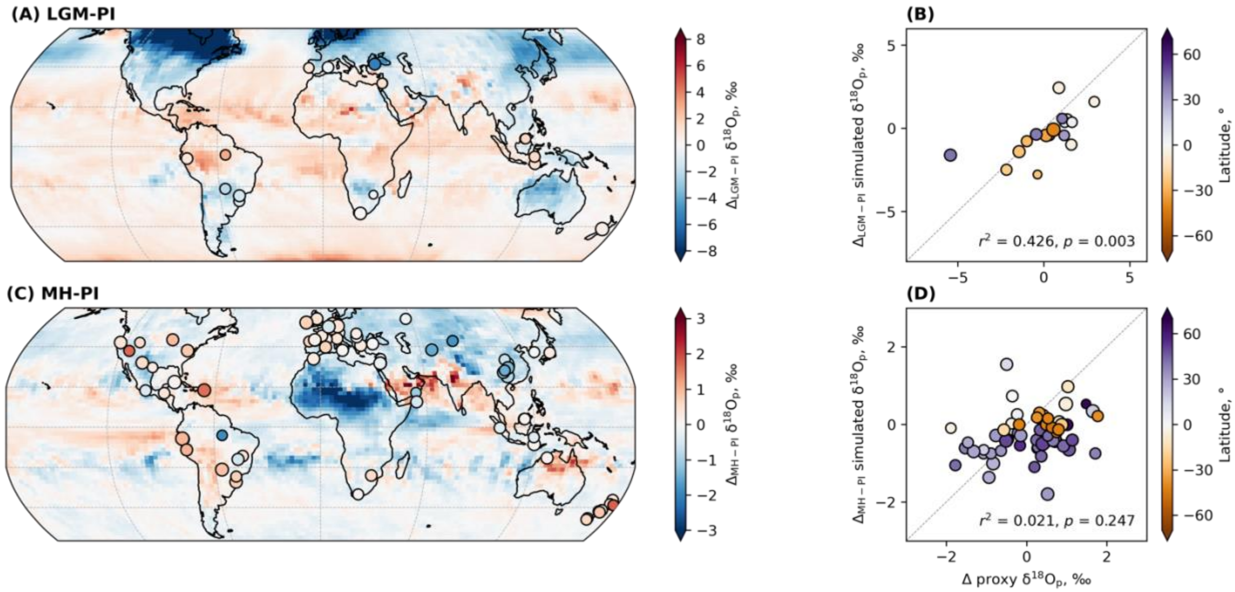

Fig. S10-l. Same as Fig. S10-a but for the *cloud droplet radius (droprad50-50)* parameterization.

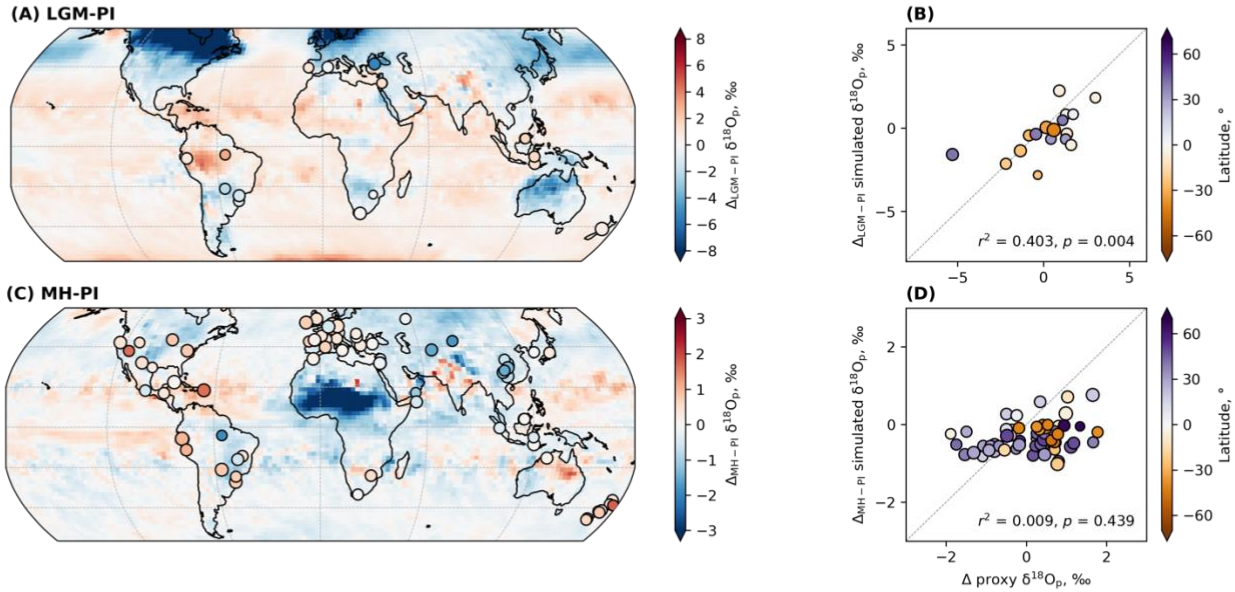

Fig. S10-m. Same as Fig. S10-a but for the *cloud droplet radius (droprad50-130)* parameterization.

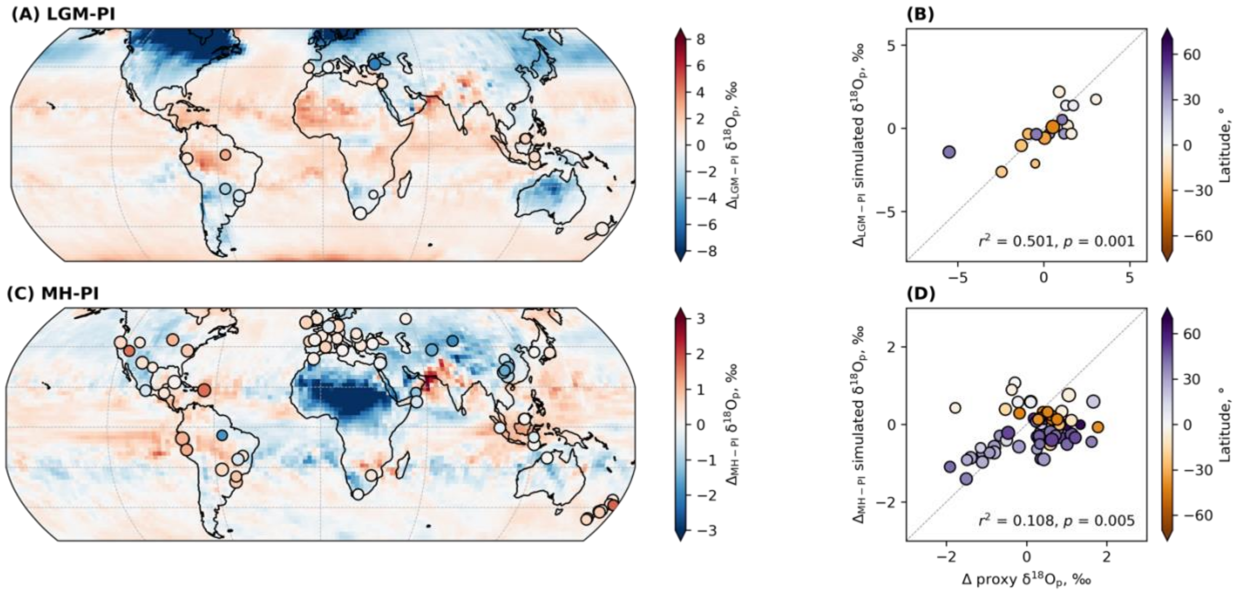

Fig. S10-n. Same as Fig. S10-a but for the *cloud droplet radius (droprad130-50)* parameterization.

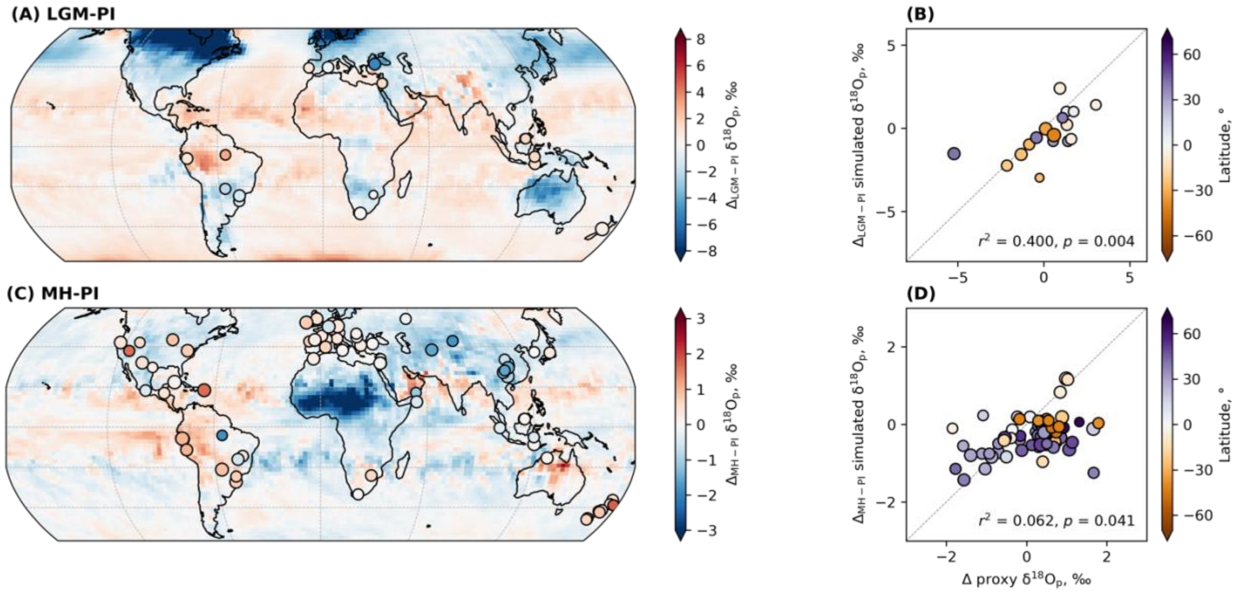

Fig. S10-o. Same as Fig. S10-a but for the *cloud droplet radius (droprad130-130)* parameterization.

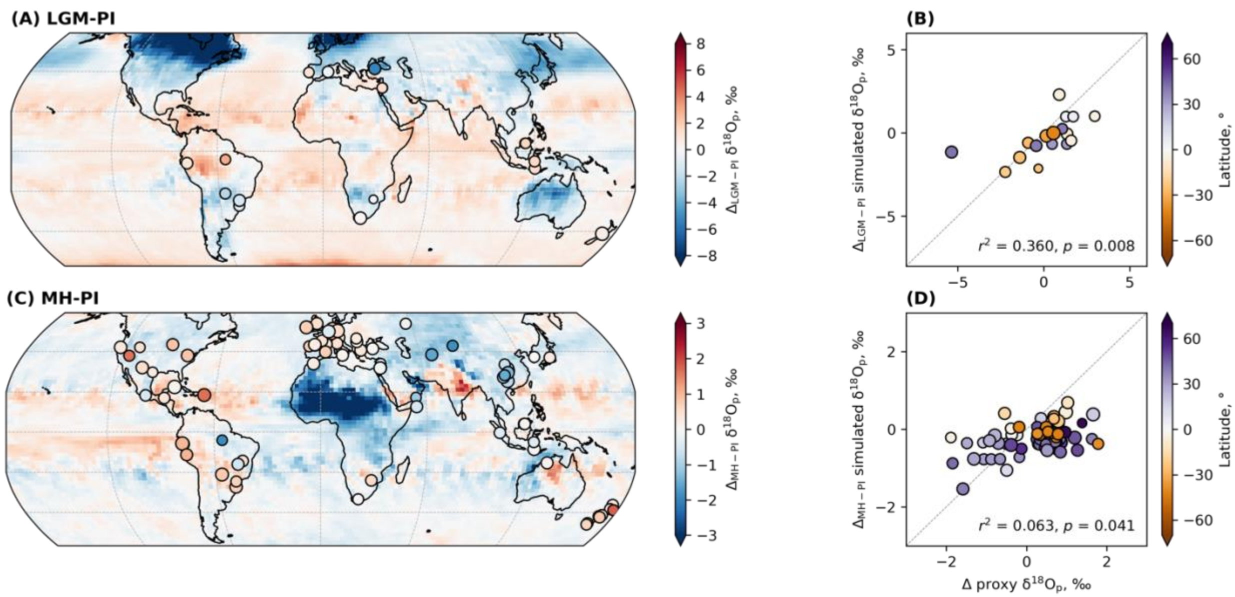

Fig. S10-p. Same as Fig. S10-a but for the *critical cloud water content (critQ2-2)* parameterization.

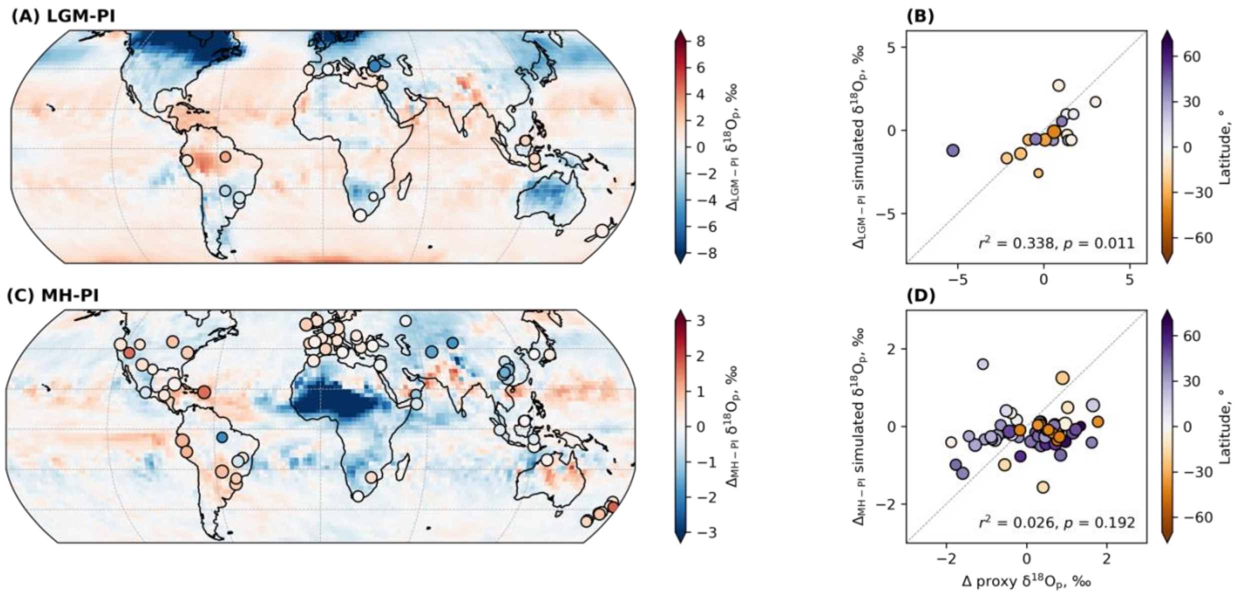

1186
1187 **Fig. S10-q. Same as Fig. S10-a but for the *critical cloud water content (critQ1-0.5)***
1188 **parameterization.**
1189

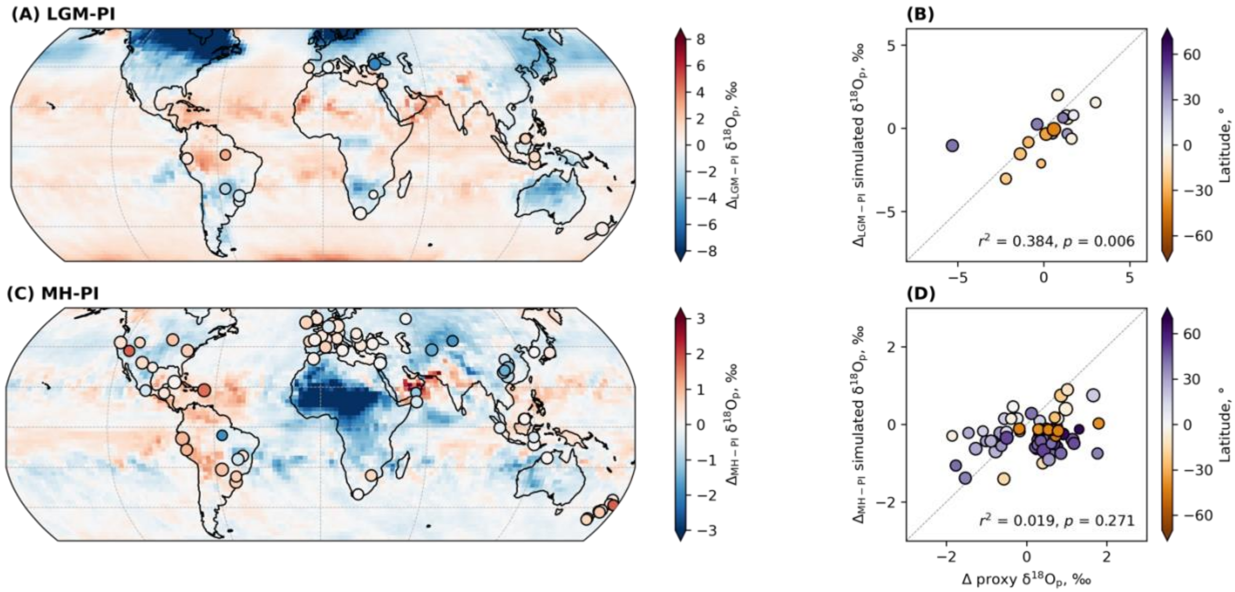

Fig. S10-r. Same as Fig. S10-a but for the *critical cloud water content (critQ1-4)* parameterization.

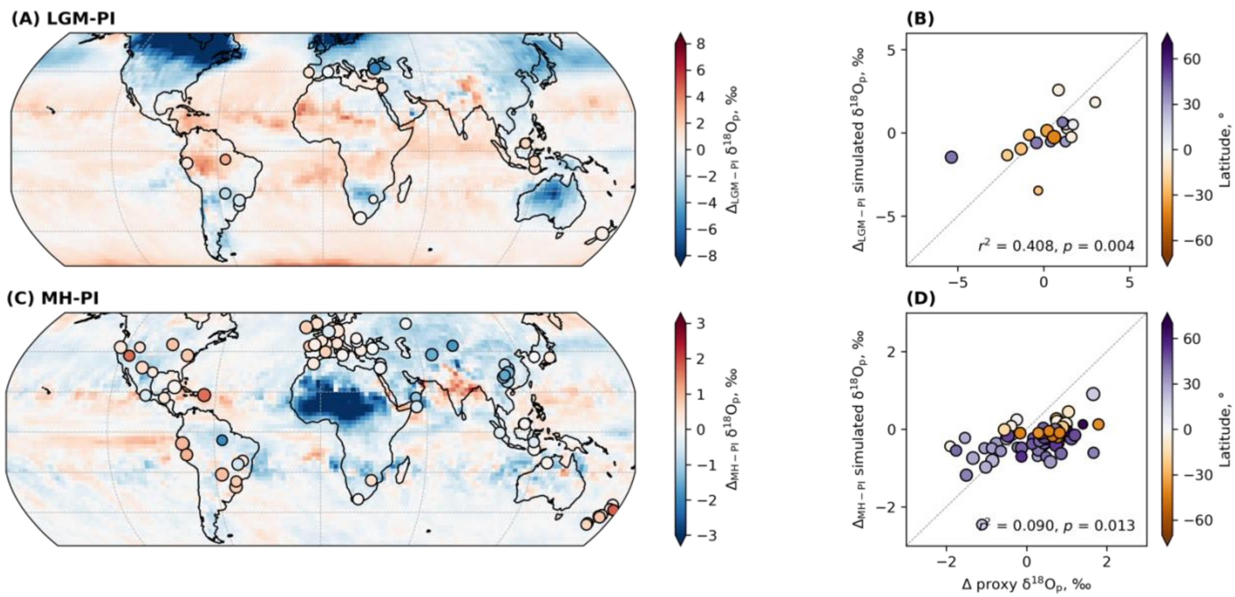

Fig. S10-s. Same as Fig. S10-a but for the *critical cloud water content (critQ2-4)* parameterization.